Author:
Swinscoe, Kirsten

Title:
Smart biological raincoats

directional shedding, regional wettability and impact damage resilience of Attacus moth wing scales.

Smart biological raincoats: directional shedding, regional wettability and impact damage resilience of *Attacus* moth wing scales.

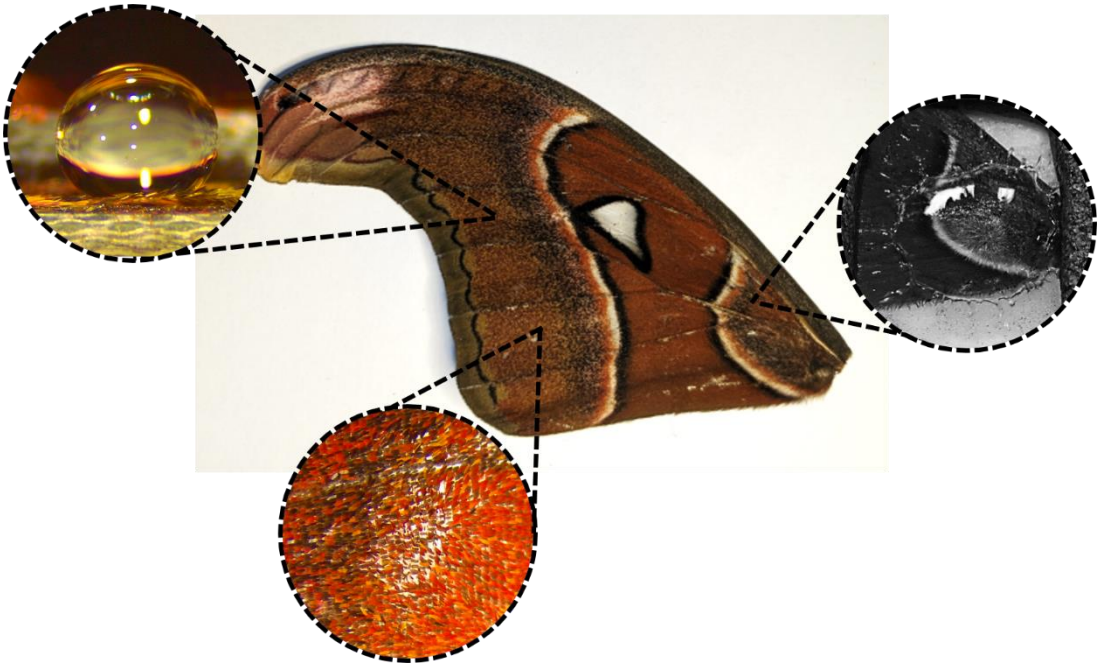

Kirsten Swinscoe

A dissertation submitted to the University of Bristol in accordance with the requirements for award of the degree of Research Masters in the Faculty of Life Sciences

Submitted: 02/07/2024

Word count: 22’974

Abstract

Extremely non-wetting (or superhydrophobic) surfaces have promising industrial applications, many of which have been inspired by phenomena observed in biology. Lepidopteran wings are a prime example of such surfaces due to their multiple functionalities, including acoustic defence, structural colouration and self-cleaning ability. This ability is achieved by the highly structured surfaces, and regular tiling patterns of wing scales. However, the scope of research into lepidopteran wettability is limited due to a lack of focus on moth species, despite moths making up such a large proportion of the taxa. Additionally, the effect of impact damage on the functionality of such surfaces has not yet been quantified in lepidoptera. Quantification of the wettability of *Attacus* moth wings demonstrated strong hydrophobic properties with directional drop shedding capabilities, surpassing the performance of current commercial hydrophobic polymers. *Attacus* scales also constituted a 'shatter-coating' which effectively induced drop shatter, making drop impacts less damaging. However, drop retention and impact resilience demonstrated regional variability. The results of this study reveal *Attacus* wings as a promising new biomimetic model which could be utilised in studies for the development of effective multifunctional superhydrophobic surfaces.

Author’s declaration

I declare that the work in this dissertation was carried out in accordance with the requirements of the University's Regulations and Code of Practice for Research Degree Programmes and that it has not been submitted for any other academic award. Except where indicated by specific reference in the text, the work is my own work. Work done in collaboration with, or with the assistance of, others, is indicated as such. Any views expressed in the dissertation are those of the author.

SIGNED: KIRSTEN SWINSCOE DATE: 2/07/24

Table of contents

Tables and Figures

List of tables:

List of figures:

Abbreviations:

Θ_A – Advancing contact angle

CA – Contact angle

CR – Horizontal crossribs

Θ_H – Contact angle hysteresis

HR – Hierarchical roughness

γ_{LG} – Liquid vapour interfacial energy

LR – Longitudinal ridges

NR – Nanoscale ridges

Θ_R – Receding contact angle

RA – Retention angle

γ_{SL} – Solid-liquid interfacial energy

γ_{SG} – Solid vapour interfacial energy

T_c – Contact time

TW – Transparent window

***We* –** Weber number

We_c – Critical weber number

Chapter 1. Introduction

Interest in extremely non-wetting (or superhydrophobic) surfaces has increased in recent years, driven by promising biomimetic applications, including self-cleaning, anti-biofouling and anti-icing coatings, which facilitate more sustainable human activity (1–3). Sustainability is a key concern regarding accelerating global climate change. ln 2023, the highest atmospheric concentrations of 'greenhouse gases' (CO_2, CH_4 and NO_2) for two million years were recorded, in addition to a 1.1° increase in global surface temperature since 1970 (4).

1.1 Self-cleaning

Self-cleaning of superhydrophobic surfaces is an extremely well-documented phenomenon, first observed on the leaves of the sacred lotus (*Nelumbo nucifera*) (5). Consequently, self-cleaning is commonly described as 'the lotus effect'. Upon contact with superhydrophobic surfaces, drops assume an almost spherical shape, and are readily shed at extremely small elevations (3,5,6). During shedding, contaminating particulates become 'captured' by drops and are passively removed from surfaces (3,5). Overtime, all surfaces become contaminated by biological and anthropogenic particulates, and thus self-cleaning has high applicability regarding renewable energy sources, specifically solar power. Particulate contamination degrades the efficiency of solar panels by blocking light transmission into solar cells, thereby reducing net energy output (7,8). Therefore, the implementation of self-cleaning solar panels promises enhanced efficacy via maximised energy yields and reduced maintenance costs.

1.2 Anti-fouling

Biofouling describes the colonisation of submerged surfaces by aquatic organisms, including barnacles and algae (9). Biofouling of ship hulls is of particular concern due to potential adverse effects on hydrodynamic performance (10,11), resulting in greater fuel consumption. Reduced fuel efficiency has a significant environmental impact, given that shipping accounts for ~80% of global trade (12). Current biofouling mitigation involves the application of biocidal paints (13). However, untargeted leaching of toxins poses a long-term risk to aquatic biodiversity (14). Superhydrophobic surfaces have an unfavourable surface energy for the development of strong adhesive bonds by fouling species, facilitating easy removal via water flow (2,15). Consequently, utilisation of superhydrophobic coatings on ship hulls, offers significant environmental and financial benefits through improved hydrodynamic performance, and reduced necessity for extended dry-docking (2,10,11).

1.3 Anti-icing

Amplified air-resistance caused by ice accretion significantly contributes to the deterioration of the mechanical performance of outdoor machinery, including aircrafts and turbines (16). Additionally, ice accretion increases load, accelerating structural fatigue and damage (17,18), and thus maintenance costs. Present methods of de-icing, including electrothermal and mechanical techniques, are expensive, time-consuming and inefficient (19). At present, the potential anti-icing properties of superhydrophobic surfaces are focused on three key attributes. Firstly, self-cleaning of superhydrophobic surfaces may prevent ice accretion via the removal of water before the onset of freezing (20). Second, superhydrophobic surfaces exhibit a high time and/or temperature threshold for freezing, resulting from a low rate of heat transfer caused by minimal contact of spherical drops (21,22). Finally, the low surface energy of superhydrophobic surfaces causes poor adhesion of formed ice, which is easily removed by external forces, such as wind or rotational force (23). However, anti-icing properties deteriorate overtime in response to damage of surface features resulting from repeated cycles of ice formation (24). Consequently, further investigation to identify robust superhydrophobic surfaces, with high resilience to prolonged periods of ice formation, is necessary to ascertain the viability of biomimetic anti-icing coatings as viable alternatives to current de-icing methods.

1.4 Defining superhydrophobic surfaces

1.4.1 Wettability: Contact angles

Wettability describes the intermolecular interactions between a liquid and a solid surface. On ideal smooth surfaces wettability is defined by Young's equation (25):

$$\gamma_{SG} - \gamma_{SL} - \gamma_{LG}\, cos\theta_c = 0$$

Young's equation describes the relationship between the interfacial energies of the solid-vapour (γ_{SG}); solid-liquid (γ_{SL}) and liquid-vapour (γ_{LG}) interface, known as the 'three-phase contact line'. This produces a contact angle (θ_c), henceforth referred to as CA, which is measured from the intersection of tangents drawn across the γ_{SL} and γ_{LG} interfaces (**Error! Reference source not found.**a) (26).

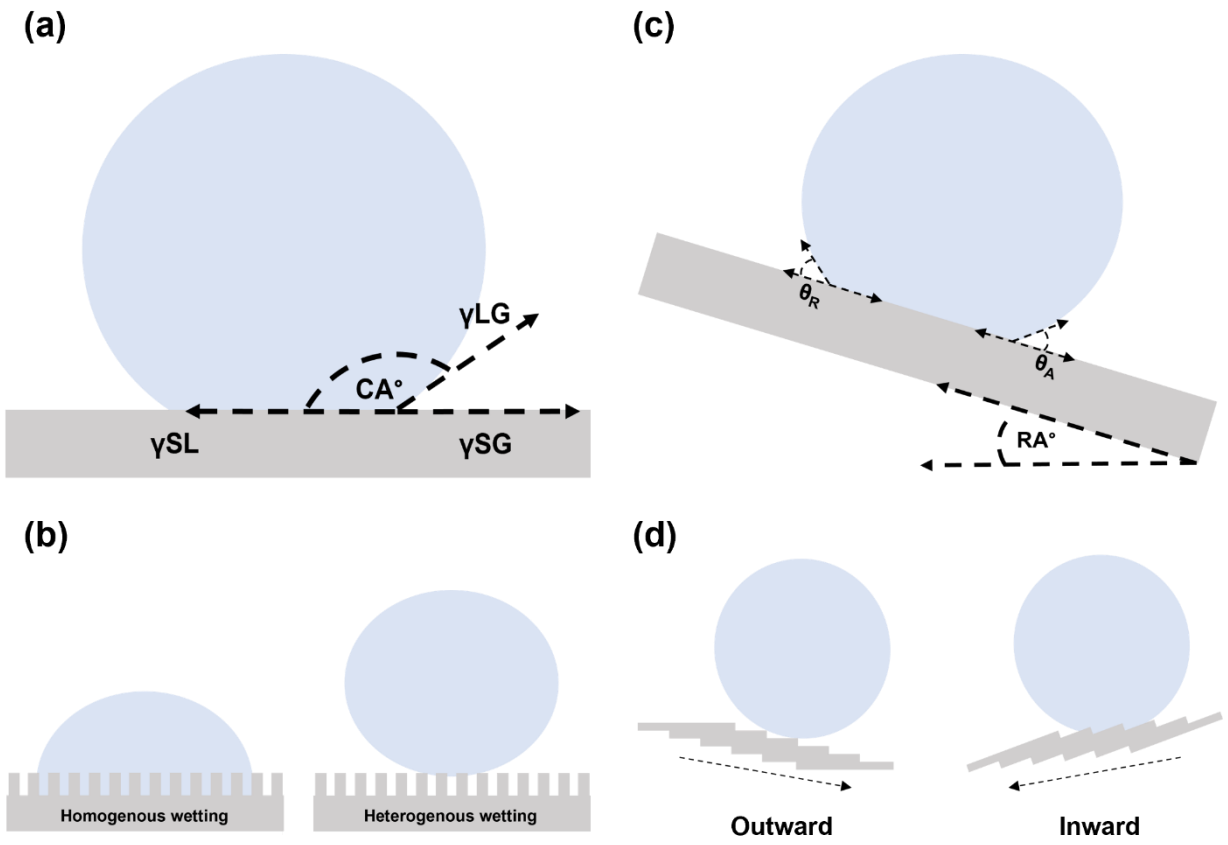

Figure 1. A schematic of common drop metrics used for classifying surface wettability. (a) The contact angle (CA) of a sessile drop, formed by the relationship between three interfacial energies: solid-vapour (γ_{SG}), solid-liquid (γ_{SL}) and liquid-vapour (γ_{LG}). CAs are measured from tangents drawn between the γ_{SL} and γ_{SG} interfaces; and between the γ_{SL} and γ_{LG} interfaces (represented by dashed arrows) (25). (b) A visual representation of homogenous (34); and heterogeneous (35) wetting regimes exhibited by drops on rough surfaces.(c) The shedding of drops from tilted surfaces can be measured using either contact angle hysteresis (θ_H) or retention angle (RA). θ_H represents the difference between advancing (θ_A) and receding (θ_R) CAs during drop movement. RA represents the surface elevation angle at which drop movement is initiated. (d) A visual representation of direction-dependant energy barriers formed by asymmetric surface roughness, which facilitate directional drop shedding.

CAs are a well-established metric for classifying surface wettability, using the following categories: CA = 0° (superhydrophilic), 0° < CA < 90° (hydrophilic), 90° < CA < 150° (hydrophobic) and CA > 150° (superhydrophobic).

1.4.2 Wettability: Surface structure

Surface wettability is determined by chemical composition and physical topography (or roughness (5,27,28). Biological superhydrophobic surfaces are chemically comprised of inherently hydrophobic materials, including chitin (28) and epicuticular waxes (5,6). All biological surfaces exhibit roughness, which significantly enhances their inherent chemical

wettability. The degree of enhancement is dependent on the density and aspect ratio of roughness features (29–33).

Surface wetting is classified under two regimes: (i) homogeneous wetting (or Wenzel wetting) (34); (ii) heterogenous wetting (or Cassie-Baxter wetting) (35) (Figure *1*b). Wenzel wetting describes the complete penetration of surface features by drops (34,36), which results in a large contact area, thereby increasing solid-liquid interfacial adhesion (henceforth referred to as adhesion). Wenzel drops assume a 'flattened' shape and remain adhered to tilted surfaces (33), and thus are often associated with hydrophilic surfaces (CA <90º). Conversely, Cassie-Baxter wetting describes the suspension of drops on entrapped air-pockets within roughness features (35,36), resulting in a small contact area, thereby reducing adhesion. Consequently, Cassie-Baxter drops assume a near spherical shape and are readily shed from tilted surfaces (5,33). Wenzel and Cassie-Baxter wetting regimes are not discrete, and penetration of suspended drops into roughness features is possible by external force, including vibration, impact and pressure changes (37), commonly known as a Cassie-to-Wenzel transition.

Superhydrophobic surfaces exhibit hierarchical roughness (henceforth referred to as HR), comprised of microscale (≥ 1µm) and nanoscale (≤ 2000 nm) surface features (5,29,38,39). Generally, HR promotes the entrapment of air pockets, and thus superhydrophobic surfaces often, but not always, exhibit Cassie-Baxter wetting (31).

For example, rose petals are classified as a superhydrophobic surface (CA >150°), yet are not self-cleaning. Instead, drops exhibit strong adhesion even when tilted 180° (27), in a phenomenon termed 'the petal effect'. The petal effect is attributed to HR comprised of high aspect ratio surface features, which allow partial drop penetration into microscale, but not nanoscale, features (27,31,32), known as the Cassie-impregnating state (31).

Superhydrophobic surfaces are classified as either 'slippery' (the lotus effect) or 'sticky' (the petal effect). Therefore, the use of CAs alone for classifying wettability is arbitrary, due to a failure to acknowledge dynamic drop-surface interactions, including drop retention (40–42).

1.4.3 Drop retention

Drop retention is defined by contact angle hysteresis (θ_H):

$$\theta_H = \theta_A - \theta_R$$

θ_H represents asymmetry between the advancing CA (θ_A) and receding CA (θ_R) of mobile drops (Figure *1*c), arising from obstruction of the advancing contact line by roughness features (43,44). During Cassie-Baxter wetting, suspension of drops upon the tips of roughness features effectively reduces such obstruction, thereby resulting in a low θ_H (36, 44).

θ_H is measured either directly via the manipulation of sessile drops (45) or indirectly using retention angles (RA) as an inferential metric. RA describes the angle of elevation of a tilted surface at which gravity is sufficient to overcome adhesion and initiate drop movement Figure *1*c) (46). Typically, so called 'slippery' superhydrophobic surfaces exhibit θ_H and RA values <5° (40,42). Consequently, this study defines a surface as superhydrophobic when CA is >150º and RA is <5º.

1.5 Impact resilience of biological surfaces

Whilst fabrication of biomimetic superhydrophobic surfaces is well-understood and relatively straightforward (3,8,45,47,48), the long-term durability of such surfaces, regarding repeated mechanical stress, is of major concern (49–51). This is particularly important when developing superhydrophobic coatings intended for external use, including wind turbines and solar panels. For example, raindrops falling at terminal velocity (~10 m/s) have the potential to generate significant impact force (~10 Mpa) (52). Therefore, repeated drop impacts may result in gradual damage of superhydrophobic surfaces, and, consequently, the deterioration of water repellency (49,53).

Dynamic interactions between impacting drops and solid surfaces have an extensive research history, attributable to a widespread scientific interest ranging across many disciplines, including the application of agricultural chemicals onto crops (54,55); the preservation of heritage sites against surface erosion (56); and the forensic analysis of blood spatter patterns (57). The potential damaging effects of repeated drop impact during precipitation on building materials, such as concrete and steel, have garnered particular attention, due to a high demand on global development on robust infrastructure (58–62). Such research has been accelerated in recent decades by refinement of high-speed videography and computational power (63–67). Consequently, present studies may elucidate complex drop impact dynamics for a range of industrial and biological surfaces with extreme detail.

The extent of drop impact damage is governed by two factors: Weber number (*We*) and contact time (T_c) (52,68). *We* is a dimensionless quantity which describes the interrelationship between drop velocity (v^2) and surface tension (σ)during impact, represented by the equation:

$$We = \frac{\rho v^2 \varnothing}{\sigma}$$

where ρ and $\varnothing$ denote the drop density and diameter respectively (69). Typically, raindrops falling at terminal velocity have a *We* of ~$10^2 – 10^3$ (52). Contact time (T_c) measures the duration for which impacting drops remain in direct contact with a surface (67). Generally, high *We* and T_c values indicate significant force transfer into surfaces (70,71), and therefore more damaging impacts During impact, force is transferred into surfaces in two ways: impact stress and shear stress (67,72,73).

1.5.1 Impact stress

Impact stress, such as hydraulic shock, describes force transfer resulting from the sudden deceleration of drops during initial contact with a surface (52,72). The extent of impact stress, and thus damage, is dependent on the velocity at which a drop contacts a surface. Consequently, raindrops falling at terminal velocity generate high impact stress, with a potential to cause irreversible structural damage to surfaces, such as fractures, tears, and holes (52,74). Additionally, impact stress exerted on superhydrophobic surfaces may trigger a Cassie-to-Wenzel transition, temporarily erasing water repellency (37,75).

1.5.2 Shear stress

Shear stress is a consequence of friction between surfaces and radially spreading drops during impact (67,76). Repeated shear stress causes gradual erosion of hierarchical surface features (49) Plant surfaces, including lotus leaves, reduce the effects of shear through the formation of new layers of epicuticular waxes, which regenerate HR (77,78). Despite recent developments (79), the implementation of effective self-healing biomimetic surfaces remains challenging due to technological restrictions (80). Consequently, research into alternative biological adaptations for impact resilience, including elastic responses and drop shatter, is imperative.

1.5.3 Elastic resilience: Leaves

The elastic responses of leaves to drop impact, such as deformation via downward flexion, twisting, and flapping, are well documented (81–85). During leaf deformation, kinetic energy is converted into elastic energy, leading to two possible outcomes. Firstly, leaves may yield, which causes drops to retain a large proportion of their kinetic energy and roll off the deformed surface (82,84). Secondly, at the point of maximum deformation, leaves may spring back into their original position and propel drops upward, known as the 'springboard effect' (83). The magnitude of leaf deformation is governed by surface rigidity, resulting from the biochemical composition of leaf tissues (86,87).

1.5.4 Elastic resilience: Insect wings

Similar elastic responses to impact stress have been documented in Hymenoptera forewings, which contain a flexible resilin joint, known as a costal break (88–90). During collisions with vegetation, the costal break causes wings to deform, which minimises the accumulation of damage (90), thereby maintaining flight efficiency (89). However, the efficacy of the costal break in mitigating against drop impact is yet to be established.

Documentation of elastic responses of insect wings against drop impact is extremely limited (91–93), compared to elastic responses of leaves. This is likely a result of mechanical constraints, whereby insect wings must retain a certain degree of stiffness to enable flight.

1.5.5 Non-elastic resilience: Drop shatter

Regarding biomimetics, elastic responses as a strategy for impact resilience are of limited relevance, given that many applications of superhydrophobic surfaces require high rigidity for optimal efficiency, such as anti-fouling ship hulls. Consequently, surfaces which exhibit passive resilience by modifying the impact dynamics of falling drops are of greater interest.

Generally, when the *We* of an impacting drop exceeds a certain threshold, inertia is greater than surface tension, causing drops to 'shatter' into satellite droplets (69,94,95). This threshold is termed the critical Weber number (We_c). Drop shatter occurs during the radial spread phase of impact, in which drops advance outwardly, creating a thin film (or liquid lamella). During radial spread, the advancing contact line becomes unstable and forms 'finger-like' projections, which detach and are ejected as smaller droplets (63,96). Hydraulic shock causes shock-like waves to propagate across the spreading lamella. When the troughs of these waves encounter roughness features, holes form within the lamella, which subsequently coalesce in a process known as

nucleation (95). Drop shatter reduces the damaging effects of impacts by dissipating impact stress over a larger area (55). Additionally, the ejection of satellite droplets from surfaces significantly reduces T_c, thereby decreasing shear stress (95,97).

When $We < We_c$, surface tension predominates over inertia causing inward retraction of the liquid lamella. Once retracted, radial momentum is converted upwards, causing drops to rebound off the surface (63,96). However, drop rebound is potentially more damaging compared to shatter for two reasons. Firstly, retraction of the liquid lamella results in a two-fold increase in shear stress (98). Secondly, pressure changes during rebound results in a second peak of impact stress (99).

The We_c for drop shatter is influenced by surface traits, with high hydrophobicity and HR promoting shatter (97,100–102). However, a large proportion of drop impact experiments are conducted on solid surfaces, where the influence of elasticity is minimal . Surface elasticity increases the We_c for shatter, due to the absorption of kinetic energy via elastic deformation (83,84,103). Consequently, it is imperative to consider surface elasticity when selecting an appropriate model for biomimetic fabrication.

1.6 Aims and Rationale

Lepidoptera, characterised by the chitin scales covering their wings and body, are ecologically important organisms, often used as markers of ecological instability (104). The surface of lepidopteran wings exhibits HR, comprising a highly-ordered scale-layer, in which neighbouring scales overlap both laterally and longitudinally (105,106). The surface of individual scales is ‘mesh-like’, comprising submicrometric longitudinal ridges (LR) interconnected by horizontal crossribs (CR) to form periodic ‘windows’ (106,107). Further roughness is constituted by nanoscale ridges (NR) which are found within microgrooves created by LRs (93).

Lepidopteran wing scales constitute a multi-functional surface with optical, acoustic and non-wetting functionality.

1.6.1 Optical functionality

The striking iridescent blue colouration observed on the wings of *Morpho* butterflies, is a direct result of the manipulation of light propagation by scales (108–110). LRs upon *Morpho* scales are formed by stacked chitin lamellae, and act as multi-layered reflectors of blue light (wavelength

range: 450 – 495 nm) (109,110). Structural colouration creates a highly conspicuous visual signal which plays an important role in both inter- and intraspecies communication, including mate recognition and the deterrence of visual predators (111,112).

1.6.2 Acoustic functionality

The wing scale-layer of earless moths constitutes an extremely effective sound-absorbing coating, providing moths with acoustic crypsis against echolocating bats (113,114). High porosity and hierarchical structuring causes scales to resonate in response to specific frequencies of acoustic stimulation (106,114). Scale resonance converts sound wave energy into vibrational energy or heat, which reduces the reflection strength of echolocation calls (106). Regional variation in scale structure across wings, causes independent tuning of scales to different resonant frequencies (106,114). Coupling of independently tuned neighbouring scales, via the wing membrane, results in broadband sound absorption across the range of echolocation frequencies used by bats (113,114). Consequently, the acoustic target strength of earless moths is extremely low, which significantly reduces their detectability.

1.6.3 Non-wetting functionality

Lepidopteran wings are classified as a superhydrophobic surface (CA >150°; RA <5°), which is highly self-cleaning (particulate removal ~86.7 % - 88.0 %) (105,115–117). Furthermore, drop shedding is directional, with low retention in an outward direction (towards the wing apical edge) and higher retention in an inward direction (towards the wing joint) (48,118). Directional drop shedding is attributed to longitudinal asymmetry within the scale-layer at two levels: (i) ‘sawtooth’ patterned LRs composed of overlapping chitin lamellae; (ii) an outward ‘stepwise’ hierarchy formed by longitudinal overlapping of neighbouring scales (118,119).

Longitudinal asymmetry, results in directional drop shedding by manipulating the detachment and reattachment of the three-phase contact line (120–123). During outward shedding (following longitudinal asymmetry), drops rest on the tips of periodic surface features, resulting in a small contact area (Figure *1*d, *Left panel*). Consequently, gravitational inertia exceeds adhesion, initiating drop movement at low RAs (118,121,124). In contrast, during inward shedding (against longitudinal asymmetry), periodic surface features form energy barriers against the advancing contact line, resulting in a large contact area (Figure *1*d, *Right panel*). Consequently, adhesion exceeds gravitational inertia, and thus a higher RA is required to initiate drop movement (118,121,124).

Directional drop shedding from lepidoptera wings has high fitness benefits, minimising both the energetic and thermoregulatory costs of water accumulation on the thorax, thereby optimising flight efficiency (115,118,125), and thus is expected to be a highly prominent phenomenon throughout the lepidoptera taxa. However, current literature exploring lepidopteran wing wettability focuses on butterflies (48,115,117–119,125), likely a result of unconscious biases towards charismatic species (126). Yet, butterflies constitute only a small proportion of documented lepidoptera species (127), and thus comprehensive understanding of wing wettability, particularly regarding directional drop shedding, is limited.

This study aims to comprehensively survey the wettability of *Attacus* moth wings. *Attacus* moths were selected for their size, ecology and availability. Using the existing literature on lepidopteran wing wettability (48,105,115–117,119,125), and the documented HR of *Attacus atlas* scales (128), it was hypothesised that the *Attacus* wing scale-layer would be classified as a superhydrophobic surface which exhibits directional drop shedding (Hypotheses 1 and 2).

1.6.4 Impact resilience

Previous studies on lepidopteran wing wettability have given little attention to the effects of drop impact (95). Damage of *Attacus* wings is directly linked to fitness (129). For example, membrane damage, such as cracking or fracturing, is extremely costly to flight because of a reduced ability to generate upward lift (129,130). Additionally, drop impact may result in the deterioration of HR, particularly through the loss of scales. Whilst having minimal aerodynamic consequence, scale loss deteriorates sound absorption, which leads to an increase in the detectability of moths by predatory bats (114,131).

Therefore, using inferred costs of impact damage, it was hypothesised that *Attacus* wings exhibit non-elastic resilience to impact damage via the induction of drop shatter (Hypothesis 3). However, despite resilience, impact and shear stresses are not eliminated completely, as demonstrated by solid surfaces (49,53,58,60), and thus damage is predicted to gradually accumulate over repeated impacts. Consequently, it was hypothesised that passive impact resilience of *Attacus* wings would degrade over frequent exposure to drop impacts (Hypothesis 4).

1.6.5 Regional effects: Surface wettability

Unlike butterflies, moth wings demonstrate regional variation in scale morphology (107,114). Generally, moth wings become gradually ‘furrier’ towards the thorax because of elongated basal scales, which are more ‘hair-like’ compared to shorter ‘paddle-like’ apical and discal scales (107). Increased ‘furriness’ within the basal region is attributed to the acoustic concealment of

wing joints, which may function as corner reflectors producing strong ultrasonic signals (132,133).

The effect of regional scale variation on surface wettability is unclear, limited to one study by Wagner, Neinhuis and Barthlott (125), which reported that apical CAs were larger compared to basal CAs. However, regional variation in surface structures configuring specific wettability patterns across leaf surfaces have been documented (134–136). For example, *H. populifolius* leaves exhibit dichotomous regional wettability, which enhances drainage. The open leaf surface is strongly hydrophobic, facilitating drop shedding, whereas veins are strongly hydrophilic, resulting in pinning of drops (136). The functionality of this phenomenon remains unclear. However, drop pinning on veins may cause leaves to become weighed down, thereby increasing the inclination angle, and thus the ease at which drops are shed from the open surface (125). However, dichotomous wetting represents an extreme example of regional wettability, and is therefore unlikely in *Attacus* wings, given their chemical homogeneity (125).

Basal scales resemble trichomes, an extremely well-documented hair-like surface structure upon leaves (137–139). The wettability of 'hairy' plant surfaces is dependent on trichome density (140). For example, the trichome layer on the upper surface of *Salvinia* leaves is extremely dense, resulting in a low height-distance-ratio between surface features. Consequently, drops cannot easily penetrate between trichomes via capillary action (31,140), resulting in a small contact area, and thus the surface is classified as superhydrophobic (CA >150°).

Basal scales are similarly densely packed (133). It is therefore predicted that elongated basal scales of *Attacus* wings will constitute an equally hydrophobic surface compared to paddle-like discal and apical scales. However, basal scales are less regularly organised, due to increased flexibility resulting from a high aspect ratio morphology (132,133,138). Therefore, it was hypothesised that basal scales will constitute decreased longitudinal asymmetry, resulting in a lower magnitude of directional shedding (Hypothesis 5.1).

1.6.6 Regional effects: Impact resilience

Regional variation in *Attacus* scale morphology may additionally affect resilience to damage, a prediction motivated by existing observations of drop impact on 'hairy' plant surfaces (6,98,138,139). Like basal scales, trichomes have a high aspect ratio, enabling elastic deformation in response to the hydraulic pressure of drops, which 'cushions' leaves against impact (138,139). Given their structural similarities, basal scales may exhibit comparable elastic responses, thereby reducing the magnitude of impact stress. It can therefore be predicted that the

basal region of *Attacus* wings will exhibit a greater resilience to damage compared to the discal and apical regions (Hypothesis 5.2).

1.6.7 Effects of transparency on wettability

The wings of *Attacus* moths contain triangular optically transparent patches, known as transparent windows (TW). Optical transparency is defined as the complete transmission of light with minimal reflection and absorption (141). The development of anti-reflective coatings to maximise the efficiency of light dependant technologies, such as solar cells, represents a significant area of interest in the biomimetic field (142,143). Multi-functional anti-reflective coatings which are also self-cleaning are particularly important regarding long-term efficiency for two reasons: (i) accumulated water increases light reflectance forming 'glare'; (ii) the accumulation of particulates forms a barrier against light transmission (as reviewed by Motamedi, Warkiani and Taylor) (141).

Complete or partial transparency is well documented across lepidoptera (144–146). However the effects of transparency on wettability remains unclear. Generally, transparent regions exhibit reduced scale density (145,146), which increases the height-to-distance ratio between roughness features (29–33). Additionally, functional differences between transparent and opaque regions mean scales are likely to vary in morphology and surface structure. For example, the TW of *Rothschildia lebeau* (a close relative of *Attacus moths*) contains small piliform scales rather than typical paddle-like scales (147). It is therefore predicted that drops are more likely to sink into roughness features via capillary action, resulting in a large contact area (31,140). Consequently, it was hypothesised that scales within the *Attacus* TW will constitute a less hydrophobic surface compared to the apical, discal and basal regions (Hypothesis 6.1).

Additionally, a lower height-to-distance ratio between neighbouring scales results in a lower degree of longitudinal overlapping, and thus reduced asymmetry (118,121,124). Therefore, it was hypothesised that drop shedding from the TW will be less directional (Hypothesis 6.1).

Reduced surface hydrophobicity and HR increases the We_c threshold for drop shatter (97,100–102). Additionally, a reduced scale-layer may increase the susceptibility of the TW to an impact-driven Cassie-to-Wenzel transition (75,148). Consequently, it is hypothesised that transparent regions will demonstrate reduced drop shatter, and thus lower resilience against damage and increased surface wetting compared to opaque regions of *Attacus* wings (Hypothesis 6.2 and 6.3)

1.7 Hypotheses and predictions

During this study, the following hypotheses and predictions were tested:

Hypothesis 1: The scale-layer of *Attacus* wings constitute a superhydrophobic surface.

1. Contact angles measured from sessile drops upon *Attacus* wings will be >150°.
2. Retention angles measured when tilting *Attacus* wings will be <5°.
3. In the absence of scales, *Attacus* wings will be less hydrophobic, with contact angles <150° and retention angles >5°.

Hypothesis 2: The shedding of drops from *Attacus* wings is directional, following scale organisation.

1. The organisation of *Attacus* scales favours outward shedding of drops (towards the apical edge).
2. Retention angles will be smaller when tilting wing samples in an outwards direction compared to an inwards (towards the thorax) or lateral direction (perpendicularly across scales).
3. In the absence of scales drop shedding will be non-directional.

Hypothesis 3: The scale-layer of *Attacus* wings constitutes a 'shatter-coating', producing less damaging drop impacts.

1. The scale-layer diffuses drop impact through shatter and radial ejection of satellite droplets.
2. Absence of scales reduces 'shatter-coating' efficacy.
3. A reduced 'shatter-coating' increases surface wetting.

Hypothesis 4: The mechanical stress of drop impact causes damage of the scale layer of *Attacus* wings.

1. Repeated drop impact causes the scale-layer to become more disordered.
2. Accumulation of scale-layer damage gradually degrades the 'shatter-coating', reducing its efficacy.

Hypothesis 5: The wettability of *Attacus* wings varies across different wing regions.

1. Differences in the regularity between paddle-like scales of the apical and discal regions, and elongated scales of basal regions, causes variation in the directionality of drop shedding.
2. Differences in scale structure causes wing regions to vary in their susceptibility to damage by impacting drops.

Hypothesis 6: The wettability of transparent wing regions differs from opaque regions.

1. A reduced scale-layer density in transparent regions causes reduced hydrophobicity compared to opaque regions, with contact angles <150° and retention angles >5°.
2. Transparent regions have a reduced shatter-coating, causing drop impacts to be more damaging.
3. Transparent regions have a reduced shatter-coating, and thus are more susceptible to surface wetting.

Chapter 2. Materials and Methods

2.1 Sourcing of specimens

Attacus atlas, Attacus lorquinni and *Methona confusa* specimens were purchased as pupae from https://butterflypupae.com between December 2022 – March 2023. Initially, it was planned to use only *A. atlas* moths as a model species to survey wing wettability. However, during the experimental period *A. atlas* pupae became unavailable from the retailer, so the sample size was supplemented with *A. lorquinii,* a closely related species of the same genus. *M. confusa* butterflies were purchased as an optically transparent control species for comparisons between transparent and opaque regions of *Attacus* wings.

Pupae were reared in temperature-controlled insect cabinets (Economic Deluxe, Snijders, Tilburg, Holland), under constant temperature (30°C), humidity (70 %), and a 12h day/night cycle, until emergence as adults. Upon emergence, specimens were euthanised via CO_2 freezing at -18°C to preserve the condition of the wing scale-layer. After euthanasia, specimens were stored at -18°C throughout the experimental period to prevent loss of wing elasticity through desiccation.

A standard sample size of N= 10 was used to represent *Attacus* moths in all experiments. Originally, 10 specimens were also planned to represent *M. confusa* butterflies. However, rearing difficulties meant that a large proportion of specimens either died before emergence, or emerged with wing deformations, and were therefore not included. Therefore, a standard sample size of N= 6 was used to represent *M. confusa* butterflies within experiments.

2.2 Classification of scale structure

Scanning electron microscopy (SEM) was used to characterise and compare the surface structure of scales, in addition to the tiling patterns of scale-layers across the apical, discal, basal and TW regions of *Attacus* wings (Figure 2a), and the discal region of *M. confusa* wings (Figure 2b).

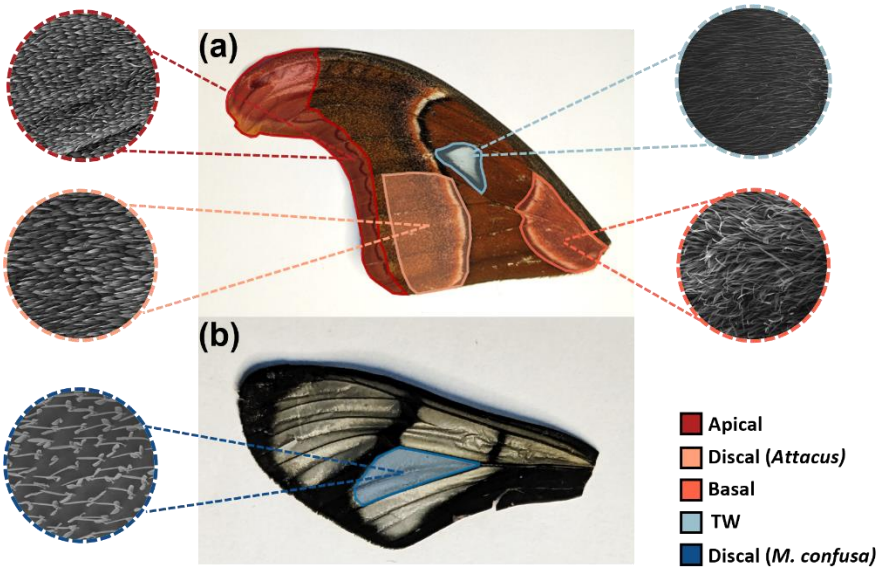

Figure 2. A visual representation of regions sampled. (a) Photograph of an *Attacus atlas* moth wing with the apical, discal, basal and transparent window (TW) highlighted. (b) Photograph of *Methona confusa* butterfly wing with the discal region highlighted. Round insets show scanning electron microscope images of the dorsal scale-layer of each region sampled.

3 mm x 3 mm (width x length) wing samples were mounted onto 12.7 ⌀ aluminium stubs (Zeiss) using adhesive carbon tabs (EM Resolutions). Mounted samples were sputter-coated with gold at standard thicknesses: 14 nm (*Attacus*: basal), 8 nm (*Attacus*: apical, discal and TW; *M. confusa*: discal) (Quorum Q150R E5, Quorum Technologies). Samples were imaged under high vacuum using an SE1 detector at a standard working distance of 8.5 mm. Images were taken over a magnification range of 80x – 15’000x using an electron high tension of 25’000 kV and a 100 Pa probe.

Imaging was conducted for dorsal samples taken from the forewings of *Attacus* and *M. confusa* specimens under three treatments: fully-scaled, descaled and damaged. Descaled samples were prepared by removing scales from the membrane using acoustic foam (Basotect W, BASF), fashioned into an angled tool. Damaged samples were taken from wings subjected to 150 repeated drop impacts.

2.3 Classification of surface wettability

2.3.1 Sample preparation

6 mm x 10 mm samples were excised from the apical, discal, basal and TW regions of *Attacus* forewings, and the discal region of *M. confusa* forewings, using a razor blade. Existing patches of scale-layer damage accumulated between emergence and preservation of specimens, via

contact with the net cage or conspecific encounters, were avoided when excising samples to limit potential confounding effects. Heavily damaged specimens were excluded completely. CAs and RAs measurements were conducted under two sample treatments: fully-scaled and descaled.

2.3.2 Contact angles

CAs were measured using the sessile drop method (149,150). The experimental setup consisted of a bespoke clamp comprising two plates held together by binder clamps. The upper plate contained a 6 mm semicircular opening, into which the prepared wing samples were affixed using double-sided tape (Figure 3a). The hemispherical opening of the clamp was placed adjacent to a right-angled mirror (L= 25.0 mm; THORLABS; Munich, Germany), which rested on a foam plinth (30 mm x 30mm x 15mm) to ensure that the base of the mirror was aligned with the wing sample (Figure 3b). The experimental set-up was assembled on the stage plate of a dissection microscope (Leica M205m; Wetzlar, Germany) fitted with a GT Vision GX CAM hichrome MET-M camera (Suffolk, England) so that the lens was aligned with the right-angled mirror.

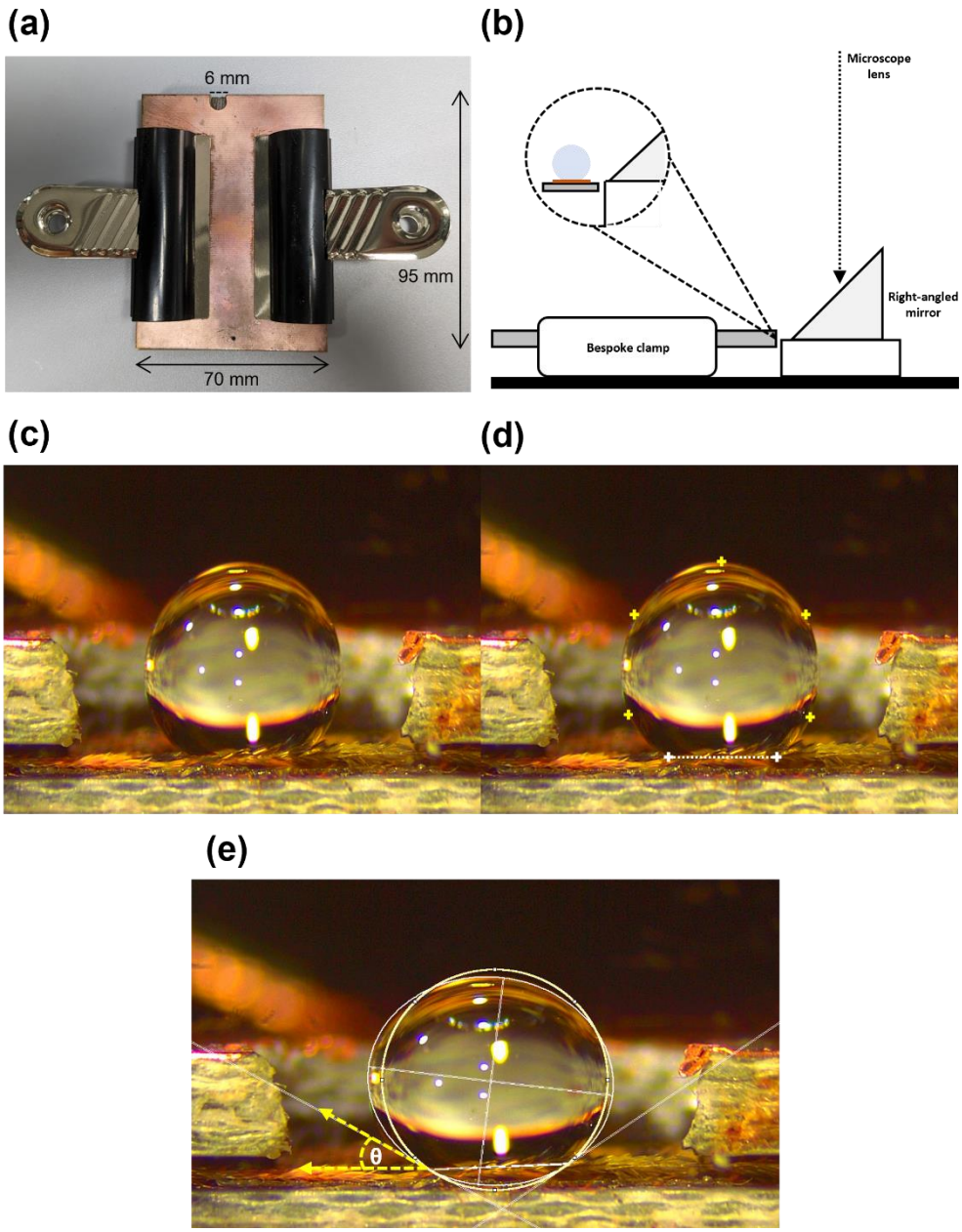

Figure 3. The experimental set-up used for measuring contact angles. (a) Photograph of the bespoke clamp used for contact angle measurements. Excised wing samples were fixed in a 6 mm semicircular opening. (b) A visualisation of the experimental set-up used to take calibrated images of sessile drops. The experimental set-up was assembled on the baseplate of a dissection microscope (represented by the black box). The black arrow represents the viewpoint of a Leica dissection microscope fitted with a camera. Circular inset demonstrates the alignment of a right-angled mirror (represented by a grey triangle) with sessile drops placed upon affixed wing samples; (c) Calibrated image taken of a sessile drop upon the discal scale-layer of an *Attacus* wing taken at 0.6x magnification; (d) Identification of drop boundary (represented by yellow '+'s) and the solid-liquid tangent (represented by white '+'s) during ImageJ analysis of calibrated images. (e) The circle-of-best-fit calculated using drop boundary and solid-liquid tangent points identified during analysis of calibrated images. Yellow arrows represent the output of the fitted model, known as theta (θ).

A 16 µl (⌀ = 3.77mm) drop of water was gently placed onto samples using a 0-20 µl micro-pipette. Subsequently, the drop's position was adjusted towards the front edge of the clamp using an insect pin. This ensured that CAs were not obstructed by the clamp baseplate. Calibrated images (.JPEG) were then taken of drops at 0.6x magnification (Figure 3c). Following imaging, drops were removed from samples via shedding by tilting the clamp downwards. Any excess water was then removed via capillary action using a paper towel before samples underwent a two-minute drying period. This process was repeated three times for each sample.

Calibrated images of sessile drops were analysed using ImageJ (ImageJ, NIH). During analysis, the γ_{SL} tangent was manually marked, using the wing membrane as reference. Next, five points were marked at regular intervals along the drop boundary (Figure 3d). A circle-of-best-fit was then fitted to drops using the specified boundary points, yielding an output value known as theta (θ) (Figure 3e). CAs were the calculated by subtracting θ from 180. Analysis was repeated three times per image, and an average taken.

2.3.3 Cupping

Upon analysis of calibrated images, it was observed that scales tended to become 'attracted' to the drop boundary, forming a 'cup-like' configuration (Figure 4a). This phenomenon was termed 'cupping'.

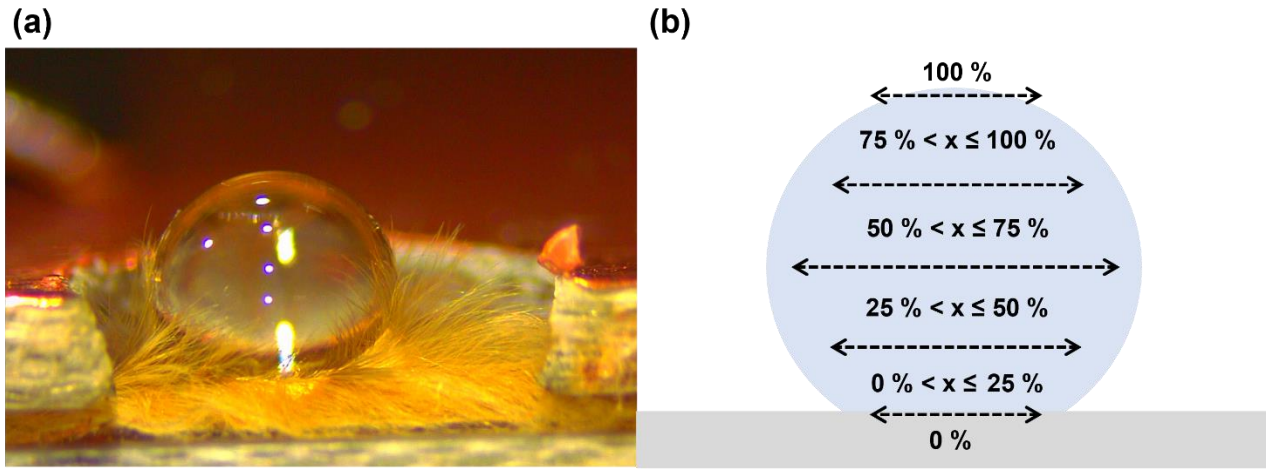

Figure 4. (a) Calibrated image of 'cupping' of a sessile drop by basal scales on an *Attacus* wing taken at 0.6x magnification. (b) A visual representation of the categories used to quantify the magnitude of cupping by scales across different regions of *Attacus* wings.

The magnitude of cupping by scales across *Attacus* wings was quantified by dividing drops into four segments. Images were then classified into six catergories based on the segment in which the highest proportion of scales were observed. The catergories are as follows: (i) 0 % (no cupping); (ii) 0 % < cupping ≤ 25 %; (iii) 25 % < cupping ≤ 50 %; (iv) 50 % < cupping ≤ 75 %; (v) 75 % < cupping ≤ 100 %; (vi) 100 % (complete cupping) (Figure 4b).

2.3.4 Retention angles

Drop RAs were measured using a modified manual rotation stage (35.6mm; THORLABS; Munich, Germany), vertically mounted onto a Perspex weight. This was secured onto a workbench using a bar-clamp. A Perspex plinth was affixed to the front of the rotation stage upon which a microscope slide was attached using double-sided tape (Figure 5a). To ensure that wing samples were consistently oriented in the same direction, the microscope slide was labelled with an arrow.

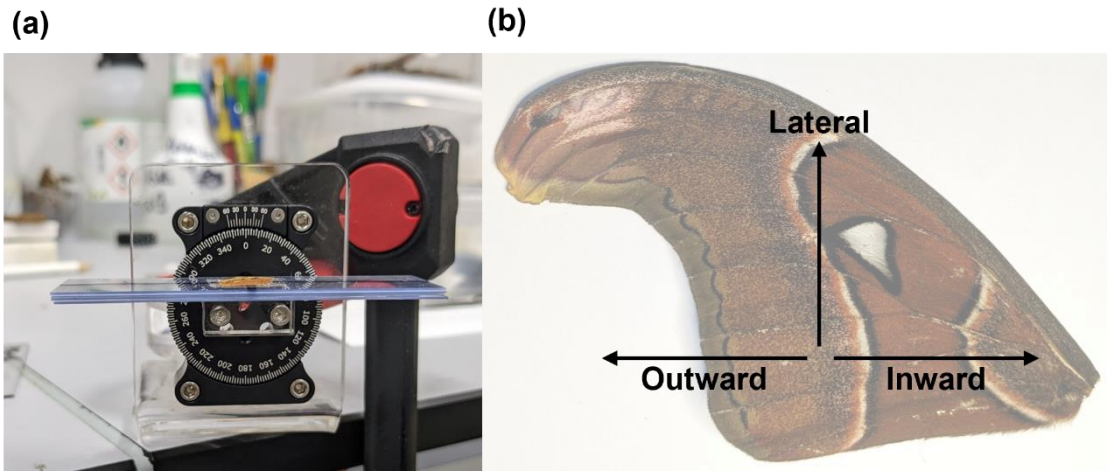

Figure 5. (a) The modified rotation stage used to measure drop retention angles in three directions: outwards (stage turned right), inwards (stage turned left) and laterally (microscope slide mounted perpendicularly and stage turned right). (b) A visual representation of the three tilt directions: outward (towards the apical edge), inward (toward the wing base) and lateral (perpendicularly across longitudinal veins) used to measure retention angles from *Attacus* wings.

The rotation stage was set to 0°, and a 16µl drop was gently placed onto the wing sample using a pipette, and then centred with an insect pin. Subsequently, the rotation stage was slowly rotated until drop movement was initiated, at which point the angle was recorded. In instances where no drop movement was observed, the retention angle was recorded as 90°.

The directionality of drop shedding was tested by tilting wing samples in three directions: outwards (toward the apical edge), inwards (toward the wing base) and lateral (perpendicular to venation) (Figure 5b). For lateral tilting, the microscope slide was turned 90° and affixed along the short edge. After recording RAs, excess water was removed, and wing samples underwent a two-minute drying period. Each sample was subjected to three repeat measurements, and an average was calculated.

2.4 Classification of impact resilience

2.4.1 Sample preparation

To minimise elastic responses, such as downward flexion, the forewings of *Attacus* and *M. confusa* were placed into a bespoke clamp. This consisted of a solid copper baseplate (72 mm x 100 mm), a lower layer of acoustic foam affixed to the baseplate (72 mm x 100 mm x 15 mm), an upper detachable layer of acoustic foam (72 mm x 90 mm x 10 mm), and a cork C-clamp (25 mm opening) (Figure 6a). The highly permeable acoustic foam layers permitted the drainage of excess water, thereby reducing the likelihood of waterlogging. A cork C-clamp was used for its sufficient rigidity to hold wings securely, whilst maintaining enough flexibility to prevent tearing of the wing membrane.

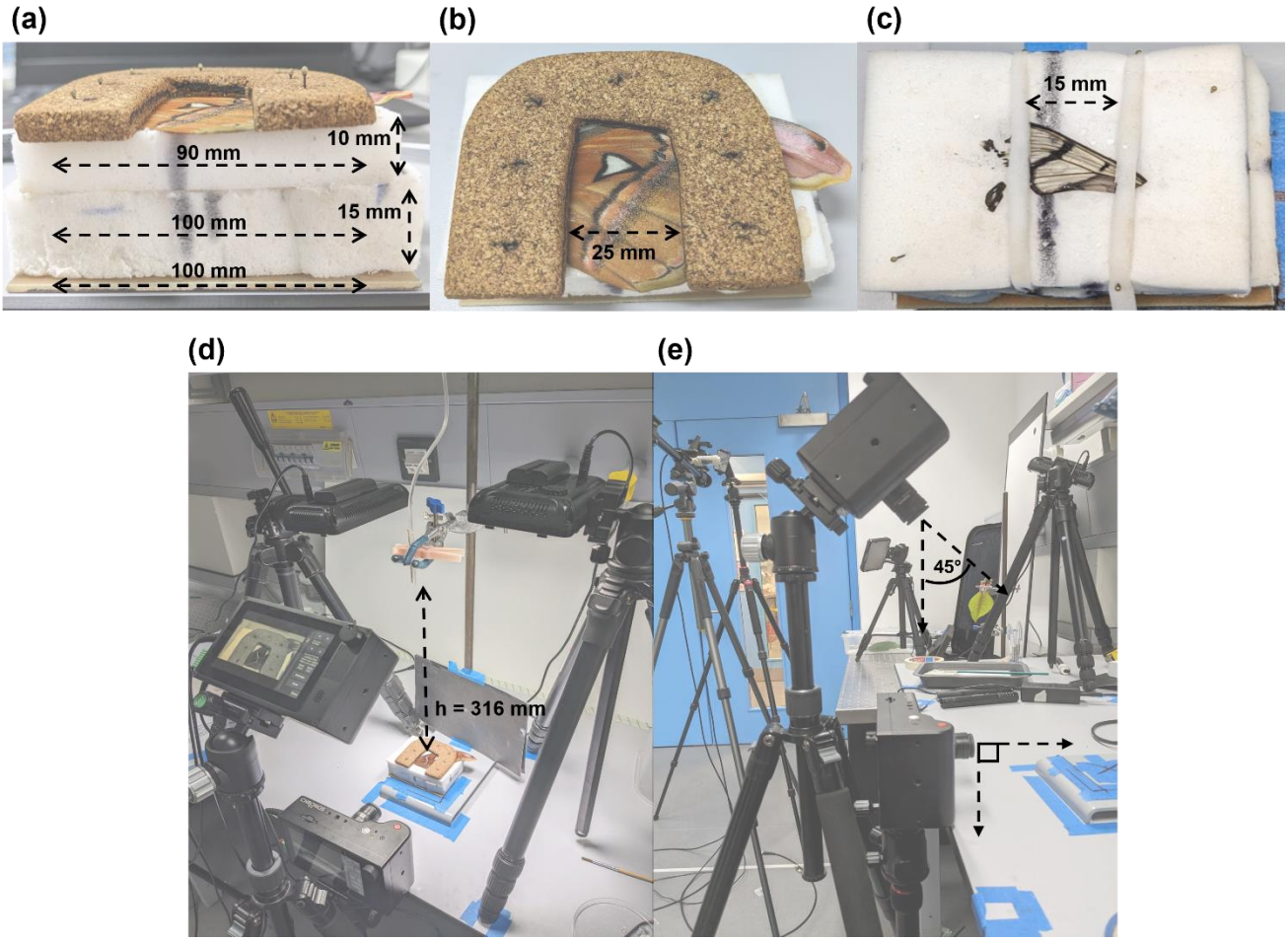

Figure 6. Experimental set-up used for measuring impact resilience. (a) Photograph of the bespoke clamp used to hold wings during impact studies taken from a parallel viewpoint. The clamp consisted of a solid copper baseplate, a lower layer of acoustic foam, an upper detachable layer of acoustic foam, and a cork C-clamp.; (b) Photograph taken of an *A. lorquinni* wing secured in the bespoke clamp. (c) Photograph of acoustic foam brackets used for securing *M. confusa* wings. (d) Experimental set-up used for recording drop impacts; (e) Photograph of downward and parallel camera positioning used for recording drop impacts.

Attacus wings were secured between the upper foam layer and the C-clamp using seven insect pins, with the region of interest positioned in the centre of the clamp opening (Figure 6b). *M. confusa* wings were considerably smaller than *Attacus* wings and were not held as securely within the C-clamp. This resulted in wings shifting position during impact, limiting the accuracy of results over repeated impacts. A smaller cork C-clamp was trialled. However, use of a smaller C-clamp was not deemed appropriate, as radial spreading of drops was obstructed by the sides of the clamp. Instead, *M. confusa* wings were secured by two brackets fashioned from acoustic foam (Figure 6c).

2.4.2 High-speed videography

Impact resilience was measured using high-speed videography of drops colliding with the discal, basal and TW regions of *Attacus* wings, and the discal region of *M. confusa* wings under two treatments: fully-scaled (*Attacus*: discal, basal and TW; *M. confusa*: discal) and descaled (*Attacus*: discal and TW).

Drops were generated at a standard rate of 120 ml/h using a modified hospital drip (4.1 lumen; Exadrop, B. Braun, Melsungen AG, Germany) positioned 316 mm above wings (h) (Figure 6d). Drops had a mean volume of 0.066 mL and fell at a mean impact velocity of 0.76 m/s, and a *We* of 27.58. Pilot drops were used to identify the drop impact site, which was marked with an 'X'. The wing clamp was then centred over the marked 'X' before a bracket was constructed using Scotch tape. This ensured that the positioning of wings was standardised throughout the duration of impact experiments. Once positioned, wings were illuminated using two LED lighting panels to maximise the depth of field and minimise the formation of shadows (Figure 6d).

Drop impacts were recorded using two Chronos 1.4 high-speed cameras (CR14-1.016M, Kron Technologies Inc., Burnaby, California) mounted in two positions: (i) in parallel with wings; and (ii) above wings at a 45° downward angle (Figure 6e). Wings were subjected to 150 repeated drop impacts, with recordings taken of the 1st impact, followed by regular intervals of 30 impacts (30, 60, 90, 120, 150). Between recordings, residual water was removed from wings using a paper towel, followed by a two-minute drying period. Impact videos were saved as image stacks (.TIFF) for analysis.

2.4.3 High-speed video analysis

Initial viewing of recorded videos demonstrated that drops shattered upon impact with wings. Drop shatter was quantified using frame-by-frame analysis to measure the frequency of three inferential impact metrics (i) nucleation of the spreading liquid lamella (Figure 7, *Left panel*); (ii) the presence of residual drops remaining within the impact site after shatter (Figure 7, *Centre panel*); and (iii) instances of surface wetting (Figure 7, *Right panel*). These metrics were chosen to represent the impact dynamics of colliding drops, including shatter (nucleation), lateral ejection of satellite drops (residual drops) and deposition of drops (surface wetting).

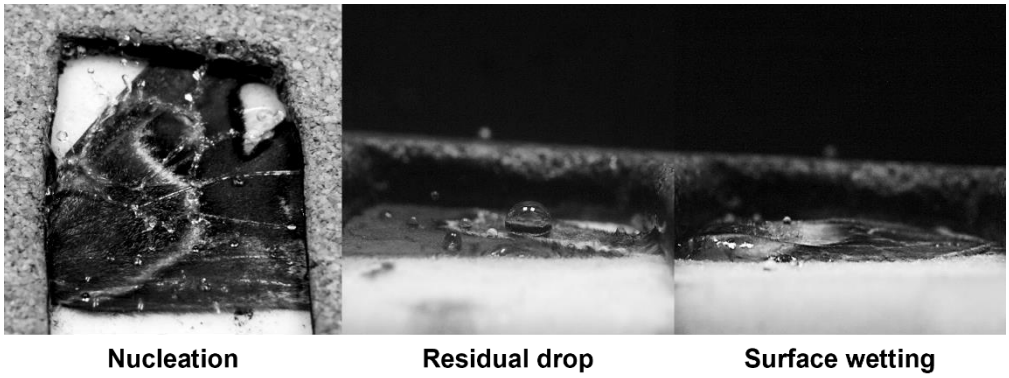

Figure 7. Photographs of inferential metrics (nucleation of the liquid lamella; residual drops remaining with the impact site; surface wetting) used to classify impacts on *Attacus* and *M. confusa* wings.

The frequency of impact metrics was recorded using a binary ranking system: yes = 1, no = 0. Ranking of impact metrics was conducted for videos taken of the 1st impact (intact wings) and the 150th impact (damaged wings). Impact metric frequencies were then accumulated for each region and recorded as a proportion (%), to minimise skewed statistics resulting from unequal sample sizes.

2.4.4 Quantification of damage accumulation

The damage accumulated across the discal, basal and TW regions of *Attacus* wings in response to repeated drop impact was quantified through the analysis of calibrated images (.JPEG) captured in conjunction with capture of high-speed videos. Prior to impact exposure, preliminary images were taken of wings using a dissection microscope fitted with a GT Vision GX CAM hichrome MET-M camera. Subsequent images were then taken at regular 30 impact intervals until wings had experienced a total of 150 drops (30, 60, 90, 120, 150). To ensure consistent alignment of consecutive images, the wing clamp was placed into a custom-bracket constructed on the microscope baseplate.

When imaging opaque regions (discal and basal), the entire wing clamp was placed into the bracket and illuminated using incident and oblique light sources. Conversely, when imaging the TW, increased glare, and low contrast of scales had to be considered as confounding factors. To mitigate this, the upper foam-layer of the clamp was detached and placed in the bracket, allowing for wings to be back-lit using transmission light. To prevent misalignment over repeated imaging, the baseplate bracket was adjusted to the dimensions of the upper foam-layer. Additionally, both the upper and lower foam-layers were marked on the length and width with a permanent marker to ensure consistent reattachment. After imaging, consecutive images of each wing region were compiled and stored as image stacks.

2.4.4.1 Scale-layer disorganisation

The effect of repeated drop impact on the organisation of the discal and basal scale-layers of *Attacus* wings was quantified by analysing the circular distribution of scales observed in calibrated images taken of intact and damaged wings. Image analysis was conducted using the MATLAB Image Processing and Computer Vision Toolbox (Version 11.7, The MathWorks INC). Before analysis, the impact site was isolated by cropping images to a standard size (450 x 500 pixnels) (Figure 8a).

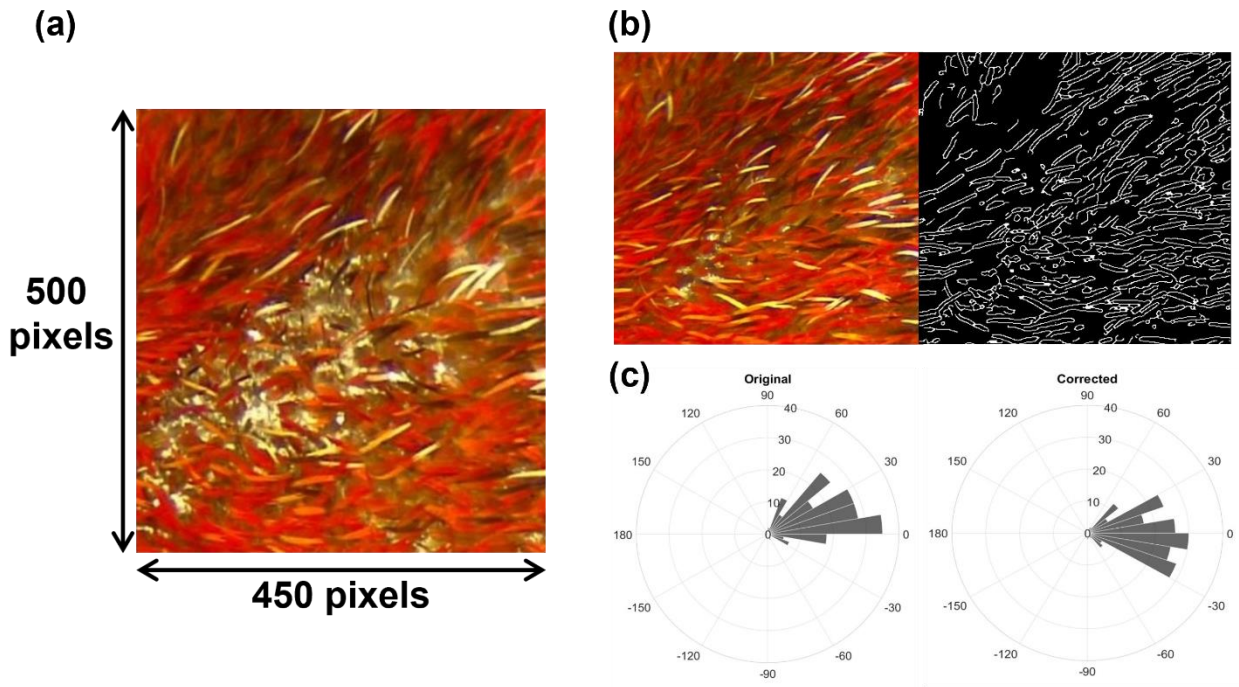

Figure 8. Orientation analysis conducted on calibrated images of *Attacus* wings. (a) Calibrated image of the drop impact site within the basal region of an *Attacus* wing after 150 impacts; (b) Identification of individual scales within the basal scale-layer using a Canny edge detector. (c) Polar histograms representing the circular distribution of basal scale orientations extracted from an edge detection before and after the application of an alignment correction.

Individual scales within images were identified via the application of a ‘Canny’ edge detector (Figure 8b). A ‘Canny’ edge detector was selected over other methods, such as ‘Sobel’ or ‘Prewitt’, for its high robustness against false edges. The edge detector output was further refined by applying the morphological operations: ‘imdilate’ (edge enhancement) and ‘imerosion’ (noise reduction), using a diamond structuring element (size 1).

The ‘regionprops’ function was then employed to extract orientation values of identified scales, which were subsequently stored as angles (range: -90° to 90°). Discrepancies in image alignment between wings was corrected by calculating the circular mean of stored angles, and then subtracting this value from each individual angle (Figure 8c). The corrected angles extracted from all wings were compiled based on region (discal or basal), and treatment (intact or damaged).

To minimise sample size-based bias, the extraction of orientation values from each image was restricted to a standard value based on the highest common number of edges found for each region: discal= 190 edges, basal= 120 edges.

2.4.4.2 Scale-layer damage

The accumulation of scale-layer damage within the basal, discal and TW regions of *Attacus* wings was quantified by analysing the pixel variance (%) between intact (preliminary images) and damaged wings (subsequent images taken at 30, 60, 90, 120 and 150 intervals of repeated impact). Image analysis was conducted in MATLAB and adapted from methods outlined in the: ‘Feature detection and extraction;’ and ‘Find image rotation and scale using automated feature matching’ documentation.

Matched surface features between intact and damage wings were identified via the application of a KAZEfeature detector (Figure 9a). A KAZEfeature detector was selected over alternative methods, such as SURFfeatures, due to a high robustness, resulting in a large output of identified matched points between images. Next, geometric transformations were employed to align images using the identified matched points (Figure 9a & b). Image alignment was used to correct for possible translation errors accumulated during the imaging of wings.

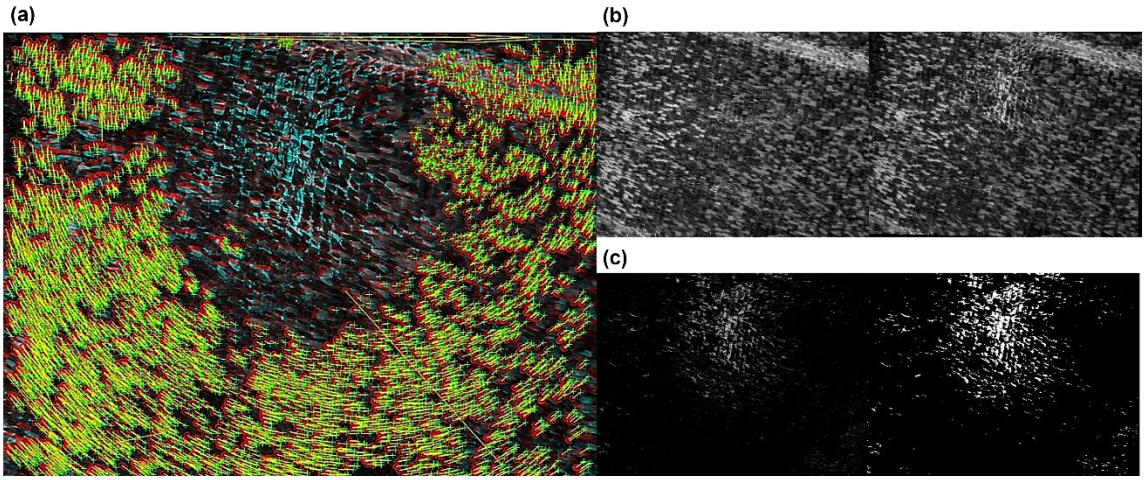

Figure 9. (a) Output matching surface features identified by a KAZEfeature detector between images of the discal scale-layer of *Attacus* wings under two treatments: intact (0 impacts) and damaged (150 impacts). Red 'O' and green '+' represent identified matched features; yellow lines represent the distance between matched points caused by differences in image alignment. (b) Aligned 'intact' and 'damaged' images after geometric transformations using matched surface features. (c) *Left panel.* Isolated impact site obtained by subtracting pixels of intact images from damaged images after alignment. *Right panel*. Output binary mask (threshold = 01, area filter = 10 – 5000 pixels) applied to isolated impact site.

Following alignment, the impact site was isolated by subtracting the pixels of the intact image from those of damaged images (Figure 9c, *Left panel*). Next, a binary mask (threshold= 0.1, area filter= 10 – 5000 pixels) was applied to the isolated impact site (Figure 9c, *Right panel*). The binary mask area (in pixels) was then extracted using the 'regionprops' function. The output area was recorded as a proportion (%) of the total pixels within the image.

2.5 Statistical analysis

Generally, non-parametric statistical testing was conducted due to the non-normal distribution of data, and the presence of paired samples. Parametric tests were conducted for comparisons between CAs measured from fully-scaled and descaled samples, and regional comparisons of drop shatter. This was due to positive results when the assumptions of parametric statistics were tested. All statistical analysis was conducted in Rstudio (Version 1.4.1106, Rstudio).

2.5.1 Surface wettability

All statistical testing of surface wettability was conducted for the apical, discal, basal and TW regions of *Attacus* wings, and the discal region of *M. confusa* wings.

2.5.1.1 Effect of scale removal

The effect of scale removal on surface wettability was tested by comparing CAs and RAs measured from fully-scaled and descaled samples taken from *Attacus* and *M. confusa* wings, using paired T-tests and Wilcoxon matched-pairs rank sum tests respectively.

2.5.1.2 Regional effects: Surface wettability

The effect of region on the CAs and RAs measured across fully-scaled and descaled *Attacus* and *M. confusa* wings was tested using a Kruskal-Wallis test. In the event of a positive Kruskal-Wallis result ($p < 0.05$), pairwise comparisons were conducted using a Dunn test, with a Holm correction.

2.5.1.3 Regional effects: Cupping

The effect of region on the degree of cupping observed across *Attacus* and *M. confusa* wings was tested using a Kruskal-Wallis test, followed by pairwise comparisons conducted using a Dunn test.

2.5.1.4 Directionality of drop shedding

The effect of tilt direction (outward, inward and lateral) on RAs measured across fully-scaled and descaled *Attacus* and *M. confusa* wings was tested using a Kruskal-Wallis test, followed by pairwise comparisons using a Dunn test.

2.5.2 Impact resilience: Drop shatter

2.5.2.1 Effect of scale removal

The effect of scale removal on the frequency of impact metrics (nucleation, residual drops and surface wetting) observed during impacts with fully-scaled and descaled discal and TW regions of *Attacus* wings, was tested using McNemar tests.

2.5.2.2 Regional effects

The effect of region on the frequency of impact metrics observed across the fully-scaled discal, basal and TW regions of *Attacus* wings, and the discal region of *M. confusa* wings was tested using a Pearson chi-squared test of independence. In the event of a positive result ($p < 0.05$),

pairwise comparisons were conducted using Pairwise chi-squared tests, with a Bonferroni correction.

2.5.2.3 Effect of damage

The effect of 150 repeated impacts on the frequency of impact metrics observed for fully-scaled discal, basal and TW regions of *Attacus* wings, and the discal region of *M. confusa* wings, was tested using McNemar tests.

2.5.3 Impact resilience: Damage accumulation

2.5.3.1 Scale-layer disorganisation

The effect of 150 repeated impacts on the circular distribution of orientation values extracted from images taken of the discal and basal regions of *Attacus* wings, was tested using Watson's two-sample circular test.

2.5.3.2 Scale-layer damage

The effect of repeated impacts on the accumulation of damage within the discal, basal and TW regions of *Attacus* wings was tested using a polynomial regression. The pixel variance (%) calculated from images taken at 30, 60, 90, 120 and 150 impacts were plotted, and a regression model was fitted. The best fitted regression model was determined by conducting k-fold cross-validation tests on five possible models, wherein the degree of polynomial (h) differed. The regression model of best fit was determined by the h which produced the lowest mean-squared error (MSE). The regression models used were as follows: discal (h=3), basal (h=3), TW (h=1). Once the polynomial regression model was fitted, an analysis of variance (ANOVA) of the model was performed.

2.5.3.3 Regional effects: Total pixel variance (%)

The effect of region on the total pixel variance accumulated within the discal, basal and TW regions of *Attacus* over 150 impacts was tested using a Kruskal-Wallis test, followed by pairwise comparisons using a Dunn test.

Chapter 3. Results

3.1 H1: The discal scale-layer of *Attacus* wings constitutes a superhydrophobic surface

3.1.1 *Classification of the discal scale-layer*

Figure 10a and b illustrates the tiling patterns and surface structure of scales within the discal region of *Attacus* wings.

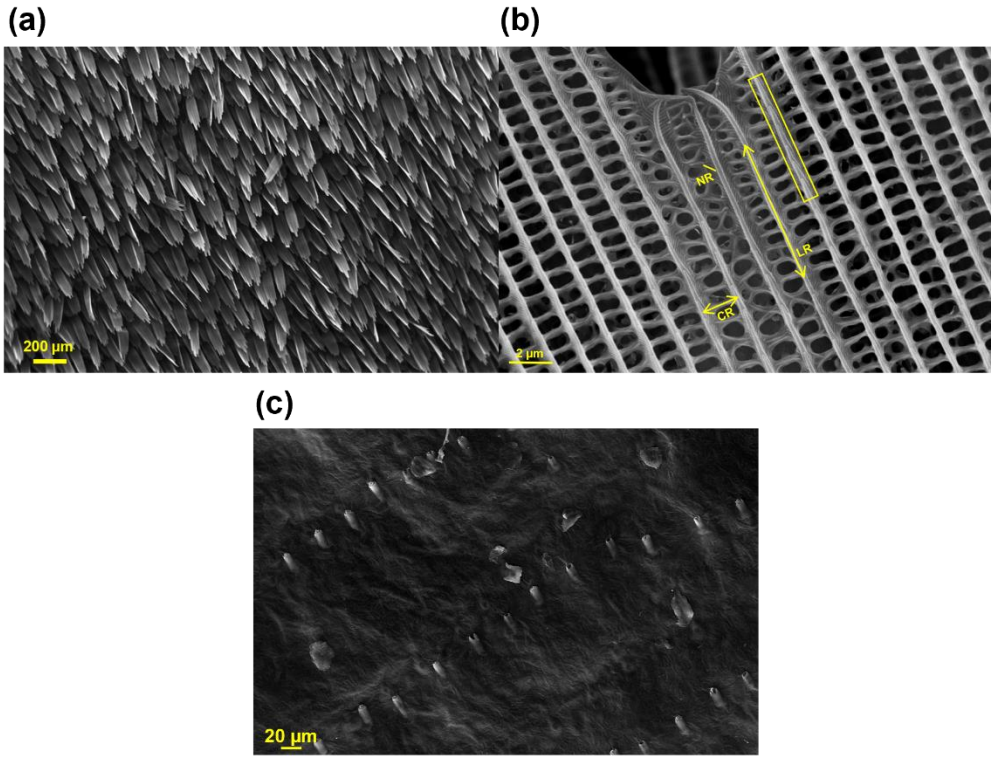

Figure 10. SEM images taken of the discal region of *Attacus* wings. (a) The 'shingle-like' organisation of the discal scale-layer taken at 80x magnification, (b) the hierarchical structure of discal scales taken at 12'000x magnification, comprising longitudinal ridges (LR), horizontal crossribs (CR) and nanoscale ridges (NR. Yellow box highlights 'sawtooth' patterning of LRs formed by overlapping cuticular lamellae. (c) the one-tier surface roughness of the descaled discal membrane at 100x magnification.

Discal scales were paddle-like and organised in lateral rows across the wing surface, with their longitudinal axis oriented in an outward direction (toward the apical edge). Neighbouring scales exhibited strong lateral and longitudinal overlapping, forming a closed-layer with an outward stepwise hierarchy (Figure 10a). The surface of discal scales demonstrated HR (Figure 10b). At the microscale, LR form microgrooves (mean width = 1.46 µm), which are interconnected by CR to form a mesh-like pattern. Within the microgrooves, NR were observed. LRs demonstrated a noticeable 'sawtooth' pattern, formed by overlapping cuticle lamellae, orientated towards the tips of scales.

3.1.2 Classification of the descaled discal membrane

Figure 10c illustrates the surface structure of the descaled discal membrane, demonstrating one-tier roughness, comprised of ridges (mean width = 195.7 µm) formed by scale insertion points organised into lateral rows.

3.1.3 Surface wettability

Table 1 presents CAs of sessile drops measured from discal samples under two treatments: fully-scaled and descaled.

Table 1. The contact angles (°) of sessile drops measured from the discal region of *Attacus* wings (N= 10) under two treatments: fully-scaled and descaled. The effect of scale removal was significant (p <0.001).

	Contact angle [°] (mean ± standard deviation)
Treatment	
Fully-scaled	144.4 ± 6.05
Descaled	99.2 ± 3.06
p-value	p<0.001***

Scale removal had a significant effect on recorded CAs (Paired T-test: $t_{(1,9)} = -15.8$, p-value = $7.1960e^{-08}$), with descaled CAs measuring 45.3° lower than fully-scaled CAs.

Table 2 presents the RAs measured by tilting fully-scaled and descaled discal samples in three directions: outward, inward and lateral.

Table 2.The retention angles (°) measured from the discal region of *Attacus* wings (N= 10), when tilting samples in three directions: outward (towards the apical edge), inward (towards the wing base), lateral (perpendicular to venation). Retention angles were recorded under two treatments: fully-scaled and descaled. The effect of scale removal was significant in all directions (p <0.01).

	Retention angle [°] (mean ± standard deviation)		
Treatment	*Outward*	*Inward*	*Lateral*
Fully-scaled	7.0 ± 2.88	14.4 ± 3.87	11.7 ± 5.56
Descaled	73.5 ± 4.24	73.0 ± 7.22	76.5 ± 7.66
p-value	p<0.01**	p<0.01**	p<0.01**

For all tilt directions, scale removal had a significant effect on recorded RAs (Wilcoxon matched-paired rank sum test: outward: V = 0, p-value = 0.0020; inward: V = 0, p-value = 0.0059; lateral: V = 0, p-value = 0.0020), with outward, inward and lateral descaled RAs being 66.5°, 58.6° and 64.8° higher respectively than fully-scaled RAs.

3.2 H2. The shedding of drops from the discal scale-layer is directional

Figure 11, illustrates the directionality of drop shedding from the discal region under two treatments: fully-scaled and descaled.

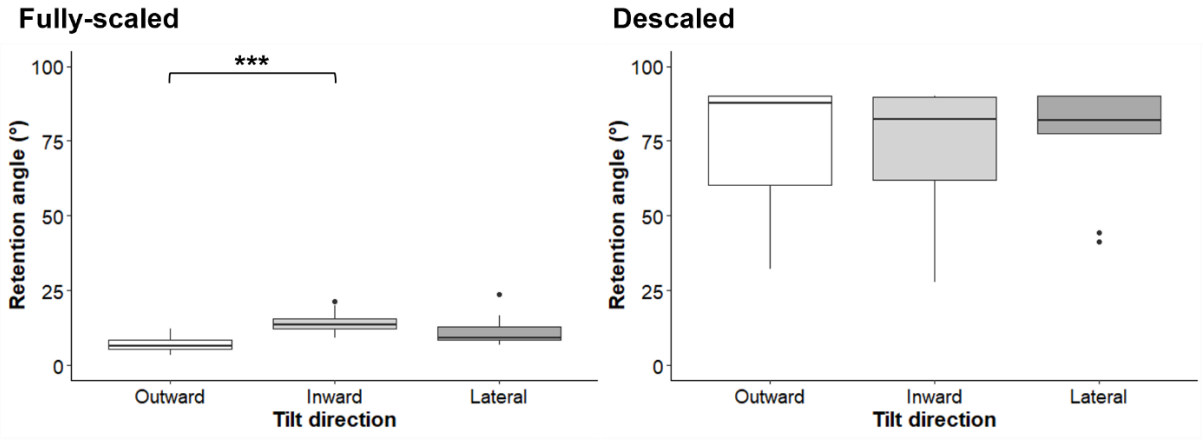

Figure 11. The directionality of drop shedding from the discal region of *Attacus* wings (N =10). Retention angles (°) were measured from fully-scaled and descaled samples in three directions: outward (toward the apical edge), inward (toward the wing

base), lateral (perpendicular to venation). A significant effect was found between outward and inward retention angles measured from fully-scaled samples, as represented by '***'.

Tilt direction had a significant effect on RAs measured from fully-scaled samples (Kruskal-Wallis: chi-squared $_{(1,2)}$ = 12.11, p-value = 0.0005; Figure 11, *Left panel*), but not descaled samples (Chi-squared $_{(1,2)}$ = 0.19, p-value = 0.9102; Figure 11, *Right panel*).

Pairwise comparisons found outward RAs to be significantly higher than inward RAs (Dunn test: z = 3.79, p-value = 0.0005) by 7.4°. No significant effects were found between outward and lateral RAs (z = -2.18, p-value = 0.0583); or inward and lateral RAs (z = 1.61, p-value = 0.1080).

3.3 H3. The discal scale-layer produces less damaging impact dynamics of colliding drops.

Figure 12, illustrates the shattering of drops upon impact with the discal region under two treatments: fully-scaled and descaled.

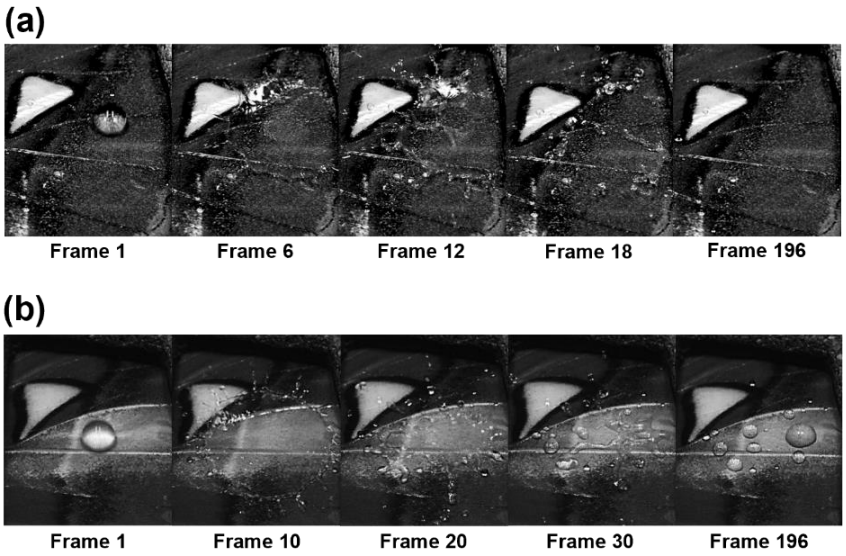

Figure 12. Photographs of drop shatter during impact with the discal region of *Attacus* wings (N=10). (a) Shatter during impact with the intact discal scale-layer. (b) Shattering during impact with the descaled discal membrane.

During impacts with the scale-layer, drops underwent radial spreading from the site of impact, forming a liquid lamella (Figure 12a; *Frame 6*). During this stage, the advancing contact line

became unstable, leading to the formation of 'finger-like' projections. Once a maximum diameter was reached, smaller droplets detached from the apex of 'fingers' and were shed outwardly. Additionally, the liquid lamella was ruptured by the formation of nucleating holes (Figure 12a; *Frame 12*). Nucleating holes then coalesced, causing shattering of the lamella into smaller satellite droplets, which were ejected outwardly (Figure 12*a; Frame 18*). The observed drop shatter resulted in minimal residual water remaining on the discal surface after impact (Figure 12a; *Frame 196*).

During impacts with the descaled membrane, drops underwent radial spreading, forming a liquid lamella which exhibits 'fingering' (Figure 12b, *Frame 10*). After reaching maximum diameter, the liquid lamella receded, and nucleating holes were formed. Additionally, smaller droplets detached from the apex of fingers and were shed outwardly (Figure 12b, *Frame 20*). Shattering of the liquid lamella occurred when the receding edge coalesced with nucleating holes (Figure 12b, *Frame 30*). Satellite droplets remained pinned to the descaled membrane resulting in a large proportion of residual water on the discal surface after impact (Figure 12b, *Frame 196*).

Table 3, presents the recorded frequencies of impact metrics observed during drop impacts with the discal scale-layer under two conditions: fully-scaled and descaled

Table 3. The frequency of impact metrics (nucleation, residual drop and surface wetting) observed during impacts with the discal region of *Attacus* wings (N=10) under two treatments: fully-scaled and descaled. Scale removal had significant effects on the frequency of nucleation and residual drops ($p < 0.001$).

	Frequency of impact metric (%)		
Treatment	Nucleation	Residual drop	Surface wetting
Fully-scaled	100	30	0
Descaled	60	100	0
p-value	p<0.001***	p<0.001***	p>0.05

After scale removal, the frequency of nucleation significantly decreased by 40% (McNemar test: McNemar's chi-squared = 38.03, p-value = $6.9840e^{-10}$), whilst residual drop frequency significantly increased by 70% (McNemar's chi-squared = 68.01, p-value = $2.2000e^{-16}$). Scale removal had no effect on the frequency of surface wetting.

3.4 H4: The mechanical impact of drops damages the scale layer of Attacus wings.

3.4.1 Structural scale damage

Figure 13, illustrates structural scale damage observed in the discal region after 150 repeated drop impacts.

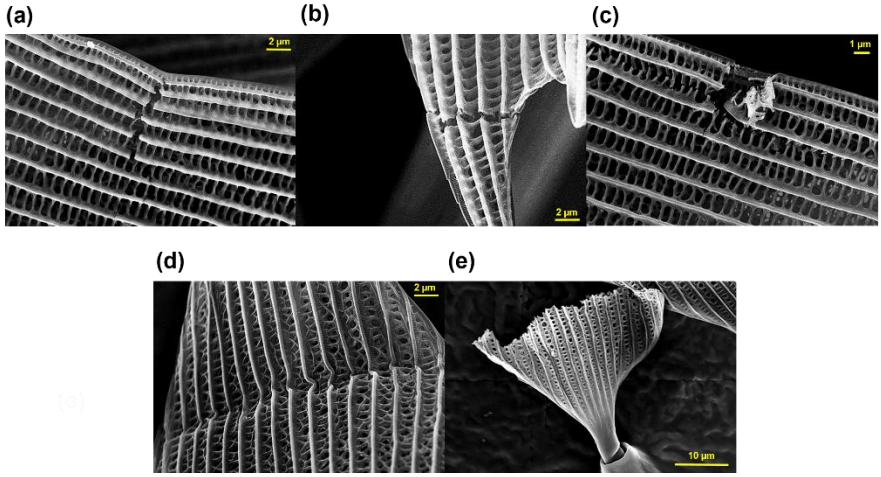

Figure 13. SEM images of structural damage to the discal scales of *Attacus* wings after 150 drop impacts. (a, b) Lateral fractures of the upper lamina. (c) 'Tearing' of the upper lamina away from the lower lamina. (d) Crumpling of scales via lateral 'creasing' of the upper and lower lamina. (e) Complete lateral breakage resulting in a loss of surface area.

Structural damage was categorised into four distinct types: (i) lateral fracturing of the upper lamina (Figure 13a & b); (ii) 'tearing' of the upper lamina away from the lower lamina (Figure 13c); (iii) crumpling of scales via lateral 'creasing' of the upper and lower laminae (Figure 13d); and (iv) complete lateral breakage, leading to loss of scale surface area (Figure 13e).

3.4.2 Scale-layer disorganisation

Figure 14a, illustrates the circular distribution of scale orientations, extracted from images taken of the discal scale-layer under two conditions: intact and damaged.

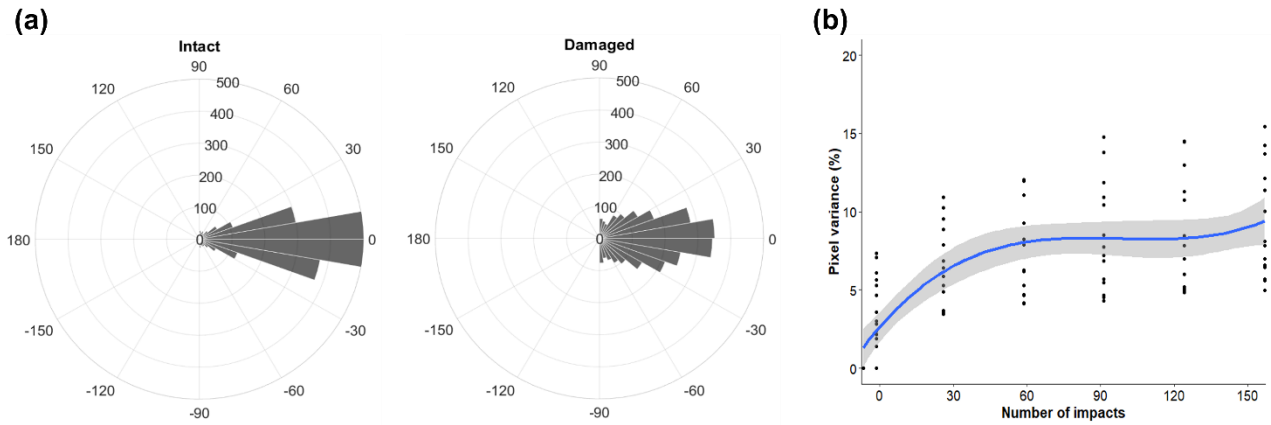

Figure 14. Accumulation of damage within the discal region of *Attacus* wings. (a) The circular distribution of scale orientations (°) extracted from images taken of the discal scale-layer of *Attacus* wings under two treatments: intact and damaged. The effect of repeated drop impact was non-significant ($p > 0.05$). (b) The accumulation of pixel variance (%) observed between images taken of the discal region of *Attacus* wings at regular intervals of 30 impacts. The line-graph demonstrates the fitted polynomial regression model ($h=3$), represented by the blue line) and standard error (represented by the light grey shaded area). The effect of impact number on pixel variance was significant ($p < 0.001$).

Exposure to 150 repeated impacts had a non-significant effect on the circular distribution of scale orientations (Watson's two-sample test: $F_{(1, 5318)} = 2.08$, p-value = 0.1494).

3.4.3 *Scale-layer damage*

Figure 14b, illustrates the accumulation of pixel variance (%) across images of the discal scale-layer in response to increasing impact number (0, 30, 60, 90, 120, 150). A non-linear positive correlation was seen, in which the greatest increase in pixel variance was observed between 0 – 30 impacts, after which the variance plateaued. The total pixel variance accumulated within the discal region over 150 impacts was 9.5 ± 3.58% (mean ± standard deviation). An ANOVA conducted on the fitted regression model found the effect of increasing impact number significant ($F_{(3,94)} = 32.99$, p-value = $1.1790e^{-14}$).

3.4.4 Effect of damage on drop shatter

Figure , illustrates the shattering of drops upon impact with the discal scale-layer after the accumulation of damage.

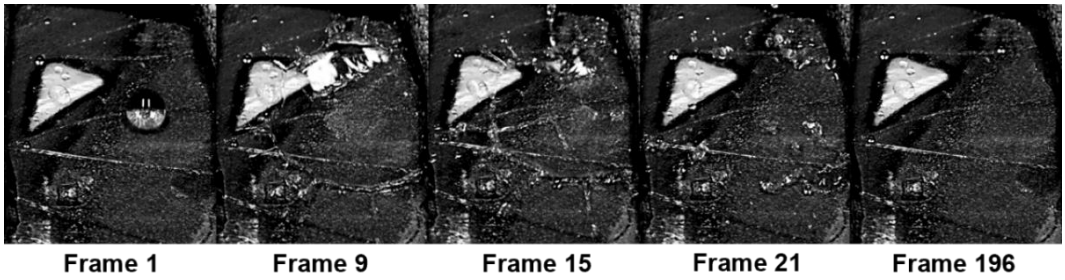

Figure 15. Photograph of drop shatter during impact with the discal region of *Attacus* wings (N=10) after the accumulation of damage.

During impact, drops underwent radial spreading, forming a liquid lamella which exhibited fingering (Figure ; *Frame 9*). Once a maximum diameter was reached, smaller droplets detached from the apex of fingers and were shed outwardly. Additionally, the liquid lamella was ruptured by the formation of nucleating holes (Figure ; *Frame 15*). Finally, coalescence of nucleating holes caused the lamella to shatter into smaller satellite droplets, which were ejected outwardly (Figure *; Frame 21*). The observed drop shatter resulted in minimal residual water remaining on the discal surface after impact (Figure ; *Frame 196*).

Table 4, presents the recorded frequencies of impacts metrics observed during drop impacts with the discal scale-layer under two conditions: intact and damaged.

Table 4. The frequency of impact metrics (nucleation, residual drop and surface wetting) observed during impacts with the discal region of Attacus wings (N=10) under two conditions: intact and damaged. Damage had significant effects on the frequency of all impact metrics ($p < 0.05$).

	Frequency of impact metric (%)		
Wing condition	Nucleation	Residual drop	Surface wetting
Intact	100	30	0
Damaged	80	50	10
p-value	p<0.001***	p<0.001***	p<0.05

During impacts with the damaged scale-layer, the frequency of nucleation significantly decreased by 20% (McNemar's chi-squared = 34.81, p-value = $3.6350e^{-09}$), whilst the frequency of residual drops (McNemar's chi-squared = 18.05, p-value = $2.1520e^{-05}$) and surface wetting (McNemar's chi-squared = 8.1, p-value = 0.0440) significantly increased, by 10% and 20% respectively, in comparison to impacts with intact samples.

3.5 H5. The wettability of Attacus atlas wings varies regionally

3.5.1 Classification of apical and basal scales

Figure illustrates the tiling patterns and surface structure of scales within the apical and basal regions of *Attacus* wings.

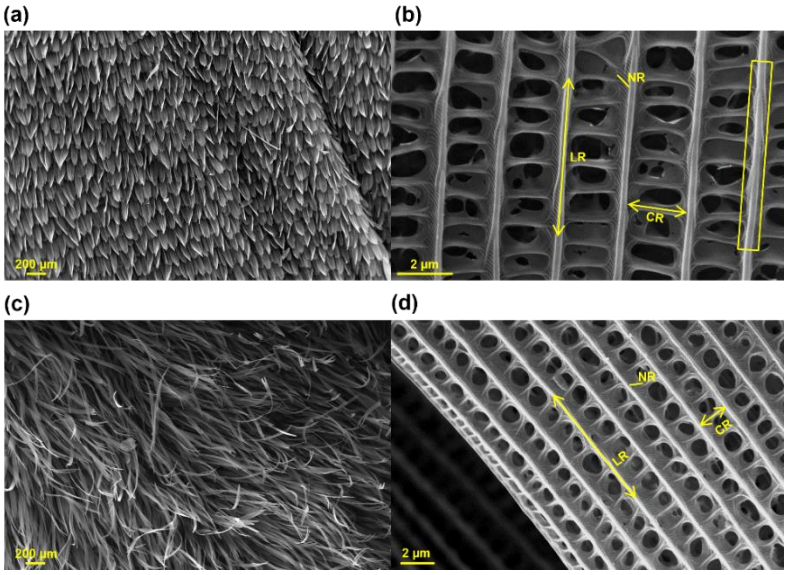

Figure 16. SEM images taken of the apical and basal regions of *Attacus* wings. (a) The 'shingle-like' organisation of the apical scale-layer, taken at 80x magnification. (b) The hierarchical surface structure of apical scales taken at 20'000x magnification, comprising longitudinal ridges (LR), horizontal crossribs (CR) and nanoscale ridges (NR). Yellow box highlights 'sawtooth' patterning of LRs formed by overlapping cuticular lamellae. (c) The dense 'fur-like' organisation of the basal scale-layer taken at 80x magnification. (d). The hierarchical surface structure of basal scales taken at 12'000x magnification, comprising longitudinal ridges (LR), horizontal crossribs (CR) and nanoscale ridges (NR).

.

Apical scales were paddle-like, whilst basal scales were ribbon-like. Both scale-types were organised into lateral rows across the wing surface, with their longitudinal axis oriented in an outward direction. In both regions, neighbouring scales exhibited strong lateral and longitudinal overlapping, with apical scales forming a closed-layer with an outward stepwise hierarchy (Figurea), and basal scales forming a dense 'fur-like' layer (Figurec).

The surface of both apical and basal scales demonstrated HR (Figureb & d). At the microscale, LRs formed microgrooves (mean width = 2.03 µm and 1.62 µm respectively), which were interconnected by CRs forming a mesh-like pattern. Within microgrooves, NRs were observed. LRs on apical scales demonstrated a noticeable 'sawtooth' pattern, formed by overlapping

cuticle lamellae, orientated towards the tips of scales. No sawtooth pattern was observed on the LRs of basal scales.

3.5.2 Surface wettability

Table 5 presents the CAs of sessile drops measured from the apical and basal regions under two treatments: fully-scaled and descaled.

Table 5. The contact angles (°) of sessile drops measured from the apical and basal regions of *Attacus* wings (N= 10) under two treatments: fully-scaled and descaled. The effect of scale removal was significant (p <0.001).

	Contact angle [°] (mean ± standard deviation)		p-value
Region	Fully-scaled	Descaled	
Apical	145.3 ± 3.84	100.0 ± 4.48	p<0.001***
Basal	141.5 ± 4.30	98.6 ± 3.19	p<0.001***

Scale removal had a significant effect on CAs recorded from both apical ($t_{(1,9)} = -30.29$, p-value = $2.2810e^{-10}$) and basal samples ($t_{(1,9)} = -19.52$, p-value = $1.1240e^{-08}$), with descaled CAs being 45.3° and 42.6° lower respectively.

Table 6 presents the RAs measured by tilting fully-scaled, and descaled apical and basal samples in three directions: outward, inward and lateral.

Table 6. The drop retention angles (°) measured from the apical and basal regions of *Attacus* wings (N=10), when tilting samples in three directions: outward (towards the apical edge), inward (towards the wing base), lateral (perpendicular to venation). Retention angles were recorded under two treatments: fully-scaled and descaled. The effect of scale removal was significant in all directions ($p < 0.01$).

Region	Retention angle [°] (Mean ± standard deviation)		
	Outward	Inward	Lateral
Apical			
Fully-scaled	7.5 ± 2.57	16.3 ± 3.41	10.8 ± 3.34
Descaled	83.7 ± 8.20	87.5 ± 1.29	84.7 ± 5.17
p-value	p<0.01**	p<0.01**	p<0.01**
Basal			
Fully-scaled	14.3 ± 9.48	23.3 ± 6.98	16.5 ± 2.95
Descaled	70.8 ± 10.73	64.2 ± 11.11	77.4 ± 9.24
p-value	p<0.01**	p<0.01**	p<0.01**

For all tilt directions, scale removal had a significant effect on RAs recorded from apical samples (outward: V = 0, p-value = 0.0020; inward: V = 0, p-value = 0.0020; lateral: V = 0, p-value = 0.0059), in which outward, inward and lateral descaled RAs were 76.2°, 71.2° and 73.9° higher respectively; and basal samples (outward: V = 0, p-value = 0.0020; inward: V = 0, p-value = 0.0059; lateral: V = 0, p-value = 0.0059), in which outward, inward and lateral descaled RAs were 66.5°, 58.6° and 64.8° higher respectively compared to fully-scaled RAs.

Figure 17, illustrates regional effects on CAs and RAs measured from apical, discal and basal samples.

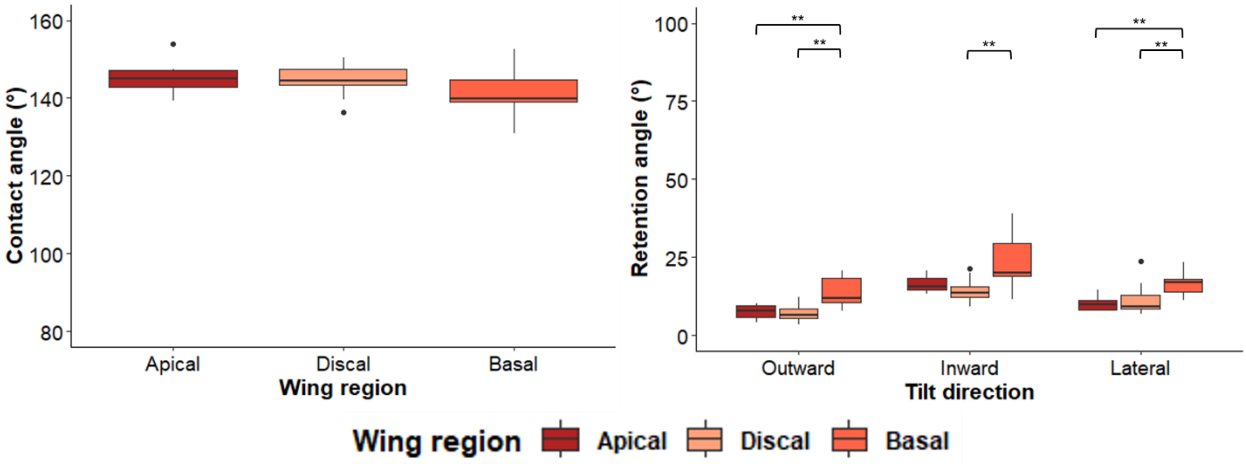

Figure 17. The effect of region on the surface wettability of *Attacus* wings (N=10). (a) Contact angles (°) of sessile drops measured from fully-scaled apical, discal and basal samples. (b) Retention angles (°) measured from fully-scaled apical, discal and basal samples tilted in three directions: outward (towards the apical edge); inward (towards the wing base) and lateral (perpendicular to venation). Region had a significant effect on retention angles ($p < 0.01$), as represented by '**'. No significant effects were found between regional contact angles ($p > 0.05$).

Region had a non-significant effect on CAs ($F_{(2,27)} = 1.65$, p-value = 0.2116), but a significant effect on RAs (chi-squared = 55.33, df = 8, p-value = $3.8010e^{-09}$) for all tilt directions.

Outwardly, pairwise comparisons found significant effects when comparing basal RAs with apical (z = -2.99, p-value = 0.0056) and discal RAs (z = -3.38, p-value = 0.0021), with basal RAs being 6.8° and 7.3° higher respectively. No significant effects were found between apical and discal RAs (z = 0.39, p-value = 0.6933). Inwardly, basal RAs were found significantly higher than discal RAs (z = -3.01, p-value = 0.0078), by 8.9°. No significant effects were found when comparing apical RAs with basal (z = -1.79, p-value = 0.1464), or discal RAs (z = 1.22, p-value = 0.2225). Laterally, significant effects were found when comparing basal RAs with apical (z = -3.14, p-value = 0.0050) and discal RAs (z = -2.74, p-value = 0.0124), with basal RAs being 5.7° and 4.8° higher respectively. No significant effects were found between apical and discal RAs (z = -0.41, p-value = 0.6838).

Figure 18, illustrates the cupping of drops by apical, discal and basal scales.

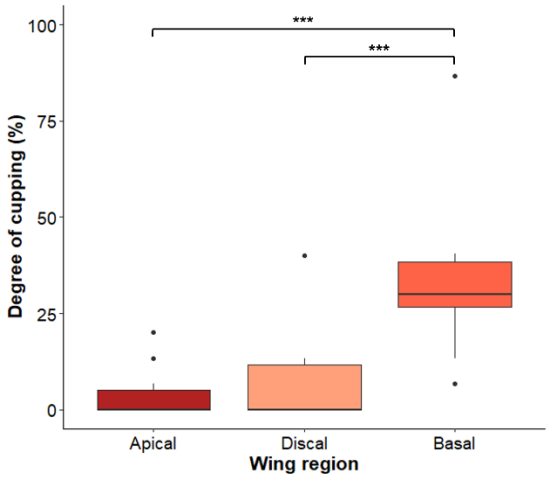

Figure 18. The cupping of sessile drops by scales within the apical, discal and basal scales of *Attacus* wings (N= 10). Regional effects were significant (p <0.001), as represented by '***'.

Region had a significant effect on the degree of cupping observed across *Attacus* wings (Chi-squared $_{(1,2)}$ = 15.52, p-value = 0.0004). Pairwise comparisons found that basal cupping was significantly higher than apical (z = -3.81, p-value = 0.0012) and discal cupping (z = -3.33, p-value = 0.0069), by 65.7% and 62.4% respectively. No significant effect was found between discal and apical cupping (z = -0.48, p-value = 1.0000).

3.5.3 Directional drop shedding

Figure 19, illustrates the directionality of drop shedding from the apical and basal regions under two treatments: fully-scaled and descaled.

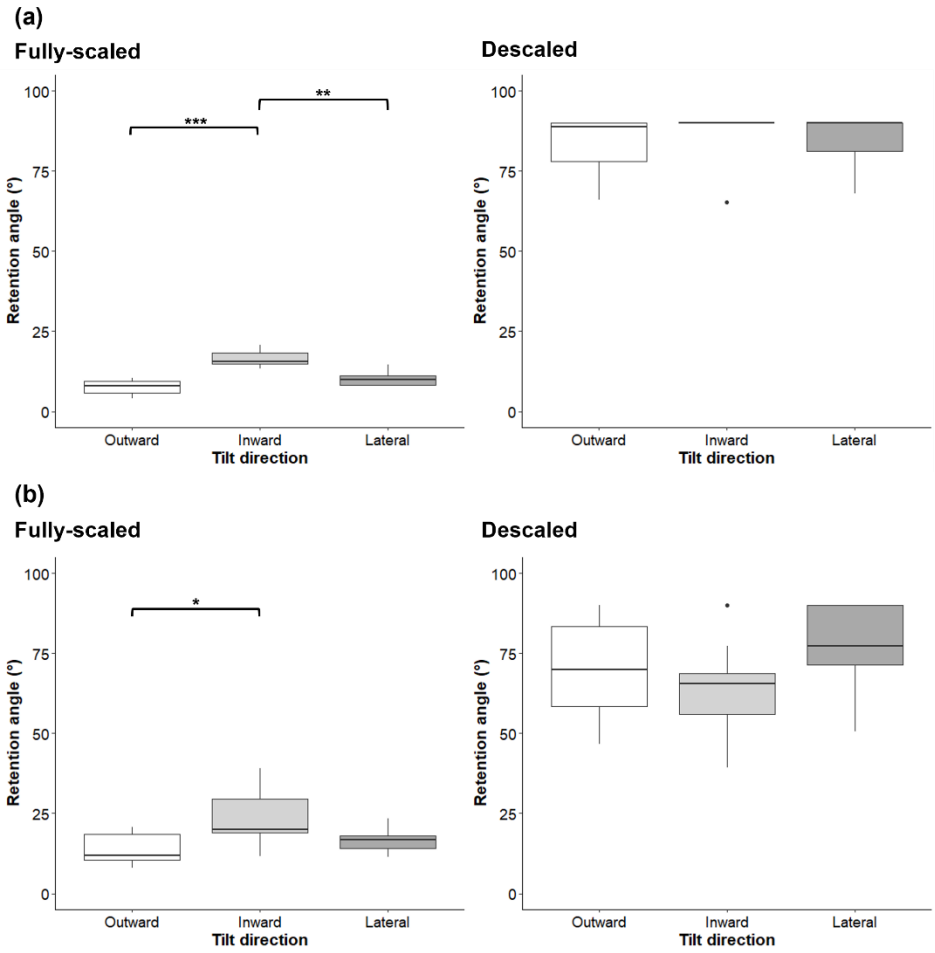

Figure 19. The directionality of drop shedding from: (a) the apical region and (b) the basal region of *Attacus* wings (N=10). Retention angles (°) were measured from fully-scaled and descaled samples in three directions: outward (toward the apical edge), inward (toward the wing base), lateral (perpendicular to venation). The effects of tilt direction were significant for fully-scaled samples ($p < 0.05$). Significant effects are represented by '*', very significant effects are represented by '**', and highly significant effects are represented by '***'.

For both regions, tilt direction had a significant effect on RAs recorded from fully-scaled samples (apical: chi-squared $_{(1.2)} = 19.92$, p-value = $4.7220e^{-05}$; basal: chi-squared $_{(1,2)} = 8.4953$, p-value = 0.0143) but not descaled samples (apical: chi-squared $_{(1,2)} = 2.70$, p-value = 0.2592; basal: chi-squared $_{(1,2)} = 4.25$, p-value = 0.1195).

Pairwise comparisons found that inward RAs were significantly higher than outward RAs for both apical (z = -4.40, p-value = $3.2453e^{-05}$) and basal samples (z = -2.88, p-value = 0.0118), by 8.8° and 9.0° respectively. For apical samples, inward RAs were significantly higher than lateral RAs (z = 2.85, p-value = 0.0088), by 5.5°. This effect was non-significant in basal samples (z = 1.80, p-value = 0.1423). For both regions, no significant effects were found between outward and lateral RAs (apical: z = -2.88, p-value = 0.1208; basal: z = -1.08, p-value = 0.2801).

3.5.4 Drop shatter upon the basal scale-layer

Figure 20, illustrates the shattering of drops upon impact with the fully-scaled basal region under two conditions: intact and damaged.

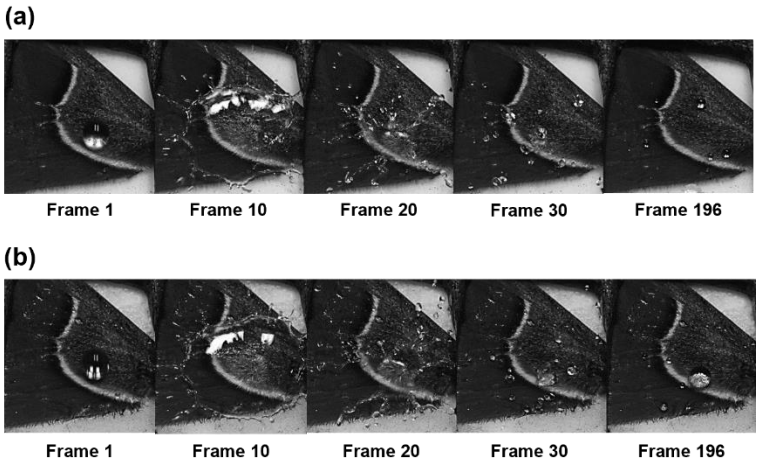

Figure 20. Photographs of drop shatter during impact with the basal region of *Attacus* wings (N=10). (a) Shattering during impact with the intact basal scale-layer. (b) Shattering during impact with the basal scale-layer after the accumulation of damage.

During impact with the intact basal scale-layer, drops underwent radial spreading, forming a liquid lamella which exhibited fingering (Figure 20a, *Frame 10*). After reaching maximum diameter, the liquid lamella receded, and nucleating holes were formed. During this stage, smaller droplets detached from the apex of fingers and were shed outwardly (Figure 20a, *Frame 20*). Shattering of the liquid lamella into satellite droplets occurred when the receding lamella edge coalesced with nucleating holes (Figure 20a, *Frame 30*). The observed drop shatter resulted in minimal residual water remaining on the basal surface after impact (Figure 20a, *Frame 196*).

Table 7, presents the recorded frequencies of impact metrics observed during drop impacts with the basal scale-layer under two conditions: intact and damaged.

Table 7. The frequency of impact metrics (nucleation, residual drop and surface wetting) observed during impacts with the basal region of *Attacus* wings (N=10) under two conditions: intact and damaged. Damage accumulation had significant effect on the frequency of nucleation and residual drops (p <0.001).

	Frequency of impact metric (%)		
Wing condition	Nucleation	Residual drop	Surface wetting
Intact	60	20	0
Damaged	40	70	0
p-value	p<0.001***	p<0.001***	p>0.05

During basal impacts, the frequency of nucleation was significantly higher compared to discal impacts (Chi-squared test of independence: X-squared $_{(1,1)}$ = 10, p-value = 4.0920e^{-10}), by 40%. Region had a non-significant effect on the observed frequency of residual drops during discal and basal impacts drops (X-squared = 2, df = 1, p-value = 0.1573). Surface wetting was absent during impacts with both the discal and basal regions (Table 3; Table 7).

3.5.5 *Damage accumulation within the basal scale-layer*

Figure 21a, illustrates the circular distribution of scale orientations, extracted from images taken of the basal scale-layer under two conditions: intact and damaged.

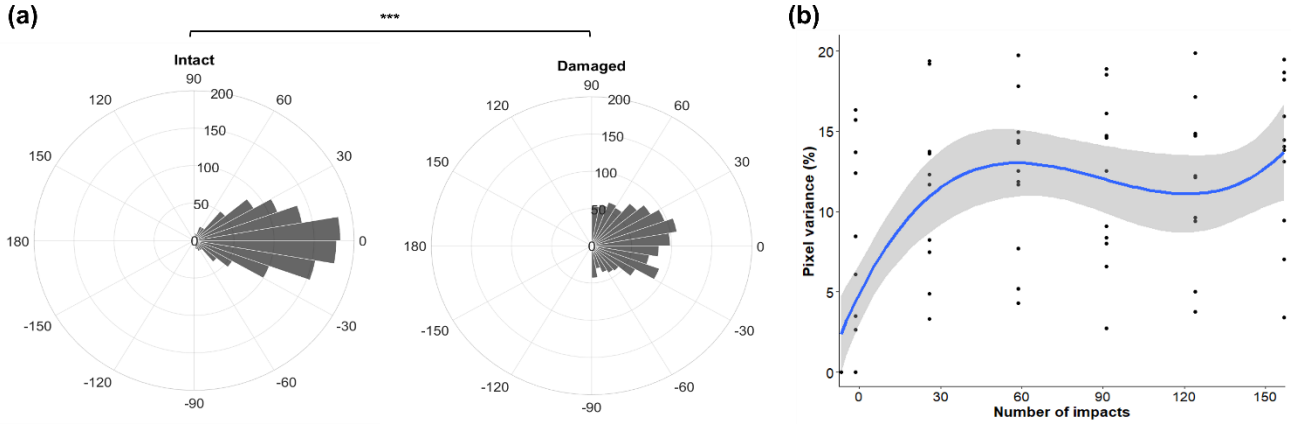

Figure 21. Accumulation of damage within the basal region of *Attacus* wings. (a) The circular distribution of scale orientations (º) extracted from images taken of the basal scale-layer (N = 11) under two treatments: intact and damaged. The effect of repeated drop impact on basal scale orientations was highly significant (p <0.001), as represented by '***'. (b) The accumulation of pixel variance (%) observed between images taken of the basal region of *Attacus* wings at regular intervals of 30 impacts. The graph demonstrates the fitted polynomial regression model (*h* = 3, represented by the blue line) and standard error (represented by the light grey shaded area). The effect of impact number on pixel variance was highly significant (p <0.001).

Exposure to 150 repeated impacts resulted in the scale orientations extracted from damaged images to be significantly wider than those extracted from intact image ($F_{(1, 2398)} = 15.15$, p-value = $1.0200e^{-4}$).

Figure 20b, illustrates the accumulation of pixel variance (%) across images of the discal scale-layer in response to increasing impact number (0, 30, 60, 90, 120, 150). A non-linear positive correlation was seen, in which the greatest increase in pixel variance was observed between 0 – 30 impacts, after which the variance plateaued. The total pixel variance accumulated within the basal region over 150 impacts was 12.7 ± 4.80%. (mean ± standard deviation). An ANOVA conducted on the fitted regression model found the effect of increasing impact number significant ($F_{(3,73)} = 16.54$, p-value = $2.673e^{-08}$).

Region had a significant effect on the total pixel variance (W = 116, p-value = 0.0333), with the accumulation of pixel variance observed in the basal region being 3.2% lower compared to the discal region.

3.5.6 Effect of damage on drop shatter

During impact, drops underwent radial spreading, forming a liquid lamella which exhibited fingering (Figure 20b; *Frame 10*). After reaching a maximum diameter, the liquid lamella receded, and nucleating holes were formed. During this stage, smaller droplets detached from the apex of fingers and were shed outwardly (Figure 20b; *Frame 20*). Shattering of the liquid lamella into satellite droplets occurred when the receding edge coalesced with nucleating holes (Figure 20b; *Frame 30*). The observed drop shatter resulted in a large proportion of residual water remaining on the basal surface after impact (Figure 20b, *Frame 196*).

During impact with the damaged scale-layer, the frequency of nucleation significantly decreased by 20% (McNemar's chi-squared = 18.05, df = 1, p-value = $2.1520e^{-05}$), whilst residual drop frequency significantly increased by 50% (McNemar's chi-squared = 48.02, df = 1, p-value = $4.2190e^{-12}$). Damage accumulation had no effect on the frequency of surface wetting (Table 7).

3.6 H6. The drop interactions of transparent wing regions differ from fully scaled regions

3.6.1 *Classification of TW and M. confusa scales*

Figure illustrate the tiling patterns and surface structure of scales within the TW region of *Attacus* wings, and the discal region of *M. confusa* wings.

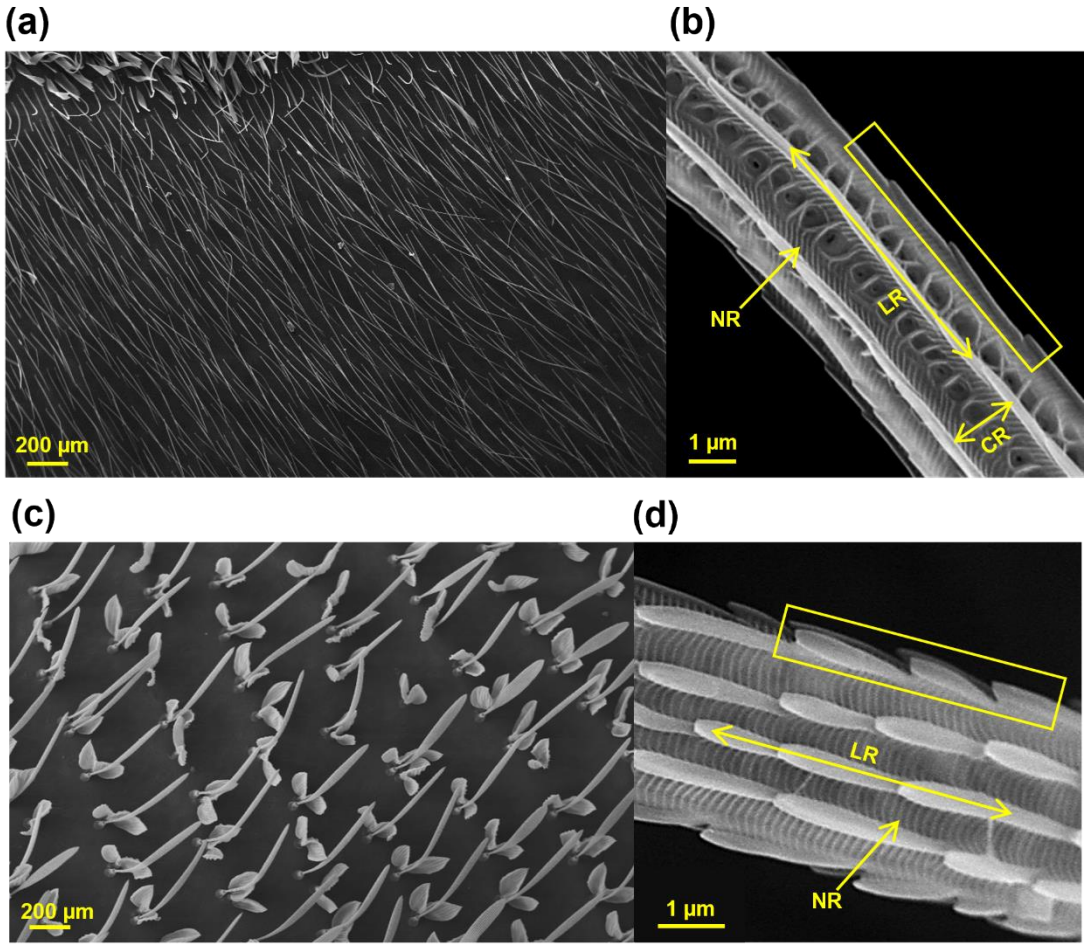

Figure 22. SEM images of taken of the transparent window (TW) of *Attacus* wings, and the discal region of *M. confusa* wings (a) The 'fur-like' organisation of the TW scale-layer taken at 80x magnification. (b) The hierarchical structure of TW scales taken at 12'000x magnification, comprising longitudinal ridges (LR), horizontal crossribs (CR) and nanoscale ridges (NR). Yellow box highlights distinct 'sawtooth' patterning of LRs formed by overlapping cuticular lamellae. (c) The organisation of the discal scale-layer taken at 500x magnification. (d) The hierarchical structure of discal scales taken at 20'000x magnification, comprising longitudinal ridges (LR), horizontal crossribs (CR) and nanoscale ridges (NR). Yellow box highlights distinct 'sawtooth' patterning of LRs formed by overlapping cuticular lamellae.

TW scales were hair-like, whilst *M. confusa* scales were unique, comprising distinct elongated ovoid cover scales coupled with 'bowtie-like' base scales. Both scale-types were organised into lateral rows across the wing surface, with their longitudinal axis oriented in an outward direction. In both regions, neighbouring scales exhibited weak lateral and longitudinal overlapping, with

TW scales forming a shear ‘fur-like’ layer (Figure 22a), and *M. confusa* scales forming an open-layer with high proportions of the membrane visible (Figure 22c).

The surface of both TW and *M. confusa* scales demonstrated HR (Figure 22b and d). At the microscale, LRs formed microgrooves (mean width = 1.14 µm and 0.35 µm respectively), in which NRs were observed. On TW scales, LRs were interconnected by CR forming a mesh-like pattern. Periodic windows formed by CRs were absent in *M. confusa* scales. The LRs on both TW and *M. confusa* scales demonstrated an extremely well-defined ‘sawtooth’ pattern, formed by overlapping cuticle lamellae, orientated towards the tips of scales.

3.6.2 Surface wettability

Table 8 presents the CAs of sessile drops measured from the TW and *M. confusa* regions under two treatments: fully-scaled and descaled.

Table 8. The contact angles (°) of sessile drops measured from the transparent window of *Attacus* wings (N=10), and the discal region of *M. confusa* wings (N=7) under two treatments: fully-scaled and descaled. The effect of scale removal was significant (p <0.001).

	Contact angle [°] (mean ± standard deviation)		**p-value**
Region	Fully-scaled	Descaled	
TW	141.6 ± 1.66	88.8 ± 3.85	p<0.001***
M. confusa	148.6 ± 6.60	110.8 ± 7.15	p<0.001***

Scale removal had a significant effect on CAs recorded from both TW ($t_{(1,9)}$ = 16.67, p-value = 4.5040e-08) and *M. confusa* samples ($t_{(1,6)}$ = -8.61, p-value = 0.0001), with descaled CAs being 52.8° and 37.8° lower respectively.

Table 9 presents the RAs measured by tilting fully-scaled, and descaled TW and *M. confusa* samples in three directions: outward, inward and lateral.

Table 9. The drop retention angles (°) measured from the transparent window (TW) of *Attacus* wings (N=10), and the discal region of *M. confusa* wings (N=6) when tilting samples in three directions: outward (towards the apical edge), inward (towards the wing base) and lateral (perpendicular to venation).Retention angles were recorded under two treatments: fully-scaled and descaled. The effect of scale removal was significant in all directions ($p < 0.01$).

Region	Retention angle [°] (mean ± standard deviation)		
TW	Outward	Inward	Lateral
Fully-scaled	7.4 ± 2.85	13.6 ± 5.18	17. 6 ± 5.86
Descaled	50.1 ± 7.57	53.5 ± 4.86	50.4 ± 13.02
p-value	p<0.01**	p<0.01**	p<0.01**
M. confusa			
Fully-scaled	2.1 ± 2.91	5.0 ± 3.19	7.9 ± 5.81
Descaled	80.3 ± 5.45	75.4 ± 8.06	90.0 ± 0.00
p-value	p<0.01**	p<0.01**	p<0.01**

For all tilt directions, scale removal had a significant effect on RAs recorded from TW samples (outward: V = 0, p-value = 0.0020; inward: V = 0, p-value = 0.0020; lateral: V = 0, p-value = 0.0020), in which outward, inward and lateral descaled RAs were 42.7°, 39.9° and 32.8° higher respectively; and *M. confusa* samples (outward: V= 0, p-value = 0.0156, inward: V= 0, p-value = 0.0223; lateral: V= 0, p-value = 0.0223), in which outward, inward and lateral descaled RAs were 78.2°, 70.4° and 82.1° higher respectively compared to fully-scaled RAs.

Figure 23 illustrates the effect of transparency on CAs and RAs measured across *Attacus* and *M. confusa* wings.

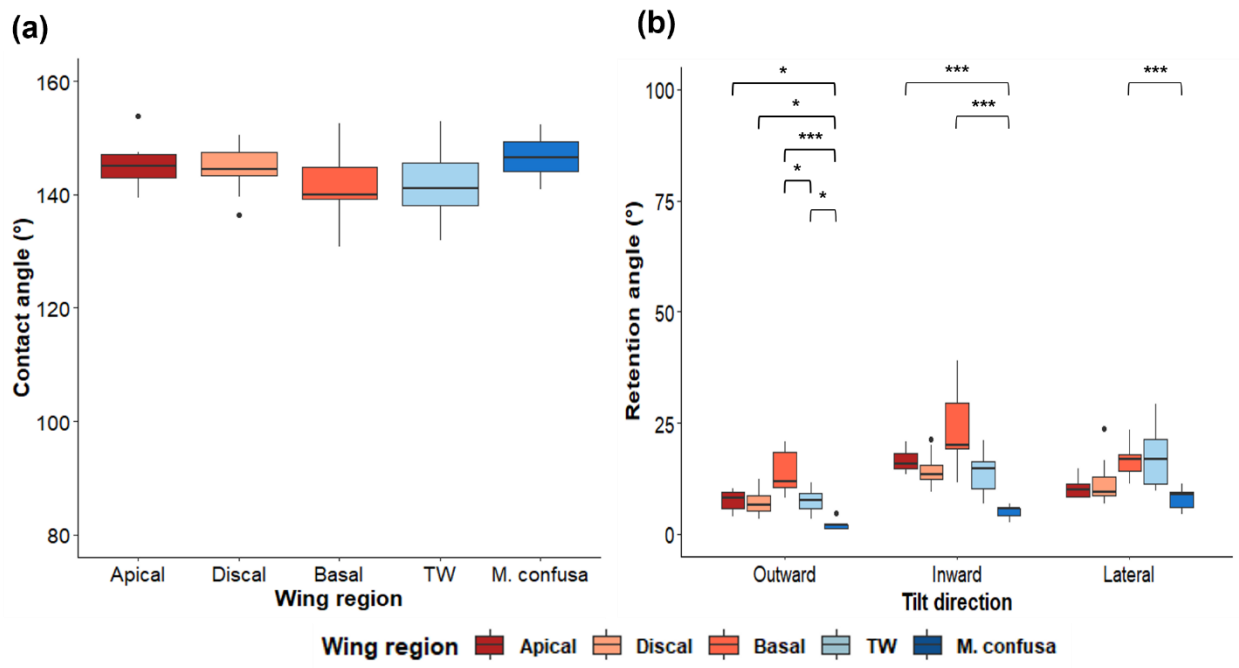

Figure 23. The effect of transparency on surface wettability across *Attacus* (N=10) and *M. confusa* wings (N=6). (a) Contact angles (°) of sessile drops measured from fully-scaled apical, discal, basal and TW *Attacus* samples, and discal *M. confusa* samples. The effect of transparency was non-significant ($p > 0.05$). (b) Retention angles (°) measured from fully-scaled apical, discal, basal and TW *Attacus* samples, and discal *M. confusa* samples tilted in three directions: outward (towards the apical edge), inward (towards the wing base) and lateral (perpendicular to venation). Transparency had a significant effect ($p<0.05$), significant effects are represented by '*', very significant effects are represented by '**', and highly significant effects are represented by '***'.

Transparency had a non-significant effect on CAs (Chi-squared$_{(1,4)}$ = 8.18, p-value = 0.0851; Figure 23a), but a significant effect on RAs (Chi-squared = 98.04$_{(1,14)}$, p-value = 1.1260e^{-14}; Figure 23b) for all tilt directions.

Outwardly, pairwise comparisons found TW RAs significantly lower than basal RAs by 6.9° (z = 2.65, p-value = 0.0479); but not apical (z = 0.07, p-value = 0.9479) or discal RAs (z = -0.30, p-value = 1.0000). Significant effects were found when comparing *M. confusa* RAs with apical (z = 2.84, p-value = 0.0358), discal (z = -2.51, p-value = 0.0483) and basal RAs (z = 5.19, p-value = 2.0939e^{-06}), in which *M. confusa* RAs were 5.4°, 4.9° and 12.2° lower respectively.

Inwardly, no significant effects were found when comparing TW RAs with apical (z = 1.08, p-value = 0.8447), discal (z = 0.03, p-value = 0.9740) or basal RAs (z = 2.57, p-value = 0.0611). Significant effects were found when comparing *M. confusa* RAs with apical (z = 3.61, p-value = 0.0028) and basal RAs (z = 4.96, p-value = 6.8935e^{-06}), in which *M. confusa* RAs were 11.3° and

18.3° lower respectively. No significant effects were found between *M. confusa* and discal RAs (z = -2.66, p-value = $0.0621e^{-02}$).

Laterally, no significant effects were found when comparing TW RAs with apical (z = -2.64, p-value = 0.0573), discal (z = -2.34, p-value = 0.0959), or basal RAs (z = 0.26, p-value = 0.7940). *M. confusa* RAs were significantly lower than discal RAs by 8.6° (z = 3.66, p-value = 0.0025); but not apical (z = 1.02, p-value = 0.9204) or basal RAs (z = -1.30, p-value = 0.7799).

During comparisons between transparent regions, TW RAs were significantly higher than *M. confusa* RAs by 5.3°. and 7.9° when tilted in an outward (z = -2.78, p-value = 0.0376) and lateral direction respectively (z = -3.42, p-value = 0.0056); but not an inward direction (z = -2.63, p-value = 0.0594).

Figure , illustrates the cupping of drops by apical, discal, and basal and TW *Attacus* scales, and discal *M. confusa* scales.

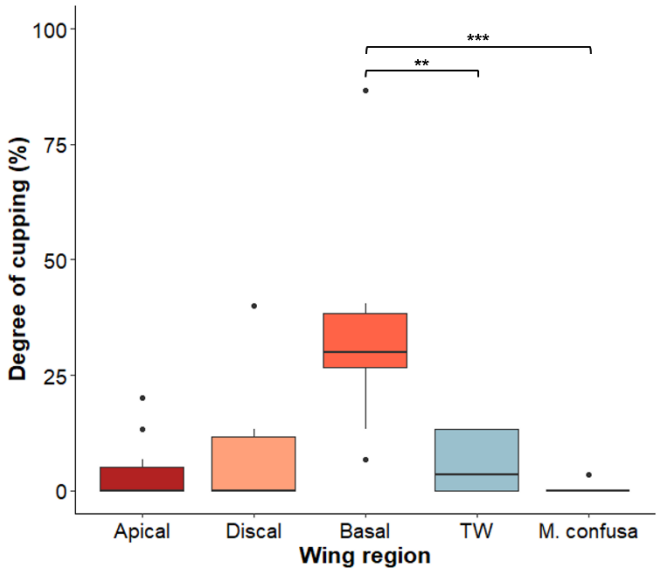

Figure 24. The cupping of sessile drops by scales within apical, discal, basal and TW regions of *Attacus* wings (N=10), and the discal region of *M. confusa* wings (N=6). Regional effects were significant (p <0.01), very significant effects are represented by '**' and highly significant effects are represented by '***'.

Transparency had a significant effect on the degree of cupping observed across *Attacus* and *M. confusa* wings (Chi-squared = $22.93_{(1,4)}$, p-value = 0.0001). Pairwise comparisons found that

basal cupping was significantly higher than TW (z = 3.15, p-value = 0.0113) and *M. confusa* cupping (z = 4.16, p-value = 0.0003), by 27.4% and 32.89% respectively. No significant effects were found when comparing transparent cupping with apical (TW: z = 0.66, p-value = 1.000; *M. confusa*: z = 0.70, p-value = 1.0000) or discal cupping (TW: z = -0.18, p-value = 0.8605; *M. confusa*: z =1.13, p-value = 1.0000). Furthermore, no significant effects were found between TW and *M. confusa* cupping (z = 1.29, p-value = 1.0000).

3.6.3 Directional drop shedding

Figure 25, illustrates the directionality of drop shedding from the TW and *M. confusa* regions under two treatments: fully-scaled and descaled.

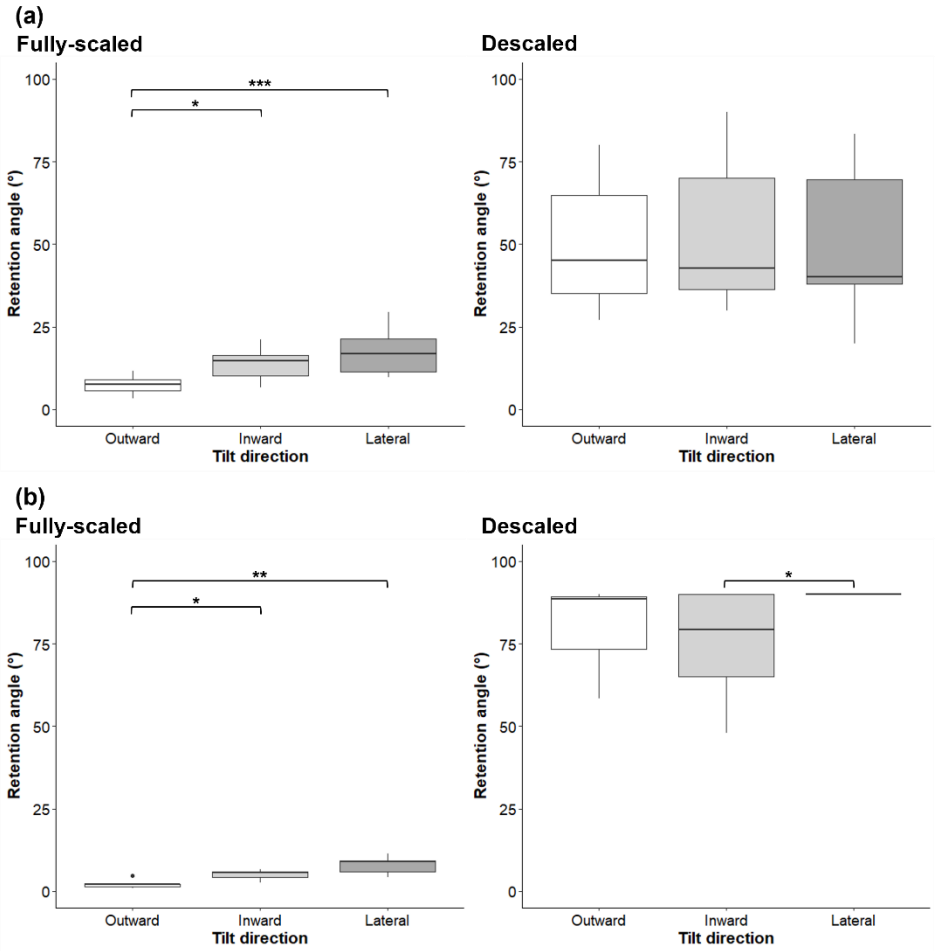

Figure 25. The directionality of drop shedding from: (a) the TW region of *Attacus* wings (N=10), and (b) the discal region of *M. confusa* wings (N=6). Retention angles (°) were measured from fully-scaled and descaled samples in three directions: outward (toward the apical edge), inward (toward the wing base), lateral (perpendicular to venation). The effect of tilt direction was significant (p <0.05). Significant effects are represented by '*', very significant effects are represented by '**', and highly significant effects are represented by '***'.

For both regions, tilt direction had a significant effect on RAs recorded from fully-scaled samples (TW: chi-squared = $14.68_{(1,2)}$, p-value = 0.0007; *M. confusa*: chi-squared = $13.12_{(1,2)}$, p-value = 0.0014) (Figure 25a & b, *Left panels*). For both regions, pairwise comparisons found outward RAs significantly lower than inward RAs (TW: z = -2.64, p-value = 0.0164; *M. confusa*: z = -2.25, p-value = 0.0495) by 6.2° and 2.9° respectively; and lateral RAs (TW: z = -3.72, p-value = 0.0006; *M. confusa*: z = -3.58, p-value = 0.0010) by 10.2° and 5.8° respectively. No significant differences were found between inward and lateral RAs (TW: z = -1.08, p-value = 0.2800; *M. confusa*: z = -1.34, p-value = 0.1807).

Tilt direction had a significant effect on RAs recorded from descaled *M. confusa* samples (Chi-squared = $6.79_{(1,2)}$, p-value = 0.0336) (Figure 25b, *Right panel*)., but not descaled TW samples (Chi-squared = $0.20_{(1,2)}$, p-value = 0.9007) (Figure 25a, *Right panel*). Pairwise comparisons found inward RAs significantly lower than lateral RAs (z = -2.24, p-value = 0.0496) by 14.6°. No significant effects were found when comparing outward RAs with lateral (z = -2.27, p-value = 0.0700) and inward RAs (z = -2.27, p-value = 0.0700).

3.6.4 Drop shatter upon the TW and M. confusa scale-layers

Figure 26, illustrates the shattering of drops upon impact with fully-scaled TW and *M. confusa* regions under two conditions: intact and damaged.

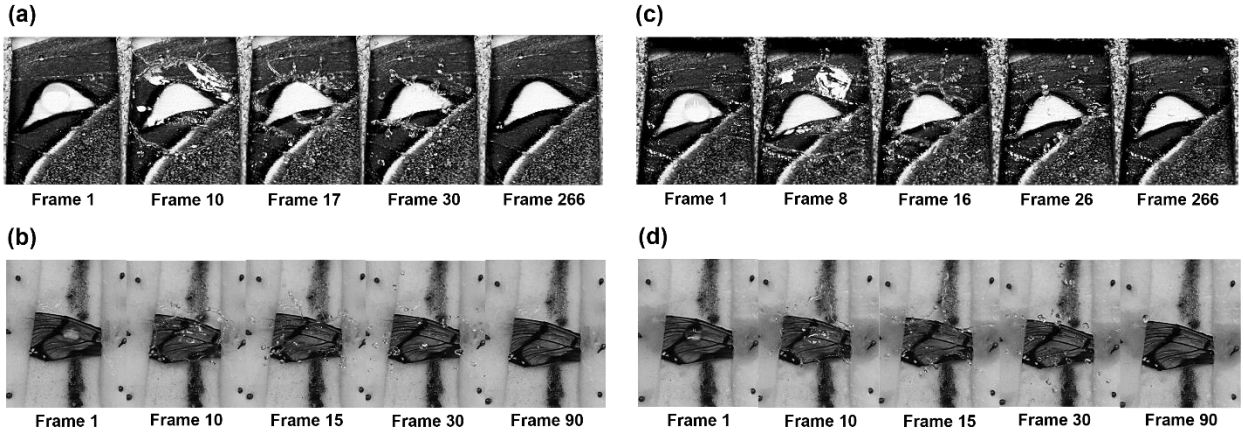

Figure 26. Photographs of drop shatter during impacts with the TW region of *Attacus* wings (N=10), and the discal region of *M. confusa* wings (N=6). (a) Shattering during impacts with the intact TW scale-layer. (b) Shattering during impacts with the intact *M. confusa* scale-layer. (c) Shattering during impacts with the TW scale-layer after the accumulation of damage. (d) Shattering during impacts with the *M. confusa* scale-layer after the accumulation of damage.

During impacts with the intact TW and *M. confusa* scale-layers, drops underwent radial spreading, forming a liquid lamella which exhibited fingering (Figure 26a; *Frame 10*; Figure 26b, *Frame 10*). During TW impacts, the liquid lamella receded after reaching maximum diameter, after which nucleating holes were formed (Figure 26a; *Frame 17*). In contrast, during *M. confusa* impacts, the liquid lamella was ruptured by the formation of nucleating holes at maximum diameter (Figure b; *Frame 15*). In both impacts, smaller droplets detached from the apex of fingers and were shed outwardly during this stage. For TW impacts, shattering of the liquid lamella into satellite droplets occurred when the receding lamella edge coalesced with nucleating holes (Figure 26a; *Frame 30*). For *M. confusa* impacts, shattering occurred via the coalescence of nucleating holes which caused satellite drops to be ejected outwardly (Figure 26b, *Frame 30*). In both cases, the observed shatter resulted in very little residual surface water after impact (Figure 26a; *Frame 266;* Figure 26b, *Frame 90*).

Table 10 presents the recorded frequencies of impact metrics observed during drop impacts with the TW and *M. confusa* scale-layers under two conditions: intact and damaged.

Table 10. The frequency of impact metrics (nucleation, residual drop and surface wetting) observed during impacts with the TW region of *Attacus* wings (N=10), and the discal region of *M. confusa* wings (N=6), under two conditions: intact and damaged. Damage accumulation had a significant effect on the frequencies of all impact metrics ($p<0.001$).

	Frequency of impact metric (%)		
	Nucleation	Residual drop	Surface wetting
TW			
Intact	80	80	10
Damaged	50	90	40
p-value	p<0.001***	p<0.001***	p<0.001***
M. confusa			
Intact	83.3	50	0
Damaged	100	83.3	16.7
p-value	p<0.001***	p<0.001***	p<0.001***

During both TW and *M. confusa* impacts, the frequency of nucleation did not differ significantly from that observed during discal (TW: X-squared = $2.22_{(1,1)}$, p-value = 0.1360; *M. confusa*: X-squared = $1.52_{(1,1)}$, p-value = 0.2174) or basal impacts (TW: X-squared = $2.86_{(1,1)}$, p-value = 0.0910; *M. confusa*: X-squared = $3.79_{(1,1)}$, p-value = 0.0516). Residual drops were observed 50%

and 60% more frequently during TW impacts compared to discal (X-squared = $22.73_{(1,1)}$, p-value = $1.8670e^{-06}$) and basal impacts (X-squared = $36.00_{(1,1)}$, p-value = $1.9730e^{-09}$), an effect which was significant. During *M. confusa* impacts residual drops were observed 20% and 30% more frequently compared to discal (X-squared = $5_{(1,1)}$, p-value = 0.0254) and basal impacts (X-squared = $12.86_{(1,1)}$, p-value = 0.0003), an effect which was significant. Surface wetting occurred 10% more frequently during TW impacts, compared to discal (X-squared = $10_{(1,1)}$, p-value = 0.0016) and basal impacts (X-squared = $10_{(1,1)}$, p-value = 0.0016), an effect which was significant. Surface wetting did not significantly differ across discal, basal and *M. confusa* impacts (Table 3; Table 7; Table 10).

When comparing between transparent regions, the frequency of residual drops and surface wetting observed during TW impacts was 30% higher; and 10% lower respectively than *M. confusa* impacts, an effect which was significant (residual drops: X-squared = $6.92_{(1,1)}$, p-value = 0.0085; surface wetting: X-squared = $10_{(1,1)}$, p-value = 0.0016). No significant effects were found when comparing the frequency of nucleation ($0.80_{(1,1)}$, p-value = 0.7962) (Table 10).

3.6.5 Damage accumulation within the TW scale-layer

Figure, illustrates the accumulation of pixel variance (%) across images of the TW scale-layer in response to increasing impact number (0, 30, 60, 90, 120, 150).

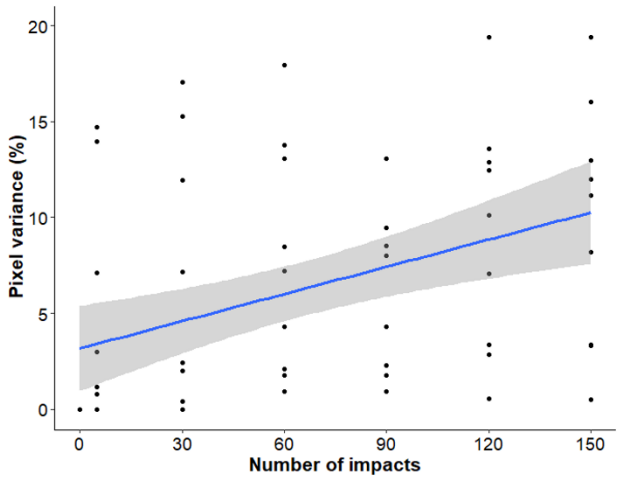

Figure 27. The accumulation of pixel variance (%) observed between images taken of the TW region of *Attacus* wings (N=9) at regular intervals of 30 impacts. The graph demonstrates the fitted polynomial regression model (*h* = 1, represented by the blue line) and standard error (represented by the light grey shaded area). The effect of impact number on pixel variance was highly significant (p<0.001).

A linear positive correlation was seen, in which pixel variance gradually increased over 150 impacts. The total pixel variance within the TW region over 150 impacts was 9.6 ± 6.33%. An ANOVA conducted on the fitted regression model found the effect of increasing impact number significant ($F_{(1,61)} = 12.83$, p-value = 0.0007).

Transparency had a non-significant effect on the total pixel variance (Chi-squared$_{(1,2)} = 4.11$, p-value = 0.1284) accumulated within the TW, discal and basal regions.

3.6.6 Effect of damage on drop shatter

During impacts with both regions, drops underwent radial spreading forming a liquid lamella which exhibited fingering (Figurec; *Frame 8*; (Figured, *Frame 10*). During TW impacts, the liquid lamella receded after reaching maximum diameter, after which nucleating holes were formed (Figurec; *Frame 16*). During *M. confusa* impacts, the liquid lamella was ruptured by the formation of nucleating holes before reaching maximum diameter (Figured, *Frame 15*). In both cases, smaller droplets detached from the apex of fingers and were shed outwardly during this stage. For TW impacts, shattering of the liquid lamella into satellite droplets occurred when the receding lamella edge coalesced with nucleating holes (Figurec; *Frame 26*). For *M. confusa* impacts, shattering occurred via the coalescence of nucleating holes, causing satellite drops to be ejected outwardly (Figured, *Frame 30*). In both cases, the observed shatter resulted in little residual surface water after impact (Figurec; *Frame 266;* Figured, *Frame 90*).

During impacts with the damaged TW scale-layer, the frequency of nucleation significantly decreased by 30% (McNemar's chi-squared$_{(1,1)} = 18.05$, p-value = $2.1520e^{-05}$), whilst the frequency of residual drops and surface wetting significantly increased by 50% and 30% respectively (McNemar's chi-squared$_{(1,1)} = 48.02$, p-value = $4.2190e^{-12}$; McNemar's chi-squared$_{(1,1)} = 28.03$, p-value = $1.192e^{-07}$). During impacts with the damage *M. confusa* scale-layer, damage accumulation resulted in a significant increase in the frequency of nucleation by 16.7% (McNemar's chi-squared$_{(1,1)} = 14.76$, p-value = 0.0001); residual drops by 33.3% (McNemar's chi-squared$_{(1,1)} = 31.33$, p-value = $2.1770e^{-08}$); and surface wetting by 16.7% (McNemar's chi-squared$_{(1,1)} = 14.76$, p-value = 0.0001) (Table 10).

Chapter 4. Discussions

4.1 H1. The discal scale-layer of *Attacus* wings constitutes a superhydrophobic surface.

As the CAs and RAs recorded from the discal scale-layer fell below standard thresholds (CA <150°; RAs >5°) for a surface to be defined as superhydrophobic (Tables 1 and 2) (5,119), this surface cannot be classified as superhydrophobic, meaning that hypotheses 1.1 and 1.2 were not satisfied.

The recorded CAs were very high (CA >140°), suggesting that the discal surface is better classified as strongly hydrophobic (*see section 1.2.1*), and it is likely that drops assume an almost spherical shape when contacting the scale-layer (5,33). Additionally, the recorded RAs were very low (RAs <15°), indicating that drops demonstrated low adhesion with the scale-layer. Consequently, the discal surface of *Attacus* wings can be classified as 'slippery'. Although not directly tested in this study, it may be that low drop retention on *Attacus* wings facilitates self-cleaning (105,116,117).

Like previous studies (48,105,115–117), the strong hydrophobicity observed in fully-scaled samples was attributed to the hierarchical structuring of scales (Figure 10b). The pitch of micro- and nano-grooves formed by LRs and NRs respectively (<1.5µm), is significantly lower than the diameter of sessile drops (3.77 mm), thereby restricting penetration via capillary pressure (151). Consequently, air pockets become entrapped by drops and the surface exhibits Cassie-Baxter wetting (35,36), resulting in a low contact area, and thus low adhesion.

In the absence of scales, CAs significantly decreased ($p < 0.001$), whilst RAs significantly increased ($p < 0.01$; Table 1 and 2). The CAs recorded from descaled samples were high (CA > 90°), suggesting that the discal membrane can be classified as hydrophobic. However, despite this, drop retention was very high for all directions (RAs > 70°) leading to the discal membrane being classified as 'sticky'. These results corroborate the hypothesis 1.3. which predicts that scales enhance hydrophobicity.

The negative effect of scale removal on surface wettability was attributed to the observed disparity in roughness between fully-scaled and descaled samples. Potential chemical effects were not considered due to the relatively similar chemical composition of both the wing membrane and scales (152). SEM images taken of the descaled membrane demonstrated a one-

tier ridge pattern constituted by scale insertion points (Figure 10c). The width between membrane ridges (~195.7µm; Figure 10c) was considerably larger than the width of scale microgrooves (1.46µm; Figure 10b), which led to increased discontinuity of drop suspension upon air pockets entrapped within insertion points (28,153). Consequently, drops become more embedded within roughness features, resembling Wenzel wetting (34), which results in a larger contact area, and thus increased adhesion.

The hydrophobicity of fully-scaled samples was lower than expected when compared to existing literature (48,105,115–117). This could be attributed to limitations of the experimental method. Firstly, CA and RA measurements were taken manually, making them susceptible to inconsistency due to human error. Accuracy can be improved by standardising data collection using automated methods, such as orthogonal camera goniometry (154,155); or a motorised rotation stage (136). Furthermore, the standard drop size used for data collection was relatively large (16µl), and thus susceptible to gravitational distortion. This resulted in drops appearing less spherical (156). Additionally, larger drops demonstrate increased shedding from surfaces due to increased gravitational inertia (157). Existing literature for both biological and industrial surfaces typically employ a standard drop size of 5µl (26,70,115,119,136,158), which can be achieved in future experiments by depositing drops using a syringe rather than a pipette.

4.2 H2. The shedding of drops from the discal scale-layer is directional

Overall, the outward, inward and lateral RAs recorded from the discal scale-layer suggests that drop shedding was directional, with outward RAs being significantly lower than inward RAs ($p < 0.001$; Figure 11a), but not lateral RAs ($p > 0.05$). Therefore, hypothesis 2.1 was only partially satisfied.

Consistent with existing studies on *Morpho aega* butterflies (48,118), directional shedding was attributed to longitudinal asymmetry observed within the discal scale-layer (Figure 10a and 10b). SEM images demonstrated that discal scales were organised into a periodic stepwise hierarchy orientated towards the apical edge (Figure 10a). Additionally, the LRs upon the discal scale surface demonstrated a clear sawtooth pattern orientated towards the scale tip (Figure 10b). Significantly lower outward RAs, suggest that the observed asymmetric features constitute direction-dependent energy barriers against the leading contact line of moving drops (118,121,122).

However, the directionality of drop shedding observed upon *Attacus* wings was less extreme compared to *M. aega* wings. Such discrepancies were attributed to ecology-driven structural differences of LRs. As previously discussed in section 1.4, the surface of lepidopteran wings is multifunctional. The evolution of striking blue structural colours upon *M. aega* wings has driven LRs upon scales to become highly structured, resulting in a large step-height of inward energy barriers (109,118,124). This, in turn, leads to significant disparity between inward and outward drop retention.

In contrast, the sawtooth structure of LRs upon *Attacus* scales was less distinct (Figure 10b), likely due to an absence of structural colours. Consequently, the step-height of longitudinal asymmetry is reduced, resulting in low inward energy barriers (124), and thus decreased disparity between outward and inward drop retention.

The facilitation of directional drop shedding by scale structuring and organisation is further supported by no significant differences being found between outward, inward and lateral RAs recorded from descaled discal samples (Figure 11b). This suggests that drop shedding from the descaled discal membrane was non-directional, thereby satisfying hypothesis 2.3. A lack of directionality is attributed to the absence of direction-dependent energy barriers, resulting from symmetrical structuring of the discal membrane surface (Figure 10c).

On fully-scaled samples, no significant differences were observed when comparing lateral RAs with either outward or inward RAs (both p-values >0.05; Figure 11a), which was attributed to the tiling patterns of discal scales. Within the scale-layer, the lateral overlapping of discal scales was weaker compared to longitudinal overlapping (Figure 10a). Therefore, the step-height of the resulting hierarchy was reduced. Consequently, lateral energy barriers exerted a less obstructive effect on the advancing contact line compared to inward energy barriers (124), resulting in intermediate lateral RAs. Furthermore, testing of lateral drop retention on excised wing samples was constrained by the disregard of macroscale surface features, such as longitudinal veins, which are likely to significantly restrict drop movement (136,159).

Documented directional shedding is often related to the optimisation of self-cleaning (5,117,118,120,160). This study proposes an additional benefit of directional shedding regarding the acoustic defence of *Attacus* moths. *Attacus* wings possess acoustic decoys in the form of heavily folded lobed wingtips, which act as retroreflectors of ultrasonic bat calls (128). Acoustic decoys produce a louder ultrasonic signal than the thorax, which diverts bat attacks towards wingtips. The efficacy of acoustic decoys is contingent upon a high disparity between the

reflected signals produced by the thorax and wingtips (128). Such disparity is enhanced by sound absorbing thoracic scales (132). It is likely that waterlogging of the thoracic scale-layer will result in the expulsion of entrapped air-pockets, causing a dampening effect (161,162), leading to a louder thoracic signal. Consequently, the control of drop movement away from the thorax via directional shedding may be beneficial in maintaining signal disparity, which in turn confers a high fitness benefit.

4.3 H3. The discal scale-layer produces less damaging impact dynamics of colliding drops.

High speed videography demonstrated that drops shattered upon impact with the discal scale-layer (Figure 12), suggesting that the discal surface exhibits a low shatter threshold (We_c) (97,163). In fact, the We_c (27.58) observed within this study is extremely low regarding previous impact studies on both biological and industrial surfaces (94,164–167). This is particularly impressive when compared to industrial surfaces, where, unlike the *Attacus* wing membrane, cushioning of impact force via elastic deformation is minimal, and thus drops are expected to shatter more readily at low *We* numbers (103).

This phenomenon has high ecological relevancy regarding the ecology of *Attacus* moths which reside in dense tropical rainforests, and thus are more likely to encounter lower velocity drops formed by canopy run-off (86). As drops were standardised across experiments, a low We_c was attributed to the strong hydrophobicity constituted by hierarchical structuring of discal scales (100,102,167–170) (Figure 10b).

The classification of impact metrics recorded nucleation across all discal impacts (Table 3). As discussed in section 1.3.5., nucleating holes occur during radial spreading, when the troughs of propagating waves encounter roughness features (95), and thereby are facilitated by a high magnitude of hydraulic shock (52). This implies that drops impact the discal scale-layer with a sufficient magnitude to effectively generate nucleating holes (95,102). This effect was attributed to the paddle-like morphology of discal scales, which have a low aspect ratio, and thus are less likely to elastically deform and provide a ‘cushioning effect’ against drop impact (138,139). Additionally, a notably low proportion of residual water remained on the discal surface following impact (Figure 12a, *Frame 196*; Table 3). Low residual water was attributed to the strong hydrophobicity of the discal scale-layer (Table 1; Table 2), resulting in low friction against the advancing contact line during radial spread. Consequently, spreading drops retained a large proportion of inertia, thereby reducing the probability of retraction (55,100).

The observed shatter patterns are consistent with those recorded in similar studies conducted by Lv *et al.* and Kim *et al.* (165,168), in which the formation and radial ejection of satellite drops significantly reduced drop T_c. It can therefore be proposed that the discal scale-layer constitutes a protective 'shatter-coating' which minimises the transfer of impact and shear stress into wings (55,166,168). This was further supported by an absence of surface wetting (Table 3), which suggests that dissipation of impact force was sufficient to prevent a pressure induced Cassie-to-Wenzel transition (37).

However, hypothesis 3.1 cannot be fully satisfied due to the inferential nature of the analysis presented within this study, whereby quantitative metrics, such as nucleation time, maximum spread, drop T_c and the temporal evolution of impact stress, were not directly measured. Therefore, at present, the efficacy of the discal scale-layer as a protective coating cannot be fully discerned. For a more comprehensive survey, future studies should take inspiration from the extensive research history of drop impacts on solid surfaces (65,66,70,171–182), in which high-speed videography is performed in conjunction with direct force estimation and/or computational modelling (66,103,173,182).

Originally, a more complex computational analysis utilising motion-based multiple object tracking of impacting drops was planned, which would have permitted accurate measurement of T_c, nucleation time, and maximum spread. However, low contrast of drops against a highly complex background prevented accurate drop tracking due to excessive noise. To improve the robustness of future drop tracking models, several changes to the experimental set-up could be implemented. First, drop contrast could be improved by (i) incorporating a non-reactive dye into the water reservoir or (ii) using a magnifying lens attachment to crop the field of view (173) Second, background noise reduction could be achieved by utilising a simpler clamping mechanism, such as mounting wings onto a solid substrate.

The temporal evolution of impact stress during drop collisions upon solid surfaces are commonly measured using piezoelectric sensors (172–174). Piezoelectric sensors output force-time curves detailing two key aspects: (i) the maximum force transfer during initial hydraulic shock, and (ii) the rate-of-decay of stress during radial spreading and/or the dispersion of satellite drops (173,174). Given the extremely thin nature of the *Attacus* wing membrane, piezoelectric sensors are proposed as an appropriate method for stress characterization during future drop impact studies, as any potential sensitivity limitations are minimized (173). As wing elasticity predominantly governs maximum impact stress (83,104,171), the rate-of-decay of force times curves are of higher relevance when considering *Attacus* scales as a protective shatter-coating.

Consequently, to satisfy hypothesis 3.1, it is predicted that impacts on the discal scale-layer will exhibit a fast rate-of-decay.

The subsequent data outputted from the synchronisation of high-speed videography, multiple-object tracking and piezoelectric sensors could be used as inputs to generate computer simulations, such as volume of fluid (VOF) models (66,103,171). Such simulations enable detailed analysis of intricate mechanisms, such as drop flow fields, which govern impact dynamics observed in high-speed videos, allowing for better understanding of solid-liquid interactions, like shear stress (66). Additionally, the ability to easily alter impact parameters within simulations means offers high predictive power. For example, systematically reducing drop *We* can facilitate the estimation of the We_c of the discal scale-layer without requiring costly and time-consuming physical trials. This simulated data could then be used to devise new, testable hypotheses for future experimental studies.

The induction of shatter by the discal scale-layer is further supported by classification of impacts upon the descaled discal membrane. In the absence of scales, the frequency of nucleation was significantly lower ($p < 0.001$; Table 3), an effect attributed to reduced surface roughness observed on the discal membrane (Figure 10c). Insertion points constituting membrane roughness demonstrated a reduced density and a smaller aspect ratio compared to discal scales. Consequently, perturbation of the spreading lamella via encounters between propagating shockwaves and surface features was likely reduced (95). Additionally, following scale removal, the frequency of residual drops significantly increased ($p<0.001$; Table 3), which was attributed to the weaker hydrophobicity of the descaled discal membrane (Table 1; Table 2).

Increased surface wettability results in a proportion of lateral inertia being absorbed via friction during radial spread, thereby allowing surface tension to predominate, thereby increasing the probability of lamella retraction (167,170). It is probable that this effect was further exacerbated by increased radial spreading time resulting from reduced nucleation.

Utilising existing data (55,166,168), it can be inferred that an increase in residual water following impact is indicative of a long T_c. Therefore, it can be proposed that drop impacts upon the descaled discal membrane are more damaging than impacts with the discal scale-layer, partially satisfying hypothesis 3.2. No change in surface wetting frequency was observed after scale removal, contradicting hypothesis 3.3. A lack of surface wetting was attributed to the descaled discal surface being classified as hydrophobic (CA >90°), and thus deposition of impacting drops was unlikely (63).

4.4 H4. The mechanical impact of drops damages the discal scale-layer of *Attacus* wings.

SEM imaging of discal scales after 150 impacts demonstrated structural damage, including lateral fractures (Figure 13), bearing striking resemblance to that observed on steel surfaces subjected to repeated impact stress (58). Damage was primarily observed upon microscale structures, such as LRs, whilst NRs within microgrooves remained intact. This suggests that microscale structures act as 'protective buffers' to mitigate nanoscale damage, preserving the HR of the discal scale-layer, and thus its hydrophobic performance of a surface (183). These findings are concordant with existing literature investigating damage upon solid surfaces (49,53).

However, structural damage resulting from repeated drop impact was not a primary focus of this study. Therefore, it is impossible to rule-out that alternative sources of structural scale damage, including mechanical abrasion during sample preparation, may have occurred.

Instead, this study focuses on damage to the discal scale-layer as a collective, rather than individual scales. Firstly, repeated impacts had a non-significant effect on the circular distribution of scale orientations ($p > 0.05$; Figure *14*a), suggesting that repeated impact had no effect on the organisation of the discal scales. Consequently, hypothesis 4.1. was not satisfied. A non-significant effect was attributed to the 'shingle-like' tiling pattern of the discal scale-layer (Figure 10a). Strong lateral and longitudinal overlapping 'locks' scales into a tight configuration, reducing their mobility, and hence susceptibility to misalignment by shear during radial spreading.

It is important to note that the orientation analysis performed on discal scales may have limited accuracy. Strong overlap of scales and low image magnification caused scale boundaries to be less distinguishable during edge detection. Additionally, the performed edge detection did not exclude confounding image features, including microdroplets and descaled patches. Consequently, the resulting output likely contained false edges which masked genuine repeated impact effects during statistical testing. The reliability of the orientation analysis can be improved in future by using high contrast SEM images. This was not possible within the present study as time and budget constraints did not allow for a meaningful sample size to be obtained.

Second, pixel variance (%) significantly increased with increasing impact number (Figure *14*b), suggesting that repeated drop impact resulted in the accumulation of damage within the discal scale-layer. However, the total accumulation of pixel variance over 150 impacts was relatively

low (9.5%), suggesting that the ‘shatter-coating’ constituted by discal scales was effective at mitigating against high levels of damage. It is important to note that image alignment using matched features required a large field of view. Therefore, the total accumulation of pixel variance was likely distorted by portions of the scale-layer unaffected by impacting drops, and therefore underestimated. In an ecological context, the concentration of impacts to a single area is extremely unlikely. Instead, it is more probable that wings will endure multiple impacts distributed across the surface, forming numerous impact sites which accumulate damage. Consequently, *in situ* total accumulation of scale-layer damage across wings will likely be higher compared to controlled laboratory settings.

Figure *14*b, suggests that the first 30 impacts were the most damaging, as indicated by a sharp increase in the rate of change. The observed plateau after 30 impacts was attributed to a reduced number of scales within the impact site available for interactions with further drops. In contradiction to the total accumulation of pixel variance, the observed accumulation curve suggests that the discal scale-layer is easily damaged by low numbers of impacts. This is concordant with visual observations of light microscope images, in which large patches of descaled membrane within the impact site are clearly visible (Figure A1).

To improve the estimation of damage caused by repeated drop impacts, future experiments could employ optical profilometry to create 3D topographical scans of the discal scale-layer before and after impact intervals (58,184). This highly precise and reliable method is widely used across a range of disciplines, including aeronautics and renewable energy, to assess rain erosion on industrial surfaces (184). Topographical scanning enables accurate quantification of damage metrics, such as volume loss of the scales and changes in surface roughness (58,184). Additionally, by combining erosion curves with CA and RA measurements, it is possible to predict the effect of repeated impact damage on the wettability of *Attacus* wings.

Furthermore, to eliminate external factors, like mechanical abrasion, and accurately assess the impact-induced damage to scales, it is crucial to quantify the temporal evolution of shear stress. Mounting of wing samples onto a solid-gel polymer embedded with fluorescent particles and employing traction-force and laser-sheet microscopy (178), allows the propagation of shear stress across the discal scale-layer during impact to be mapped. This information can then be overlaid onto light microscope images to identify genuine patches of scale-layer damage. By analysing the spatial relationship between descaled patches and the shear stress propagation zone, pixel variance analysis can be refined, thereby increasing the accuracy of impact damage quantification.

It can be suggested that low resiliency of the discal scale-layer to damage may provide a short-term 'shock-absorbing effect' against impact, reflective of 'crumple zones' within cars. Mechanical removal of scales by drops, through either breakage or dislodgement, likely absorbs a portion of kinetic energy (185), thereby preventing direct transfer of impact stress into the wing membrane. Therefore, synergy between the discal scale-layer as both a 'shock-absorbing' and 'shatter-inducing' coating may significantly reduce the occurrence of costly membrane damage. However, this causes a trade-off between the benefits of membrane damage prevention (88,129), and the costs of scale-layer damage on the multifunctionality of the wing surface (105,109,113–116).

For example, the acoustic function of *Attacus* wings is likely negatively impacted by high levels of scale-layer damage. This is because broadband sound absorption is dependent on the coupling of independently tuned neighbouring scales (106,113,114). Loss of scales narrows the frequency range of echolocation calls across which absorption occurs, thereby increasing the detectability of moths by predatory bats (101,102). Descaled patches of membrane are associated with increased acoustic reflectivity (114), which may contribute to the disruption of acoustic crypsis by creating louder, more detectable signals. Originally, acoustic tomography was intended to be performed in parallel with impact trials to assess the effect of damage on the acoustic functionality of *Attacus* wings. However, due to time constraints and the unavailability of necessary equipment, this was not possible.

Hypothesis 4.2 predicted that damage accumulation would gradually degrade the efficacy of the discal scale-layer as a 'shatter-coating'. This was partially satisfied by the classification of impacts upon the damaged discal scale layer (Table 4). Following damage, the frequency of nucleation significantly decreased ($p < 0.01$), whilst residual drops significantly increased ($p < 0.01$), which suggests that damage accumulation results in a reduction in shatter. As discussed previously in section 4.3, the reduction in shatter observed was attributed to decreased surface roughness and increased wettability resulting from exposed patches of membrane.

However, the detrimental effect of impact damage on drop shatter was less pronounced than that of complete scale removal, in which 2x less nucleation and 3.5x more residual drops was observed (Table 3). Furthermore, the accumulation of damage had no effect on the frequency of surface wetting ($p > 0.05$). Consequently, it can be proposed that the functionality of the discal scale-layer as a 'shatter-coating' exhibits resilience to repeated impact.

4.5 H5. The wettability of *Attacus* wings varies regionally

4.5.1 Surface wettability

As with the discal scale-layer, the CAs and RAs recorded from apical and basal samples fell below standard thresholds, and therefore cannot be classified as superhydrophobic (Table 5).

Nevertheless, both apical and basal CAs were very high (CAs >140°), thereby classifying the apical and basal surfaces as strongly hydrophobic. No significant regional effects were found between apical, discal or basal CAs ($p > 0.05$; Figure 17a), suggesting that apical, discal and basal scales constitute an equally strong hydrophobic surface irrespective of their differing morphology. The absence of regional effects on CA was attributed to the indistinguishable hierarchical structuring of apical, discal and basal scale surfaces (Figure 10b; Figure 16b and d).

Additionally, both apical and basal RAs, recorded in all directions, were very low (apical RAs <20°; basal RAs <25°), suggesting that drops exhibited low adhesion. This, in turn, defines the apical and basal surfaces as 'slippery'. For all directions, no significant differences were observed between apical and discal RAs ($p > 0.05$; Figure 17b), suggesting that drops are shed with equal efficiency from both surfaces. This was attributed to the identical 'shingle-like' tiling patterns of paddle-like apical and discal scales (Figure 10a; Figure 16a). Conversely, basal RAs were significantly higher than discal RAs for all directions ($p < 0.01$), and apical RAs for outward and lateral directions ($p < 0.01$; Figure 17b), which suggests that drop shedding becomes increasingly difficult towards the thorax.

Increased drop retention by the basal scale-layer was attributed to the elongated ribbon-like morphology of basal scales (Figure 16d). A high aspect ratio results in high flexibility (138) which may enable reorientation by drops via interfacial attraction. This was further supported by significantly higher 'cupping' being exhibited by basal scales compared to apical and discal scales ($p < 0.001$; Figure 18), resulting in a greater contact area between drops and scales, thereby increasing drop adhesion. As with discal samples, scale removal resulted in a significant decrease in CAs ($p<0.001$; Table 5), and a significant increase in RAs ($p<0.01$; Table 6) measured from apical and basal samples. For both regions, the descaled membrane was classified as a hydrophobic surface (CAs >90°), exhibiting extremely high drop retention in all directions (apical RAs: > 80°, basal RAs > 60°). This suggests that the inherent hydrophobicity of the apical and basal membranes was enhanced by the presence of scales. As discussed previously in section 4.1., the reduction in hydrophobicity recorded from descaled apical and basal samples was attributed to decreased surface roughness.

4.5.2 Directional shedding

Overall, outward, inward and lateral RAs recorded from apical and basal samples suggest that drop shedding was directional. For apical samples, inward RAs were significantly higher than both outward ($p < 0.001$) and lateral RAs ($p < 0.01$; Figure 19a, *Left panel*). As with discal samples, the strong directionality of drop shedding from apical samples was attributed to longitudinal asymmetry, consisting of an outward stepwise scale hierarchy (Figure a) and distinct sawtooth patterning of LRs (Figure 19b). An additional significant effect between inward and lateral RAs, which was not observed for discal samples, suggests that longitudinal asymmetry within the apical scale-layer results in stronger inward energy barriers compared to the discal scale-layer (124).

Conversely, directional shedding observed within basal samples was concordant with that observed in discal samples, in which inward RAs were significantly higher than outward RAs ($p < 0.05$), but not lateral RAs ($p > 0.05$; Figure 19b, *Left panel*). However, the directional effect between outward and inward RAs in basal samples was less significant compared to apical and discal samples (Figure 11; Figure 19), suggesting that shedding from the basal region is less directional. Weaker directionality was attributed to reduced longitudinal asymmetry within the basal scale-layer, resulting from the absence of sawtooth patterning upon LRs (Figure 16d) (124). Additionally, the high flexibility of basal scales increases the probability of elastic deformation driven by the hydraulic pressure of advancing drops (98,138). Consequently, inward energy barriers, resulting from the stepwise organisation of basal scales, may have a weaker effect compared to the stepwise hierarchies of apical and discal scales (121).

The facilitation of directional drop shedding by apical and basal scales was further supported by the absence of significant differences between outward, inward and lateral RAs recorded from descaled samples (Figure 19b), which suggests that drop shedding was non-directional. As with discal samples, this effect was attributed to symmetrical surface structuring of the apical and basal membranes.

The observed results suggest that regional variation in scale morphology establishes a drop retention gradient across *Attacus* wings, which may allow for finer control of drop movement, thereby satisfying hypothesis 5.1. Firstly, drop adhesion becomes stronger towards the basal region. It can be proposed that higher drop retention in the basal region intercepts inward-travelling drops from the apical and discal regions before they reach the thorax, thus acting as a final ‘buffer zone’ against thoracic wetting. Secondly, the directionality of drop shedding becomes increasingly pronounced towards the apical region. Towards the basal region, outward shedding becomes increasingly difficult due to the distance that drops must traverse, which in

turn increases the probability of pinning by particulates or damage. Furthermore, outward drop shedding from the apical region is likely facilitated by downward wing flexion, particularly during drop impact (84), with the effect diminishing towards the wing joint (82). Consequently, it is inferred that an increased magnitude of directionality towards the apical region may improve shedding efficiency by restricting inward drop movement into regions where outward shedding becomes more challenging.

4.5.3 Impact resilience: Drop shatter

As with the discal region, high-speed videography demonstrated that drops shattered upon impact with the basal scale-layer (Figure 20), suggesting that variation in scale morphology had no effect on We_c. This was expected, given that both the discal and basal regions exhibited similarly strong hydrophobicity (Figure 17) and indistinguishable hierarchical structuring of scales (Figure 10; Figure 16).

Whilst shatter was recorded in both regions, the shatter dynamics observed in the basal region differed from the discal region. Nucleation was significantly less frequent during basal impacts ($p < 0.01$; Table 3, Table 7). As previously discussed in section 4.3., the formation of nucleating holes is dependent on the magnitude of hydraulic shock (52). It is therefore proposed that entrapped air-pockets within the 'fur-like' basal scale-layer (132) may provide a 'cushioning effect' against drop impact (186,187). Cushioning of impacts serves to reduce the magnitude of hydraulic shock, thereby decreasing the probability of encounters between propagating waves and roughness features. However, a low *We* reduces the efficiency of impact cushioning (187) which may explain why nucleation was still observed 60% of the time.

Despite reduced nucleation, a low proportion of residual water remained on the basal surface after impact (Figure 20, *Frame 196*), particularly regarding residual drop frequency (Table 7). No significant differences were found between the residual frequency recorded for both discal and basal impacts ($p > 0.05$; Table 3). This effect was attributed to strong hydrophobicity of the basal scale-layer, which likely resulted in low absorption of lateral inertia via friction (55,100), despite retraction of the liquid lamella being observed (Figure 20, *Frame 20*). Consequently, satellite drops retained a large portion of kinetic energy and thus were ejected.

The observed basal shatter patterns were consistent with those recorded from discal impacts and previous studies (55,166,168). Therefore, it is inferred that the basal scale-layer constitutes an equally effective 'shatter-coating' which minimises potential impact damage. As with discal impacts, this inference was further supported by an absence of surface wetting (Table 7).

4.5.4 Impact resilience: Damage accumulation

Hypothesis 5.2. predicted regional variation in the resilience of *Attacus* wings to impact damage. This was satisfied by the results of circular analysis, polynomial regression and the classification of impacts following damage.

Figure 21a, demonstrated that the circular distribution of scale orientations became significantly wider after repeated drop impact ($p > 0.001$), suggesting that repeated impacts cause the basal scale-layer to become more disorganised. This effect was attributed to the highly flexible elongated morphology of basal scales (Figure 16c). Therefore, it is inferred that basal scales respond elastically to impact, rendering them more susceptible to misalignment compared to discal scales. However, disorganisation of the basal scale-layer may be as detrimental to its functionality as scale removal. Repeated misalignment against a preferred orientation may result in excessive strain, leading to inelastic deformation or even complete breakage of basal scales (138,188). Consequently, the basal scale-layer becomes less dense, and thus more susceptible to wetting (140).

Pixel variance (%) increased significantly with increasing impact number (Figure 21b), suggesting that repeated drop impact led to the accumulation of damage within the basal scale-layer. Like the discal region, the output accumulation curve suggested the first 30 impacts to be the most damaging, suggesting that both regions exhibited a comparably low resilience to damage accumulation in response to repeated impacts.

A significantly higher total pixel variance was recorded in the basal region compared to the discal region ($p < 0.05$), which suggests a lower resilience of the basal scale-layer to impact damage. This was expected, given that nucleation was recorded significantly less frequently during basal impacts (Table 7). Nucleation reduces the time in which the spreading lamella fragments into satellite droplets, thereby minimising T_c (95). Therefore, it can be inferred that the liquid lamella contacted the basal scale-layer for longer before the onset of shatter, resulting in a greater transfer of stress into the basal surface (71).

It is important to note that increased pixel variance across basal images may be influenced by constraints of the conducted image analysis. The utilised image analysis procedure was unable to differentiate between genuine damage, resulting from scale loss, and confounding factors, such

as scale movement or entrapped microdroplets. Such confounding was more probable in basal images due to the increased flexibility of basal scales.

4.5.5 Impact resilience: Effect of damage on drop shatter

Following damage, the frequency of nucleation significantly decreased ($p < 0.05$), while residual drops significantly increased ($p<0.01$), suggesting that damage accumulation decreases the efficacy of the basal scale-layer as a 'shatter-coating'. Interestingly, nucleation decreased at an equal rate across the discal and basal regions (Tables 3 and 7). This observation is consistent with damage accumulation curves plotted for both regions (Figure 14b; Figure 21b), suggesting that repeated impact gradually degrades the discal and basal scale-layers at a comparable rate across *Attacus* wings. However, the basal region exhibited a significantly higher damage-driven increase in residual drop frequency compared to the discal region (Tables 3 and 7), which suggests that whilst deterioration of the discal and basal 'shatter-coating' efficiency is relatively uniform, the subsequent consequence of such deterioration is significantly more pronounced in the basal region. This effect was attributed to disparity in the shatter dynamics observed during basal and discal impacts prior to damage.

During basal impacts, the spreading liquid lamella retracted prior to the onset of nucleation (Figure 20, *Frame 20*). Notably, such retraction was absent during discal impacts (Figure 12, *Frame 12*). As previously discussed, retraction results in increased absorption of lateral inertia (100). Prior to damage, such effects were negligible, likely a consequence of strong hydrophobicity of the basal surface. However, as the basal scale-layer becomes more damaged, it's hydrophobic properties decrease, resulting in increased resistance against the spreading lamella, and thus absorption of lateral inertia is exacerbated (55,100).

The frequency of surface wetting frequency in the basal region remained unchanged following damage. This contradicted the discal region, where a significant 10% increase was observed ($p <0.05$). However, the conducted McNemar tests were heavily skewed by frequency values of 0, and thus the resulting p-value is likely to be overestimated. Consequently, it is unwise to draw any firm conclusions regarding the biological significance of this effect without conducting further tests with a larger sample size.

4.6 H6. The drop interactions of transparent wing regions differ from fully scaled regions

4.6.1 Surface wettability

Hypothesis 6.1. predicted that the scales within transparent wing regions would constitute reduced hydrophobicity compared to scales within opaque regions. This was not satisfied by CA and RA results recorded from TW and *M. confusa* samples.

As with opaque regions, the CAs and RAs recorded from transparent samples fell below standard thresholds (Tables 8 and 9), and thus cannot be classified as superhydrophobic. Unexpectedly, both TW and *M. confusa* CAs were very high (CAs >140°), thereby classifying the TW and *M. confusa* surfaces as strongly hydrophobic. No significant regional effects were found when comparing transparent and opaque regions across *Attacus* and *M. confusa* wings ($p > 0.05$; Figure 23a), suggesting that transparent scales constitute an equally hydrophobic surface as opaque regions, despite having a reduced scale-layer (Figure 22a and c). The absence of significant effects was attributed to the hierarchical structuring of TW and *M. confusa* scales (Figure 22b and d), which closely resembles the surface of opaque scales (Figure 10b; Figure b and d)

TW and *M. confusa* RAs, recorded in all directions, were very low (TW RAs <20°; *M. confusa* RAs <10°), suggesting that drops exhibited low adhesion. This, in turn, defines the TW and *M. confusa* surfaces as 'slippery'. Unexpectedly, TW RAs were more concordant with those measured from apical and discal samples, rather than basal samples. In fact, no significant differences were found between apical, discal or TW RAs ($p > 0.05$; Figure 23b), suggesting that hair-like TW scales constitute an equally 'slippery' surface as paddle-like apical and discal scales. Initially, it was expected that the TW scale-layer would exhibit drop retention more like the basal scale-layer due to similar scale morphologies(Figure 16d and Figure 22a). TW RAs were significantly lower than basal RAs in an outward direction ($p < 0.05$), but not inward or lateral directions ($p > 0.05$; Figure 23b).

Significant outward effects were attributed to the low aspect ratio morphology of TW scales (Figure 16d), resulting in reduced flexibility (138), which, in turn, restricts reorientation by drops via interfacial attraction. This was further supported by 'cupping' being exhibited by TW scales which was equal to apical and discal cupping ($p > 0.05$), but significantly lower than basal cupping ($p < 0.001$; Figure 24). Reduced cupping results in a smaller contact area between drops and TW scales, thereby decreasing drop adhesion.

Conversely, RAs measured from *M. confusa* samples were extremely low compared to *Attacus* regions, particularly in an outward direction ($p < 0.05$; Figure 23b). This effect was attributed to the unique scale morphology observed upon *M. confusa* samples (Figure 22c). The elongated

cover scales of *M. confusa* wings resemble specialised scales observed in *P. sita* butterflies (145), and thus are inferred to exhibit similar elastic responses. Elastic deformation of scales under the weight of sessile drops prevents contact with the wing membrane by increasing contact area, whilst the elastic recovery of scales around the drop boundary facilitates the suspension of drops, resulting in extremely low adhesion (145).

The CAs measured from across *Attacus* and *M. confusa* wings were exceptionally high (all mean CAs >140°) and precise (mean standard deviation range = 1.66° - 6.60°) (Table 1; Table 5; Table 8). Whilst, falling short of lotus leaves (160.1° ± 0.7°) (5), these CAs are remarkably impressive when compared to commercially available synthetic hydrophobic polymers, such as: polyfluorotetraethylene (or Teflon) (mean CA ≈ 107.0° ± 3.41°) (189–193); Teflon AF1600 (mean CA ≈ 121.8° ± 3.63°)(194–196); and polydimethylsiloxane (PDMS) (mean CA ≈ 107.9° ± 4.05°) (197–200). On average *Attacus* and *M. confusa* wings demonstrated CAs approximately 35° and 40° higher, respectively, than these polymers.

Similar precision was observed during outward drop shedding from *Attacus* and *M. confusa* wings (mean standard deviation range = 2.25° - 2.91°), except for the *Attacus* basal region (mean standard deviation = 9.48°), where measurements were less consistent due to irregular surface roughness caused by elongated scales (Figure 16). Whilst direct comparison of RAs to hydrophobic polymers is challenging due to the reporting of CAH, it is evident that drops shed more readily from *Attacus* and *M. confusa* wings (all mean RAs <8°) compared to Teflon (CAH ≈ 34.3° ± 15.84°) (189–191,193) and PDMS (CAH ≈ 26.9° ± 7.21°) (197,198). Additionally, unlike *Attacus* and *M. confusa* wings, hydrophobic polymers typically exhibit symmetrical surface roughness (189,198) and thus lack evidence of directional drop shedding. As a result, only outward RAs measured from *Attacus* and *M. confusa* wings are discussed.

Consequently, this study demonstrates that *Attacus* and *M. confusa* wings possess superior hydrophobic properties, particularly in terms of dynamic drop interactions, compared to commercial hydrophobic polymers. The lack of directionality upon commercial coatings limits their widespread application, especially in areas requiring precise droplet control, such as smart self-cleaning fabrics.

To enhance the hydrophobicity of polymers, surface roughness is often increased either chemically, using plasma treatments (191,192), or physically, by etching, imprinting or embossing (190,197,199). By studying the unique surface topography of lepidopteran wings

further, with a particular focus on how such surfaces can be replicated, valuable insights in how to optimise the design of commercial hydrophobic coatings can be gained.

As discussed in section 4.1., the CAs recorded from transparent samples were likely strongly influenced by a large drop size (16µl). In addition to gravitational distortion, large drops may reduce the efficacy of elastic suspension exhibited by *M. confusa* scales via prevention of elastic recovery around the drop boundary (134), and thus CAs may be underestimated.

As with opaque samples, scale removal resulted in a significant decrease in CAs ($p < 0.001$; Table 8), and a significant increase in RAs ($p < 0.01$; Table 9) measured from TW and M. confusa samples. The descaled *M. confusa* membrane was classified as a hydrophobic surface (CA >110°), exhibiting high drop retention in all directions (RAs >75°). Conversely, the descaled TW membrane exhibited lower hydrophobicity than both opaque and *M. confusa* surfaces (CA <90°), but lower drop retention (RA <60°). This effect was attributed to an observed disparity in surface roughness, constituted by the organisation of insertion points upon the descaled TW and *M. confusa* membranes (see Appendix 1.2.).

4.6.2 Directional shedding

Overall, outward, inward and lateral RAs recorded from TW and *M. confusa* samples suggest that drop shedding was directional. For both transparent regions, outward RAs were significantly lower than both inward ($p < 0.05$) and lateral RAs ($p < 0.01$; Figure 25a and b, *Left panel*). As with opaque samples, directional drop shedding from was attributed to longitudinal asymmetry, consisting of an outward stepwise scale hierarchy (Figure 22a and c), and distinct sawtooth patterning of scale LRs (Figure 22b and d).

However, the outward-inward directionality observed in transparent regions was less significant ($p < 0.05$) than apical and discal regions ($p < 0.001$), more closely resembling the directional effects observed for the basal region. The TW and *M. confusa* scale-layers lack strong overlapping of neighbouring scales both longitudinally and laterally, resulting in a reduced periodic stepwise hierarchy (Figure 22a and c). Furthermore, TW and *M. confusa* scales exhibit an elongated morphology, and thus may deform elastically in response to the hydraulic pressure of inward-advancing drops (98,138), therefore reducing the efficacy of direction-dependant energy barriers.

Strong directionality between outward and lateral tilt directions was attributed to large inter-scale space (Figure 22a and c), resulting from reduced scale-layer density. When tilted laterally, the large inter-scale space may cause the advancing contact line to become pinned due to increased contact with the less hydrophobic wing membrane. Enhanced directionality against lateral drop movement is advantageous when considering excised transparent samples in the context of the overall wing structure. In both instances, samples were obtained from the centre of wings (Figure 2). Therefore, lateral movement of drops is difficult due to a large shedding distance, and a high probability of the contact line becoming pinned by longitudinal veins. Consequently, the presence of strong directionality inhibits lateral movement, thereby enhancing drop control, and facilitating the efficient shedding of drops from wings.

The facilitation of directional drop shedding by TW and *M. confusa* scales was further supported by the absence of significant differences between outward, inward and lateral RAs recorded from descaled samples (Figure 25b and d). This suggests that drop shedding was non-directional. As with opaque samples, this effect was attributed to symmetrical surface structuring of the TW and *M. confusa* membranes (Figure A2).

4.6.3 Impact resilience: Drop shatter

As with opaque regions, high-speed videography demonstrated that drops shattered upon impact with the TW and *M. confusa* scale-layers (Figure a and b), suggesting that variation in scale morphology and scale-layer density had little effect on We_c. This was expected, given that transparent regions exhibited strong hydrophobicity, and hierarchical structuring of scales which resembled that of opaque regions.

Whilst shatter was recorded across all regions, regional differences in shatter dynamics were observed. The frequency of nucleation observed during transparent impacts were more concordant with discal impacts than basal impacts (Table 3; Table 7; Table 10). However, this effect was non-significant ($p > 0.05$). This suggests that a reduced scale-layer, necessary for transparency, does not impede the induction of drop shatter (97,163). As with discal impacts, the facilitation of drop shatter by scales was further supported by the classification of impacts upon the descaled TW membrane (Table A2), in which nucleation significantly decreased ($p < 0.01$).

However, whilst the induction of drop shatter is relatively equal across transparent and opaque regions, a significantly higher proportion of residual drops remained on the TW and *M. confusa* surfaces following impact ($p < 0.05$; Table 10; Figure 26a, *Frame 266*; Figure 26b, *Frame 90*). This suggests that impact stress was not dispersed via the ejection of satellite drops as effectively

in transparent regions compared to opaque regions. Therefore, it is inferred that T_c is greater during transparent impacts (95,168), resulting in impacts which are more damaging.

The increase in residual drops observed in transparent regions was attributed to large inter-scale space. A high proportion of exposed membrane increases resistance against the spreading liquid lamella, leading to a portion of a drop's inertia is lost via friction (55,100). Therefore, the probability of satellite droplets being ejected from the surface is reduced. This effect was more pronounced in the TW region, in which residual drops were observed 30% more frequently (Table 10). This was attributed to retraction of the liquid lamella prior to nucleation which was observed during TW impacts (Figure 26a, *Frame* 17), but not *M. confusa* impacts (Figure 26b, *Frame* 15).

Finally, the frequency of surface wetting observed during transparent impacts was low (Table 10), suggesting that despite an inferred high transfer of force, the lateral dissipation of impacts by the TW and *M. confusa* scale-layers was sufficient to prevent a Cassie-to-Wenzel transition (37). Consequently, it is proposed that whilst the 'shatter-coating' constituted by TW and *M. confusa* scales is less effective at dissipating impact stress, it remains a robust protective mechanism against impact-driven wetting of wings.

One factor not considered within this study was the effect of surface tension on the drop impact dynamics observed during collisions with *Attacus and M.confusa* wings. Temperature and solute concentration significantly influences the surface tension of drops (201–204). From an environmental perspective, the impact of reduced surface tension on drop impact dynamics may be particularly relevant due to increased global surface temperature (4) and pollution of hydrological systems by industrial effluents (205–207).

The effect of surface tension on drop impacts with *Attacus* and *M. confusa* wings could be investigated using the experimental set-up outlined in *section 2.4.2.* The surface tension of drops can be systematically decreased by adding increasing concentrations of surfactant, such as Triton X-100 or dish soap, into the water reservoir (208). Low surface tension increases the dominance of inertial forces during impacts, leading to higher *We,* and increased drop shatter (69,95,96,208). As a result, impacts of surfactant solutions on *Attacus* and *M. confuse* wings are predicted to result in two outcomes. First, drops will shatter without retraction of the liquid lamella across all wing regions, not just the discal and *M. confusa* regions (Figure 12a; Figure 20a; Figure 26a and b). Second, as surfactant concentration increases, drops are expected to

shatter more readily, as indicated by decreased duration of impact, increased nucleation frequency and the absence of residual drops or surface wetting.

4.6.4 Impact resilience: Damage accumulation

Hypothesis 6.2. predicted that transparent regions would be more susceptible to the accumulation of damage than opaque regions. This was partially satisfied by the results of a polynomial regression and the classification of impacts following damage.

As with opaque regions, pixel variance (%) increased significantly with increasing impact number (Figure 27), suggesting that repeated impacts resulted in the accumulation of damage within the TW scale-layer. The total accumulation of pixel variance (%) within the TW region did not differ significantly from that observed in the discal and basal regions ($p > 0.05$). This was unexpected when considering the classification of shatter dynamics, which suggested TW impacts to be more damaging compared to discal or basal impacts.

Additionally, in contrast to opaque regions, damage accumulation within the TW scale-layer was linear. The rate of scale-layer damage will always eventually plateau when the number of scales in which an impacting drop can contact diminishes. Therefore, the linear model observed for the TW region (Figure 27), implies that damage accumulation is occurring at a slower rate compared to opaque regions (Figure 14b; Figure 21b). Consequently, it is proposed that TW scale-layer exhibits higher resiliency to impact damage than opaque regions, despite a reduced scale-layer.

The advantage of high resiliency of the *Attacus* TW against impact damage is hard to infer because at present the functionality of optically transparent patches is debatable. However, it can be proposed that high resiliency may as a ‘counteractive measure’ to mitigate increased susceptibility to loss of optical function via complete scale-loss, resulting from a reduced scale-layer.

An unexpectedly low total pixel variance recorded for the TW region may be attributed to limitations during image analysis. A smaller sample size of TW images (N=9), compared to discal (N=14) and basal images (N=12), were used during analysis. This was because the KAZEfeature detector was less robust against false positives due to a general lack of contrast between TW scales and the membrane, and the formation of glare. Consequently, matched features were not detected as effectively, resulting in poor image alignment. In cases where this effect was extreme, images were discounted to control for confounding effects.

4.6.5 Impact resilience: Effects of damage on drop shatter

Like opaque regions, the frequency of nucleation observed during TW impacts following damage significantly decreased ($p < 0.01$), whilst residual drops significantly increased ($p < 0.01$; Table 10). This suggests that damage accumulation decreases the efficacy of the TW scale-layer as a 'shatter-coating'. The reduction in nucleation frequency following damage was relatively similar across *Attacus* wings ($p > 0.05$; Tables 4, 7, and 10), suggesting that 'shatter-coating' efficacy is degraded at similar rates. However, the consequence of 'shatter-coating' degradation was more pronounced in the basal region, as represented by a greater increase in residual drops (Tables 7 and 10). This was attributed to disparity in scale-layer density observed between the TW and basal region. The TW scale-layer is sparse, with a high proportion of wing membrane visible (Figure 22c). Therefore, the magnitude of deterioration of surface wettability and roughness driven by impact damage is likely to be smaller compared to the dense basal scale-layer (Figure 16c).

In contrast, the frequency of both nucleation and residual drops observed during *M. confusa* impacts, following damage, significantly increased ($p < 0.01$; Table 10). An increase in nucleation suggests that damage of the *M. confusa* scale-layer leads to an increase in hydraulic shock of impacting drops (166). In section 4.6.1., it was proposed that *M. confusa* scales respond elastically to sessile drops to configure a strongly hydrophobic surface (145). It is possible that such elastic responses provide an 'absorbing effect' against drop impact, like trichomes (138,139). Consequently, damage may cause scales to lose their elastic potential, diminishing absorbing effects, and thus increasing the amplitude of hydraulic shock.

Finally, following damage, transparent regions were more susceptible to surface wetting, as demonstrated by a significant increase in surface wetting ($p < 0.001$; Table 10). As previously discussed, increased residual drop frequency implies a greater T_c, and thus higher transference of force into surfaces. The increased surface wetting observed in transparent regions following impact suggests that, unlike opaque regions, increased force transfer, resulting from scale-layer damage, was sufficient to trigger a Cassie-to-Wenzel transition (37). This effect was attributed to the reduced scale-layer of transparent regions. Previous classification of transparent impacts prior to damage, suggested that transparent regions were less effective at dispersing impact force compared to opaque regions (Table 7; Table 10). Therefore, it is proposed that transparent regions were more predisposed to damage-driven Cassie-to-Wenzel transitions, thereby satisfying hypothesis 6.3.

4.7 Conclusions

To conclude, this study has identified *Attacus* wings as a strongly hydrophobic surface, which utilises regional variability in directional drop retention for enhanced control of drop movement. Additionally, *M. confusa* wings were identified as a surface which exhibits both optical transparency and strong hydrophobicity. This study has also uncovered a new potential functionality of the lepidopteran wing surface- where the presence of scales constitutes 'shatter-coating' to provide resilience against impact damage. Ecologically, impact resilience is likely to be further enhanced by elastic responses of wings, particularly toward the apical edge (82). Such effects should be quantified in future research before considering *Attacus* wings as an appropriate biomimetic model.

Attacus and *M. confusa* wings have very promising biomimetic potential, particularly when considering multi-functionality. Utilisation of lepidopteran wing surfaces as biomimetic models is favourable, as this would reduce the need for development of multiple surfaces for different industrial application. Yet, at present, this study would not deem *Attacus* or *M. confusa* wings as an appropriate model for surfaces intended for external use. This is because repeated impact testing demonstrated a low resilience of wings to surface damage typical of current artificial superhydrophobic surfaces. This is especially important, when considering that this study utilised drops falling at a fraction of the *We* and impact velocity exhibited by natural rainfall (67). However, this study did not quantify the transfer of impact force directly, and thus results cannot be extrapolated to more natural conditions. Ultimately, the results of this study provide an encouraging baseline from which more rigorous testing can be conducted to provide a more conclusive assessment of lepidopteran wing wettability, which could one day be utilised to develop effective biomimetic superhydrophobic surfaces.

Acknowledgements

Firstly, I would like to thank my supervisor Professor Marc Holderied for his continued support throughout this project, advising me with my methodology and data analysis, and suggesting improvements for the data collection and subsequent write-up. Your support was invaluable to me and without it I doubt the outcome of this project would be where it is.

I would also like to thank my co-supervisor Professor Ulrike Bauer who significantly aided with the impact resilience portion of this project. Without your expertise a large portion of this project would not have been possible. I would also like to thank you for continued access to your lab and equipment. I extend my gratitude to your lab group for being so welcoming, particularly Nathanael Tan, who greatly assisted me when conducting high-speed videography.

Finally, I would like to acknowledge my family, and partner Beth for their continued support throughout the duration of this project, particularly during the write-up process. I couldn't have done it would you.

Bibliography

List of references

1. Boinovich LB, Emelyanenko AM, Ivanov VK, Pashinin AS. Durable Icephobic Coating for Stainless Steel. ACS Appl Mater Interfaces. 2013 Apr 10;5(7):2549–54.

2. Ferrari M, Benedetti A. Superhydrophobic surfaces for applications in seawater. Adv Colloid Interface Sci. 2015 Aug;222:291–304.

3. Fürstner R, Barthlott W, Neinhuis C, Walzel P,. Wetting and self-cleaning properties of artificial superhydrophobic surfaces. Langmuir. 2005;21(3):956–61.

4. Calvin K, Dasgupta D, Krinner G, Mukherji A, Thorne PW, Trisos C, et al. IPCC, 2023: Climate Change 2023: Synthesis Report. Contribution of Working Groups I, II and III to the Sixth Assessment Report of the Intergovernmental Panel on Climate Change [Core Writing Team, H. Lee and J. Romero (eds.)]. IPCC, Geneva, Switzerland. [Internet]. Arias P, Bustamante M, Elgizouli I, Flato G, Howden M, Méndez-Vallejo C, et al., editors. 2023 Jul. Available from: https://www.ipcc.ch/report/ar6/syr/

5. Barthlott W, Neinhuis C. Purity of the sacred lotus, or escape from contamination in biological surfaces. Planta. 1997;202:1–8.

6. Koch K, Bhushan B,, Barthlott W,. Diversity of structure, morphology and wetting of plant surfaces. Soft Matter. 2008;4(10):1943–63.

7. Park YB, Im H, Im M, Choi YK. Self-cleaning effect of highly water-repellent microshell structures for solar cell applications. J Mater Chem. 2011;21(3):633–6.

8. Liang Z, Zhou Z, Zhao L, Dong B, Wang S. Fabrication of transparent, durable and self-cleaning superhydrophobic coatings for solar cells. New Journal of Chemistry. 2020;44(34):14481–9.

9. Callow ME,, Callow JA,. Marine biofouling: a sticky problem. Biologist. 2002;49(1):1–5.

10. Schultz MP, Bendick JA, Holm ER, Hertel WM. Economic impact of biofouling on a naval surface ship. Biofouling. 2011 Jan 14;27(1):87–98.

11. Liu S, Kee YH, Shang B, Papanikolaou A. Assessment of the economic, environmental and safety impact of biofouling on a ship’s hull and propeller. Ocean Engineering. 2023 Oct;285:115481.

12. UNCTAD. Review of Maritime Transport 2023. 2023.

13. Pei X, Ye Q. Development of Marine Antifouling Coatings. In: Antifouling Surfaces and Materials. Berlin, Heidelberg: Springer Berlin Heidelberg; 2015. p. 135–49.

14. Ciriminna R, Bright F V., Pagliaro M. Ecofriendly Antifouling Marine Coatings. ACS Sustain Chem Eng. 2015 Apr 6;3(4):559–65.

15. Baier RE. Surface behaviour of biomaterials: The theta surface for biocompatibility. J Mater Sci Mater Med. 2006 Nov 22;17(11):1057–62.

16. Botta G, Cavaliere M, Holttinen H,. Ice accretion at acqua spruzza and its effects on wind turbine operation and loss of energy production. BOREAS IV. 1998;31:77–86.

17. Frohboese P, Anders A. Effects of Icing on Wind Turbine Fatigue Loads. J Phys Conf Ser. 2007 Jul 1;75:012061.

18. Dalili N, Edrisy A, Carriveau R. A review of surface engineering issues critical to wind turbine performance. Renewable and Sustainable Energy Reviews. 2009 Feb;13(2):428–38.

19. Huang W, Huang J, Guo Z, Liu W. Icephobic/anti-icing properties of superhydrophobic surfaces. Adv Colloid Interface Sci. 2022 Jun;304:102658.

20. Li W, Zhan Y, Yu S. Applications of superhydrophobic coatings in anti-icing: Theory, mechanisms, impact factors, challenges and perspectives. Prog Org Coat. 2021 Mar;152:106117.

21. Tourkine P, Le Merrer M, Quéré D. Delayed Freezing on Water Repellent Materials. Langmuir. 2009 Jul 7;25(13):7214–6.

22. Varanasi KK, Deng T, Smith JD, Hsu M, Bhate N. Frost formation and ice adhesion on superhydrophobic surfaces. Appl Phys Lett. 2010 Dec 6;97(23).

23. Lin Y, Chen H, Wang G, Liu A. Recent Progress in Preparation and Anti-Icing Applications of Superhydrophobic Coatings. Coatings. 2018 May 31;8(6):208.

24. Farhadi S, Farzaneh M, Kulinich SA. Anti-icing performance of superhydrophobic surfaces. Appl Surf Sci. 2011 May;257(14):6264–9.

25. Young T,. An essay on the cohesion of fluids. Philos Trans R Soc Lond. 1805;95:65–87.

26. Yuan Y, Lee TR. Contact angle and wetting properties. Springer Series in Surface Sciences. 2013;51(1):3–34.

27. Feng L, Zhang Y, Xi J, Zhu Y, Wang N, Xia F, et al. Petal Effect: A Superhydrophobic State with High Adhesive Force. Langmuir. 2008 Apr 1;24(8):4114–9.

28. Byun D, Hong J, Ko JH, Lee YJ, Park HC, Byun BK, et al. Wetting characteristics of insect wing surfaces. J Bionic Eng. 2009;6(1):63–70.

29. Bell MS, Shahraz A, Fichthorn KA, Borhan A. Effects of Hierarchical Surface Roughness on Droplet Contact Angle. Langmuir. 2015 Jun 23;31(24):6752–62.

30. Nakae H, Yoshida M, Yokota M. Effects of roughness pitch of surfaces on their wettability. J Mater Sci. 2005 May;40(9–10):2287–93.

31. Gong G, Wu J, Jin X, Jiang L. Adhesion Tuning at Superhydrophobic States: From Petal Effect to Lotus Effect. Macromol Mater Eng. 2015 Nov 26;300(11):1057–62.

32. Bico J, Thiele U, Quéré D. Wetting of textured surfaces. Colloids Surf A Physicochem Eng Asp. 2002 Jul;206(1–3):41–6.

33. Bhushan B, Jung YC. Wetting, adhesion and friction of superhydrophobic and hydrophilic leaves and fabricated micro/nanopatterned surfaces. Journal of Physics: Condensed Matter. 2008 Jun 4;20(22):225010.

34. Wenzel RN. RESISTANCE OF SOLID SURFACES TO WETTING BY WATER. Ind Eng Chem. 1936 Aug 1;28(8):988–94.

35. Cassie ABD, Baxter S,. Wettability of porous surfaces. Transactions of the Faraday Society. 1944;40:546–51.

36. Lafuma A, Quéré D. Superhydrophobic states. Nat Mater. 2003 Jul 1;2(7):457–60.

37. Papadopoulous p. , Mammen L, Deng X, Vollmer D,, Butt HJ,. How superhydrophobicty breaks down. Proceedings of the National Academy of Sciences. 2013;110(9):3254–8.

38. Schellenberger F, Encinas N, Vollmer D, Butt HJ. How Water Advances on Superhydrophobic Surfaces. Phys Rev Lett. 2016 Feb 29;116(9):096101.

39. Feng XQ, Gao X, Wu Z, Jiang L, Zheng QS,. Superior water repellency of water strider legs with hierarchical structures: experiments and analysis. Langmuir. 2007;23(9):4892–6.

40. Zhang X, Shi F, Niu J, Jiang Y, Wang Z. Superhydrophobic surfaces: from structural control to functional application. J Mater Chem. 2008;18(6):621–33.

41. Drelich JW, Boinovich L, Chibowski E, Della Volpe C, Hołysz L, Marmur A, et al. Contact angles: history of over 200 years of open questions. Surf Innov. 2020 Feb 1;8(1–2):3–27.

42. Marmur A, Della Volpe C, Siboni S, Amirfazli A, Drelich JW. Contact angles and wettability: towards common and accurate terminology. Surf Innov. 2017 Mar;5(1):3–8.

43. Roth-Nebelsick A, Konrad W, Ebner M, Miranda T, Thielen S, Nebelsick JH. When rain collides with plants—patterns and forces of drop impact and how leaves respond to them. J Exp Bot. 2022 Feb 24;73(4):1155–75.

44. de Gennes PG. Wetting: statics and dynamics. Rev Mod Phys. 1985 Jul 1;57(3):827–63.

45. Hsu SH, Woan K, Sigmund W. Biologically inspired hairy structures for superhydrophobicity. Materials Science and Engineering: R: Reports. 2011 Oct;72(10):189–201.

46. Extrand CW, Gent AN. Retention of liquid drops by solid surfaces. J Colloid Interface Sci. 1990 Sep;138(2):431–42.

47. Li J, Zhou Y, Wang W, Xu C, Ren L. Superhydrophobic Copper Surface Textured by Laser for Delayed Icing Phenomenon. Langmuir. 2020 Feb 11;36(5):1075–82.

48. Fang Y, Jin D, Wang J, Hou Y, Dong F. Directional Wettability of Butterfly Wing and Biomimetic Preparation of Superhydrophobic Polymer Film by Soft Lithography. 2017.

49. Verho T, Bower C, Andrew P, Franssila S, Ikkala O, Ras RH,. Mechanically durable superhydrophobic surfaces. Advanced Materials. 2011;25(5):673–8.

50. Malavasi I, Bernagozzi I, Antonini C, Marengo M. Assessing durability of superhydrophobic surfaces. Surf Innov. 2015 Mar;3(1):49–60.

51. Cohen N, Dotan A, Dodiuk H, Kenig S. Superhydrophobic Coatings and Their Durability. Materials and Manufacturing Processes. 2016 Jul 3;31(9):1143–55.

52. Soto D, De Larivière AB, Boutillon X, Clanet C, Quéré D. The force of impacting rain. Soft Matter. 2014;10(27):4929–34.

53. Groten J, Rühe J,. Surfaces with combined microscale and nanoscale structures: a route to mechanically stable superhydrophobic surfaces?. Langmuir. 2013;29(11):3765–72.

54. Huet OD, Massinon M, De Cock N, Forster WA, Zabkiewicz JA, Pethiyagoda R, et al. Image analysis of shatter and pinning events on hard-to-wet leaf surfaces by drops containing surfactant. Pest Manag Sci. 2020 Oct 3;76(10):3477–86.

55. Dorr GJ, Wang S, Mayo LC, McCue SW, Forster WA, Hanan J, et al. Impaction of spray droplets on leaves: influence of formulation and leaf character on shatter, bounce and adhesion. 2015 Jun 13; Available from: http://arxiv.org/abs/1506.04258

56. Erkal A, D'Ayala D, Sequeira L. Assessment of wind-driven rain impact, related surface erosion and surface strength reduction of historic building materials. Build Environ. 2012 Nov;57:336–48.

57. Laan N, de Bruin KG, Bartolo D, Josserand C, Bonn D. Maximum Diameter of Impacting Liquid Droplets. Phys Rev Appl. 2014 Oct 30;2(4):044018.

58. Luiset B, Sanchette F, Billard A, Schuster D. Mechanisms of stainless steels erosion by water droplets. Wear. 2013 Jun;303(1–2):459–64.

59. Udawattha CD, Galkanda GAHH, Halwatura RU. A Study on Natural Rain Surface Erosion of Different Walling Materials in Tropics. In: 2018 Moratuwa Engineering Research Conference (MERCon). IEEE; 2018. p. 84–9.

60. Wang W, Shen A, He Z, Guo Y, Li D. Mechanism and erosion resistance of internally cured concrete including super absorbent polymers against coupled effects of acid rain and fatigue load. Constr Build Mater. 2021 Jul;290:123252.

61. Wang Y, Niu D, Song Z. Effect of acid rain erosion on steel fiber reinforced concrete. Journal of Wuhan University of Technology-Mater Sci Ed. 2017 Feb 12;32(1):121–8.

62. Klein NS, Bachmann J, Aguado A, Toralles-Carbonari B. Evaluation of the wettability of mortar component granular materials through contact angle measurements. Cem Concr Res. 2012 Dec;42(12):1611–20.

63. Josserand C, Thoroddsen ST. Drop Impact on a Solid Surface. Vol. 48, Annual Review of Fluid Mechanics. Annual Reviews Inc.; 2016. p. 365–91.

64. Popinet S. An accurate adaptive solver for surface-tension-driven interfacial flows. J Comput Phys. 2009 Sep;228(16):5838–66.

65. Scardovelli R, Zaleski S. Direct numerical simulation of free-surface and interfacial flow. Annu Rev Fluid Mech. 1999;31(1):567–603.

66. Gunjal PR, Ranade V V., Chaudhari R V. Dynamics of drop impact on solid surface: Experiments and VOF simulations. AIChE Journal. 2005 Jan 9;51(1):59–78.

67. Cheng X, Sun TP, Gordillo L. Drop Impact Dynamics: Impact Force and Stress Distributions. Annu Rev Fluid Mech. 2022 Jan 5;54(1):57–81.

68. Serio MA, Carollo FG, Ferro V. Raindrop size distribution and terminal velocity for rainfall erosivity studies. A review. J Hydrol (Amst). 2019 Sep;576:210–28.

69. Frohn A,, Roth N,. Dynamics of droplets. Springer Science & Business Media.; 2000.

70. Richard D, Clanet C, Quéré D. Contact time of a bouncing drop. Nature. 2002 Jun;417(6891):811–811.

71. Bird JC, Dhiman R, Kwon HM, Varanasi KK. Reducing the contact time of a bouncing drop. Nature. 2013;503(7476):385–8.

72. Gordillo L, Sun TP, Cheng X. Dynamics of drop impact on solid surfaces: evolution of impact force and self-similar spreading. J Fluid Mech. 2018 Apr 10;840:190–214.

73. Sun TP, Álvarez-Novoa F, Andrade K, Gutiérrez P, Gordillo L, Cheng X. Stress distribution and surface shock wave of drop impact. Nat Commun. 2022 Mar 31;13(1):1703.

74. Kirols HS, Kevorkov D, Uihlein A, Medraj M. The effect of initial surface roughness on water droplet erosion behaviour. Wear. 2015 Nov;342–343:198–209.

75. Hyväluoma J, Timonen J. Impalement transitions in droplets impacting microstructured superhydrophobic surfaces. EPL (Europhysics Letters). 2008 Sep;83(6):64002.

76. Nouhou Bako A, Darboux F, James F, Josserand C, Lucas C. Pressure and shear stress caused by raindrop impact at the soil surface: Scaling laws depending on the water depth. Earth Surf Process Landf. 2016 Jul 11;41(9):1199–210.

77. Neinhuis C, Koch K,, Barthlott W,. Movement and regeneration of epicuticular waxes through plant cuticles. Planta. 2001;213(3):427–34.

78. Koch K, Bhushan B, Ensikat HJ, Barthlott W,. Self-healing of voids in the wax coating on plant surfaces. Philosophical Transactions of the Royal Society A: Mathematical, Physical and Engineering Sciences. 2009;367(1894):1673–88.

79. Xiang S, Liu W. Self-Healing Superhydrophobic Surfaces: Healing Principles and Applications. Adv Mater Interfaces. 2021 Jun 24;8(12).

80. Zhou H, Niu H, Wang H, Lin T. Self-Healing Superwetting Surfaces, Their Fabrications, and Properties. Chem Rev. 2023 Jan 25;123(2):663–700.

81. Lauderbaugh LK, Ginebra-Solanellas RM, Holder CD, Webb R,. A biomechanical model of leaf inclination angle oscillations after raindrop impact. Environ Exp Bot. 2021;190:104586.

82. Gart S, Mates JE, Megaridis CM, Jung S,. Droplet impacting a cantilever: A leaf-raindrop system. Phys Rev Appl. 2015;3(4):044019.

83. Weisensee PB, Tian J, Miljkovic N, King WP,. Water droplet impact on elastic superhydrophobic surfaces. Sci Rep. 2016;6(1):30328.

84. Bhosale Y, Esmaili E, Bhar K, Jung S. Bending, twisting and flapping leaf upon raindrop impact. Bioinspir Biomim. 2020 Mar 6;15(3):036007.

85. Holder CD, Lauderbaugh LK, Ginebra-Solanellas RM, Webb R. Changes in leaf inclination angle as an indicator of progression toward leaf surface storage during the rainfall interception process. J Hydrol (Amst). 2020 Sep;588:125070.

86. Ginebra-Solanellas RM, Holder CD, Lauderbaugh LK, Webb R,. The influence of changes in leaf inclination angle and leaf traits during the rainfall interception process. Agric For Meteorol. 2020;285:107924.

87. Méndez-Alonzo R, Ewers FW, Sack L. Ecological variation in leaf biomechanics and its scaling with tissue structure across three mediterranean-climate plant communities. Funct Ecol. 2013 Apr 28;27(2):544–54.

88. Mountcastle AM, Combes SA,. Biomechanical strategies for mitigating collision damage in insect wings: structural design versus embedded elastic materials. . Journal of Experimental Biology,. 2014;217(7):1108–15.

89. Mountcastle AM, Helbling EF, Wood RJ,. An insect-inspired collapsible wing hinge dampens collision-induced body rotation rates in a microrobot. . J R Soc Interface. 2019;15(150):20180618.

90. Foster DJ, Cartar RV,. What causes wing wear in foraging bumble bees?. . Journal of Experimental Biology,. 2011;214:1896–901.

91. Dickerson AK, Hu DL. Mosquitoes Actively Remove Drops Deposited by Fog and Dew. Integr Comp Biol. 2014 Dec 1;54(6):1008–13.

92. Dickerson AK, Shankles PG, Hu DL. Raindrops push and splash flying insects. Physics of Fluids. 2014 Feb 1;26(2).

93. Dickerson AK, Shankles P. G., Madhavan NM,, Hu DL. Mosquitoes survive raindrop collisions by virtue of their low mass,. Proceedings of the National Academy of Sciences . 2012;109(25):9822–7.

94. Kim H, Lee C, Kim MH, Kim J. Drop impact characteristics and structure effects of hydrophobic surfaces with micro-and/or nanoscaled structures. Langmuir. 2012;28(30):11250–7.

95. Kim S, Wu Z, Esmaili E, Dombroskie JJ, Jung S. How a raindrop gets shattered on biological surfaces. Proceedings of the National Academy of Sciences. 2020 Jun 23;117(25):13901–7.

96. Yarin AL. DROP IMPACT DYNAMICS: Splashing, Spreading, Receding, Bouncing…. Annu Rev Fluid Mech. 2006 Jan 1;38(1):159–92.

97. Quintero ES, Riboux G, Gordillo JM,. Splashing of droplets impacting superhydrophobic substrates. J Fluid Mech. 2019;870:175–88.

98. Papierowska E, Beczek M, Mazur R, Szatyłowicz J, Szewińska J, Polakowski C, et al. Study of drop impact dynamics on the hydrophobic leaf surface of an aquatic plant–Pistia stratiotes case study. J Exp Bot. 2023;74(17):5255–72.

99. Zhang B, Sanjay V, Shi S, Zhao Y, Lv C, Feng XQ, et al. Impact forces of water drops falling on superhydrophobic surfaces. Phys Rev Lett. 2022;129(10):104501.

100. Hao J,. Effect of surface roughness on droplet splashing. Physics of Fluids. 2017;29(12).

101. Bartolo D, Bouamrirene F, Verneuil É, Buguin A, Silberzan P, Moulinet S. Bouncing or sticky droplets: Impalement transitions on superhydrophobic micropatterned surfaces. Europhys Lett. 2006 Apr 15;74(2):299–305.

102. de Goede T, de Bruin K, Shahidzadeh N, Bonn D,. Droplet splashing on rough surfaces. Phys Rev Fluids. 2021;6(4):043604.

103. Howland CJ, Antkowiak A, Castrejón-Pita JR, Howison SD, Oliver JM, Style RW, et al. It's Harder to Splash on Soft Solids. Phys Rev Lett. 2016 Oct 26;117(18):184502.

104. Goldstein PZ. Diversity and Significance of Lepidoptera: A Phylogenetic Perspective. In: Insect Biodiversity. Wiley; 2017. p. 463–95.

105. Sun G, Fang Y. The Relationship between Superhydrophobicity, Self-Cleaning Performance and Microstructure of Moth Wing. In: Proceedings of the 2015 International Conference on Advanced Engineering Materials and Technology. Paris, France: Atlantis Press; 2015. p. 9–12.

106. Shen Z, Neil TR, Robert D, Drinkwater BW, Holderied MW,. Biomechanics of a moth scale at ultrasonic frequencies. Proceedings of the National Academy of Sciences. 2018;115(48):12200–5.

107. Ghiradella H. Structure of butterfly scales: Patterning in an insect cuticle. Microsc Res Tech. 1994 Apr 4;27(5):429–38.

108. Vukusic P,. Structural colour in Lepidoptera. Current Biology. 2006;16(16):R621–3.

109. Liao G, Zuo H, Cao Y, Shi T. Optical properties of the micro/nano structures of Morpho butterfly wing scales. Science in China Series E: Technological Sciences. 2010 Jan 28;53(1):175–81.

110. Kinoshita S, Yoshioka S, Kawagoe K. Mechanisms of structural colour in the *Morpho* butterfly: cooperation of regularity and irregularity in an iridescent scale. Proc R Soc Lond B Biol Sci. 2002 Jul 22;269(1499):1417–21.

111. Doucet SM, Meadows MG. Iridescence: a functional perspective. J R Soc Interface. 2009 Apr 6;6(suppl_2).

112. Bálint Z, Kertész K, Piszter G, Vértesy Z, Biró LP. The well-tuned blues: the role of structural colours as optical signals in the species recognition of a local butterfly fauna (Lepidoptera: Lycaenidae: Polyommatinae). J R Soc Interface. 2012 Aug 7;9(73):1745–56.

113. Neil TR, Shen Z, Robert D, Drinkwater BW, Holderied MW,. Moth wings as sound absorber metasurface. Proceedings of the Royal Society A: Mathematical, Physical and Engineering Sciences. 2022;478(2262):20220046.

114. Neil TR, Shen Z, Robert D, Drinkwater BW, Holderied MW. Moth wings are acoustic metamaterials. Proceedings of the National Academy of Sciences. 2020 Dec 8;117(49):31134–41.

115. Fang Y,, Sun G,. Complex wettability and self-cleaning performance of butterfly wing surface. In: Applied Mechanics and Materials. Trans Tech publications Ltd.; 2015. p. 943–7.

116. Sun G,, Fang Y,. Low adhesive superhydrophobicity and self-cleaning property of moth wing. Vol. 1089. Trans Tech publications Ltd.; 2015. 194–197 p.

117. Fang Y, Sun G, Yin J, Wang W, Wang Y. Ultrastructure and Self-Cleaning Function of Moth (Notodontidae) and Butterfly (Lycaenidae) Wings. In: Proceedings of the 2nd International Conference on Biomedical and Biological Engineering 2017 (BBE 2017). Paris, France: Atlantis Press; 2017. p. 440–6.

118. Zheng Y, Gao X, Jiang L. Directional adhesion of superhydrophobic butterfly wings. Soft Matter. 2007;3(2):178–82.

119. Sun G, Fang Y. Anisotropic Characteristic of Insect (Lepidoptera) wing Surfaces. In 2015.

120. Zhao H,, Law KY,. Directional self-cleaning superoleophobic surface. Langmuir. 2012;28(32):11812–8.

121. Chamakos NT, Karapetsas G,, Papathanasiou AG,. How asymmetric surfaces induce directional droplet motion. Colloids Surf A Physicochem Eng Asp. 2016;511:180–9.

122. Yoshimitsu Z, Nakajima A, Watanabe T,, Hashimoto K,. Effects of surface structure on the hydrophobicity and sliding behavior of water droplets. Langmuir. 2022;18(15):5818–22.

123. Lv C, Yang C, Hao P, He F, Zheng Q. Sliding of Water Droplets on Microstructured Hydrophobic Surfaces. Langmuir. 2010 Jun 1;26(11):8704–8.

124. Sheng X, Zhang J. Directional motion of water drop on ratchet-like superhydrophobic surfaces. Appl Surf Sci. 2011 May;257(15):6811–6.

125. Wagner T, Neinhuis C,, Barthlott W,. Wettability and contaminability of insect wings as a function of their surface sculptures. Acta Zoologica . 1996;77(3):213–25.

126. LEATHER SR, BASSET Y, HAWKINS BA. Insect conservation: finding the way forward. Insect Conserv Divers. 2008 Feb;1(1):67–9.

127. Kawahara AY, Breinholt JW. Phylogenomics provides strong evidence for relationships of butterflies and moths. Proceedings of the Royal Society B: Biological Sciences. 2014 Aug 7;281(1788):20140970.

128. Neil TR, Kennedy EE, Harris BJ, Holderied MW,. Wingtip folds and ripples on saturniid moths create decoy echoes against bat biosonar. Current Biology. 2021;31(21):4824–30.

129. Rajabi H, Dirks JH, Gorb SN. Insect wing damage: causes, consequences and compensatory mechanisms. Journal of Experimental Biology. 2020 May 1;223(9).

130. Mountcastle AM, Combes SA. Wing flexibility enhances load-lifting capacity in bumblebees. Proceedings of the Royal Society B: Biological Sciences. 2013 May 22;280(1759):20130531.

131. Neil TR, Shen Z, Robert D, Drinkwater BW, Holderied MW. Moth wings as sound absorber metasurface. Proceedings of the Royal Society A: Mathematical, Physical and Engineering Sciences. 2022 Jun 15;478(2262).

132. Neil TR, Shen Z, Robert D, Drinkwater BW, Holderied MW. Thoracic scales of moths as a stealth coating against bat biosonar. J R Soc Interface. 2020 Feb 26;17(163):20190692.

133. Sharplin J. Wing Base Structure in Lepidoptera: III. Taxonomic Characters. Can Entomol. 1964 Jul 31;96(7):943–9.

134. Shirtcliffe NJ, McHale G, Newton MI,. Learning from superhydrophobic plants: The use of hydrophilic areas on superhydrophobic surfaces for droplet control. Langmuir. 2009;25(24):14121–8.

135. Bauer U, Scharmann M, Skepper J, Federle W,. 'Insect aquaplaning' on a superhydrophilic hairy surface: how Heliamphora nutans Benth. pitcher plants capture prey. . Proceedings of the Royal Society B: Biological Sciences. 2013;280(1753):20122569.

136. Dunkerley D. Leaf water shedding: Moving away from assessments based on static contact angles, and a new device for observing dynamic droplet roll-off behaviour. Methods Ecol Evol. 2023 Dec 15;14(12):3047–54.

137. Hsu SH, Woan K, Sigmund W,. Biologically inspired hairy structures for superhydrophobicity. Materials Science and Engineering: R: Reports. 2011;72(19):189–201.

138. Ditsche P, Gorb E, Mayser M, Gorb S, Schimmel T, Barthlott W,. Elasticity of the hair cover in air-retaining Salvinia surfaces. Applied Physics A. 2015;121:505–11.

139. Konrad W, Roth-Nebelsick A, Kessel B, Miranda T, Ebner M, Schott R, et al. The impact of raindrops on Salvinia molesta leaves: effects of trichomes and elasticity. J R Soc Interface. 2021;18(185):20210676.

140. Brewer CA, Smith WK, Vogelmann TC. Functional interaction between leaf trichomes, leaf wettability and the optical properties of water droplets. Plant Cell Environ. 1991 Dec 28;14(9):955–62.

141. Motamedi M, Warkiani ME, Taylor RA. Transparent Surfaces Inspired by Nature. Adv Opt Mater. 2018 Jul 9;6(14).

142. Boden SA, Bagnall DM. Sunrise to sunset optimization of thin film antireflective coatings for encapsulated, planar silicon solar cells. Progress in Photovoltaics: Research and Applications. 2009 Jun 13;17(4):241–52.

143. Husain AAF, Hasan WZW, Shafie S, Hamidon MN, Pandey SS. A review of transparent solar photovoltaic technologies. Renewable and Sustainable Energy Reviews. 2018 Oct;94:779–91.

144. Binetti VR, Schiffman JD, Leaffer OD, Spanier JE, Schauer CL. The natural transparency and piezoelectric response of the Greta oto butterfly wing. Integrative Biology. 2009;1(4):324–9.

145. Perez Goodwyn P, Maezono Y, Hosoda N, Fujisaki K. Waterproof and translucent wings at the same time: Problems and solutions in butterflies. Naturwissenschaften. 2009 Jul;96(7):781–7.

146. Gomez D, Pinna C, Pairraire J, Arias M, Barbut J, Pomerantz A, et al. Wing transparency in butterflies and moths: structural diversity, optical properties, and ecological relevance. Ecol Monogr. 2021 Nov 17;91(4).

147. Hernández-Chavarría F, Hernández A, Sittenfeld A. The" windows", scales, and bristles of the tropical moth Rothschildia lebeau (Lepidoptera: Saturniidae). Revista de biología tropical. 2004;52(4):919–26.

148. Papadopoulos P, Mammen L, Deng X, Vollmer D, Butt HJ. How superhydrophobicity breaks down. Proceedings of the National Academy of Sciences. 2013 Feb 26;110(9):3254–8.

149. Staicopolus DN. The computation of surface tension and of contact angle by the sessile-drop method. J Colloid Sci. 1962 Jun;17(5):439–47.

150. Drelich J. Guidelines to measurements of reproducible contact angles using a sessile-drop technique. Surf Innov. 2013 Dec;1(4):248–54.

151. Long J, Fan P, Jiang D, Han J, Lin Y, Cai M, et al. Anisotropic sliding of water droplets on the superhydrophobic surfaces with anisotropic groove-like micro/nano structures. Adv Mater Interfaces. 2016;3(24):1600641.

152. Webb HK, Crawford RJ,, Ivanova EP. Wettability of natural superhydrophobic surface. Adv Colloid Interface Sci. 2014;210:58–64.

153. Jiang Y, Choi CH. Droplet Retention on Superhydrophobic Surfaces: A Critical Review. Vol. 8, Advanced Materials Interfaces. Wiley-VCH Verlag; 2021.

154. Akbari R, Antonini C. Contact angle measurements: From existing methods to an open-source tool. Adv Colloid Interface Sci. 2021 Aug;294:102470.

155. Kabir H, Garg N. Machine learning enabled orthogonal camera goniometry for accurate and robust contact angle measurements. Sci Rep. 2023 Jan 27;13(1):1497.

156. Extrand CW, Moon SI. Contact Angles of Liquid Drops on Super Hydrophobic Surfaces: Understanding the Role of Flattening of Drops by Gravity. Langmuir. 2010 Nov 16;26(22):17090–9.

157. Matos IS, Rosado BHP. Retain or repel? Droplet volume does matter when measuring leaf wetness traits. Ann Bot. 2016 May;117(6):1045–52.

158. Huhtamäki T, Tian X, Korhonen JT, Ras RHA. Surface-wetting characterization using contact-angle measurements. Nat Protoc. 2018 Jul 9;13(7):1521–38.

159. Wu D, Wang JN, Wu SZ, Chen QD, Zhao S, Zhang H, et al. Three-level biomimetic rice-leaf surfaces with controllable anisotropic sliding. Adv Funct Mater. 2011;21(15):2927–32.

160. Bixler GD,, Bhushan B. Rice- and butterfly-wing effect inspired self-cleaning and low drag micro/nanopatterned surfaces in water, oil and air flow. Nanoscale. 2014;6(1):76–96.

161. Berardi U, Iannace G. Acoustic characterization of natural fibers for sound absorption applications. Build Environ. 2015;94:840–52.

162. Arenas JP,, Crocker MJ,. Recent trends in porous sound-absorbing materials. Sound & Vibration. 2010;44(7):12–8.

163. Tarnogrodzki A,. Theoretical prediction of the critical Weber number. International journal of multiphase flow. 1993;19(2):329–36.

164. Richard D, Quéré D,. Bouncing water drops. Europhys Lett. 2000;50(6):769.

165. Kim H, Park U, Lee C, Kim H, Hwan Kim M, Kim J. Drop splashing on a rough surface: How surface morphology affects splashing threshold. Appl Phys Lett. 2014 Apr 21;104(16).

166. Kim S, Wu Z, Esmaili E, Dombroskie JJ,, Jung S,. How a raindrop gets shattered on biological surfaces. PNAS. 2020;117(25):13901–7.

167. Zhang H, Zhang X, Yi X, He F, Niu F, Hao P,. Effect of wettability on droplet impact: Spreading and splashing. Exp Therm Fluid Sci. 2021;124:110369.

168. Lv C, Hao P, Zhang X, He F. Drop impact upon superhydrophobic surfaces with regular and hierarchical roughness. Appl Phys Lett. 2016 Apr 4;108(14).

169. Aboud DG, Kietzig AM,. Splashing threshold of oblique droplet impacts on surfaces of various wettability. Langmuir. 2015;31(36):10100–11.

170. Yokoi K. Numerical studies of droplet splashing on a dry surface: triggering a splash with the dynamic contact angle. Soft Matter. 2011;7(11):5120–3.

171. Chen H, Zhang X, Garcia BD, Georgoulas A, Deflorin M, Liu Q, et al. DROP IMPACT ONTO A CANTILEVER BEAM: BEHAVIOR OF THE LAMELLA AND FORCE MEASUREMENT. Interfacial Phenom Heat Transf. 2019;7(1):85–96.

172. Li J, Zhang B, Guo P, Lv Q. Impact force of a low speed water droplet colliding on a solid surface. J Appl Phys. 2014 Dec 7;116(21).

173. Mitchell BR, Klewicki JC, Korkolis YP, Kinsey BL. The transient force profile of low-speed droplet impact: measurements and model. J Fluid Mech. 2019 May 25;867:300–22.

174. Imeson AC, Vis R, de Water E. The measurement of water-drop impact forces with a piezo-electric transducer. Catena (Amst). 1981 Jan;8(1):83–96.

175. Philippi J, Lagrée PY, Antkowiak A. Drop impact on a solid surface: short-time self-similarity. J Fluid Mech. 2016 May 25;795:96–135.

176. Riboux G, Gordillo JM. Experiments of Drops Impacting a Smooth Solid Surface: A Model of the Critical Impact Speed for Drop Splashing. Phys Rev Lett. 2014 Jul 11;113(2):024507.

177. Liu Q, Lo JHY, Li Y, Liu Y, Zhao J, Xu L. The role of drop shape in impact and splash. Nat Commun. 2021 May 24;12(1):3068.

178. Sun TP, Álvarez-Novoa F, Andrade K, Gutiérrez P, Gordillo L, Cheng X. Stress distribution and surface shock wave of drop impact. Nat Commun. 2022 Mar 31;13(1):1703.

179. Cimpeanu R, Papageorgiou DT. Three-dimensional high speed drop impact onto solid surfaces at arbitrary angles. International Journal of Multiphase Flow. 2018 Oct;107:192–207.

180. Tang C, Qin M, Weng X, Zhang X, Zhang P, Li J, et al. Dynamics of droplet impact on solid surface with different roughness. International Journal of Multiphase Flow. 2017 Nov;96:56–69.

181. Rioboo R, Tropea C, Marengo M. OUTCOMES FROM A DROP IMPACT ON SOLID SURFACES. Atomization and Sprays. 2001;11(2):12.

182. Cheng X, Sun TP, Gordillo L. Drop Impact Dynamics: Impact Force and Stress Distributions. Annu Rev Fluid Mech. 2022 Jan 5;54(1):57–81.

183. Aguilar-Morales AI, Alamri S, Voisiat B, Kunze T, Lasagni AF. The Role of the Surface Nano-Roughness on the Wettability Performance of Microstructured Metallic Surface Using Direct Laser Interference Patterning. Materials. 2019 Aug 27;12(17):2737.

184. Pugh K, Nash JW, Reaburn G, Stack MM. On analytical tools for assessing the raindrop erosion of wind turbine blades. Renewable and Sustainable Energy Reviews. 2021 Mar;137:110611.

185. Vangi D. Structural behavior of the vehicle during the impact. In: Vehicle Collision Dynamics. Elsevier; 2020. p. 1–27.

186. Wu JZ, Pan CS, Ronaghi M, Wimer BM, Reischl U. Application of polyethylene air-bubble cushions to improve the shock absorption performance of Type I construction helmets for repeated impacts. Biomed Mater Eng. 2021 Jan 21;32(1):1–14.

187. Wu JZ, Pan CS, Ronaghi M, Wimer BM, Reischl U. Application of air-bubble cushioning to improve the shock absorption performance of type I industrial helmets. Eng Fail Anal. 2020 Nov;117:104921.

188. Reiner M. Elasticity Beyond the Elastic Limit. American Journal of Mathematics. 1948 Apr;70(2):433.

189. Lee S, Park JS, Lee TR. The Wettability of Fluoropolymer Surfaces: Influence of Surface Dipoles. Langmuir. 2008 May 1;24(9):4817–26.

190. Nilsson MA, Daniello RJ, Rothstein JP. A novel and inexpensive technique for creating superhydrophobic surfaces using Teflon and sandpaper. J Phys D Appl Phys. 2010 Feb 3;43(4):045301.

191. Vazirinasab E, Maghsoudi K, Jafari R, Momen G. A comparative study of the icephobic and self-cleaning properties of Teflon materials having different surface morphologies. J Mater Process Technol. 2020 Feb;276:116415.

192. Lojen D, Zaplotnik R, Primc G, Mozetič M, Vesel A. Optimization of surface wettability of polytetrafluoroethylene (PTFE) by precise dosing of oxygen atoms. Appl Surf Sci. 2022 Oct;598:153817.

193. Goswami S, Klaus S, Benziger J. Wetting and Absorption of Water Drops on Nafion Films. Langmuir. 2008 Aug 1;24(16):8627–33.

194. Grundke K, Pöschel K, Synytska A, Frenzel R, Drechsler A, Nitschke M, et al. Experimental studies of contact angle hysteresis phenomena on polymer surfaces — Toward the understanding and control of wettability for different applications. Adv Colloid Interface Sci. 2015 Aug;222:350–76.

195. Scarratt LRJ, Hoatson BS, Wood ES, Hawkett BS, Neto C. Durable Superhydrophobic Surfaces via Spontaneous Wrinkling of Teflon AF. ACS Appl Mater Interfaces. 2016 Mar 16;8(10):6743–50.

196. Sedev R, Fabretto M, Ralston J. WETTABILITY AND SURFACE ENERGETICS OF ROUGH FLUOROPOLYMER SURFACES. J Adhes. 2004 Jun 10;80(6):497–520.

197. Stanton MM, Ducker RE, MacDonald JC, Lambert CR, Grant McGimpsey W. Super-hydrophobic, highly adhesive, polydimethylsiloxane (PDMS) surfaces. J Colloid Interface Sci. 2012 Feb;367(1):502–8.

198. Wong WSY, Hauer L, Naga A, Kaltbeitzel A, Baumli P, Berger R, et al. Adaptive Wetting of Polydimethylsiloxane. Langmuir. 2020 Jul 7;36(26):7236–45.

199. Khorasani MT, Mirzadeh H, Kermani Z. Wettability of porous polydimethylsiloxane surface: morphology study. Appl Surf Sci. 2005 Apr;242(3–4):339–45.

200. Ziya Özek H. Silicone-based water repellents. In: Waterproof and Water Repellent Textiles and Clothing. Elsevier; 2018. p. 153–89.

201. Smith JE, Gillham RW. Effects of solute concentration–dependent surface tension on unsaturated flow: Laboratory sand column experiments. Water Resour Res. 1999 Apr;35(4):973–82.

202. Docoslis A, Giese RF, van Oss CJ. Influence of the water–air interface on the apparent surface tension of aqueous solutions of hydrophilic solutes. Colloids Surf B Biointerfaces. 2000 Dec;19(2):147–62.

203. Hsin W, Sheng YJ, Lin SY, Tsao HK. Surface tension increment due to solute addition. Phys Rev E. 2004 Mar;69(3):031605.

204. Vargaftik NB, Volkov BN, Voljak LD. International Tables of the Surface Tension of Water. J Phys Chem. 1983;3(12).

List of software

1. Leica Microsystems LTD. (2023). Leica Application SuiteEZ version: 3. 4. 0., Available at: Leica Application Suite Download - Leica Application (informer.com)
2. Rasband, W.S., ImageJ, U. S. National Institutes of Health, Bethesda, Maryland, USA, https://imagej.nih.gov/ij/, 1997-2018.
3. RStudio Team (2020). RStudio: Integrated Development for R. RStudio, PBC, Boston, MA URL http://www.rstudio.com/.
4. The Mathworks Inc. (2023). MATLAB version: 9.14.0.2239454 (R2023a), Natick, Massachusetts: The MathWorks Inc. Available at: https://www.mathworks.com
5. The MathWorks Inc. (2023). Image Processing Toolbox version: 11.7., Natick, Massachusetts: The MathWorks Inc. Available at: https://www.mathworks.com
6. The MathWorks Inc. (2023). Computer Vision Toolbox version: 10.4., Natick, Massachusetts: The MathWorks Inc. Available at: https://www.mathworks.com

Appendices

Appendix 1: Damage accumulation within the discal region

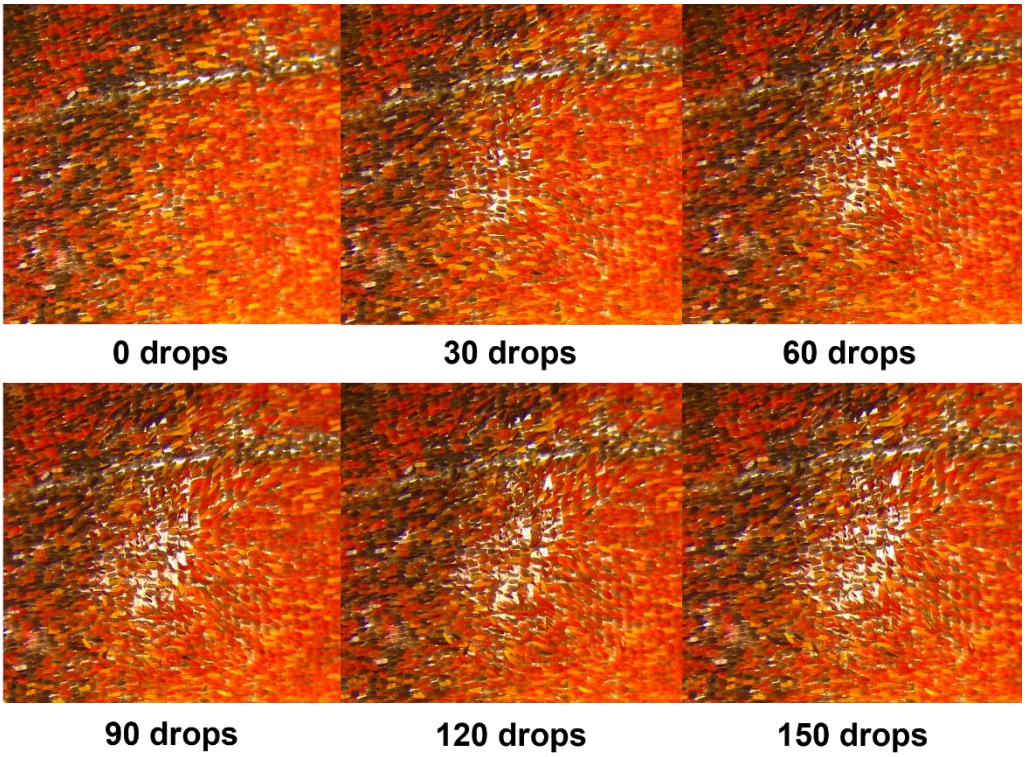

Figure A1. Calibrated images taken of the discal scale-layer of *Attacus* wings at 30 drop interval of repeated drop impact.

Appendix 2. Classification of the descaled transparent membranes

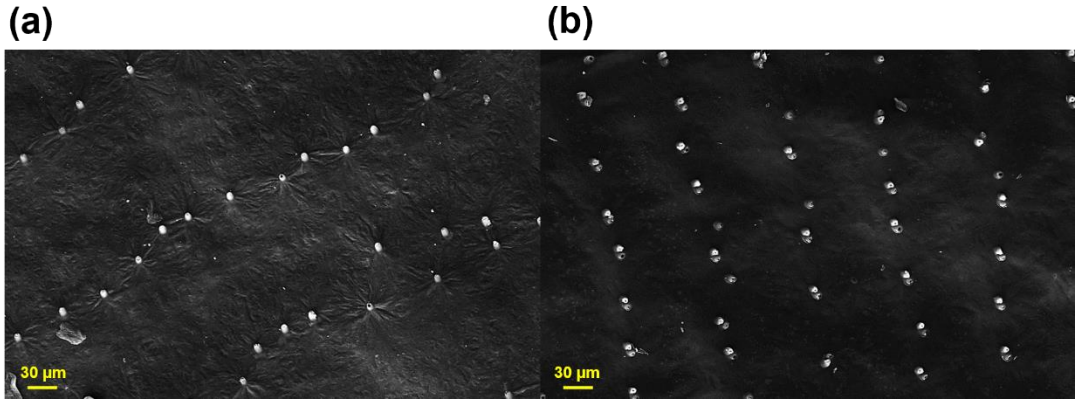

Figure A2. A scanning electron microscope image taken of the descaled membranes of the transparent window of *Attacus* wings (a), and the discal region of *M. confusa* wings (b) at 100x magnification.

The surface structure of the descaled TW and *M. confusa* membrane. Both the TW and *M. confusa* membranes demonstrated one-tier roughness, comprised of ridges (mean widths: 150.68 µm and 90.15 µm respectively) formed by scale insertion points organised in lateral rows. In the TW membrane, ridges were comprised of singular insertion points, whereas on the *M. confusa* membrane insertion points were coupled in pairs.